

Source Analysis of Induced Earthquakes in the Western Canada Sedimentary Basin

by

Ruijia Wang

A thesis submitted in partial fulfillment of the requirements for the degree of

Doctor of Philosophy

in

Geophysics

Department of Physics
University of Alberta

© Ruijia Wang, 2018

Abstract

It has been long known that industrial activities can trigger earthquakes and the topic of “induced earthquake” embraces a great deal of scientific interest in recent years. Globally, several damaging events (i.e., $M_w > 5$) have been linked with fluid injection/extraction. In the Western Canada Sedimentary Basin (WCSB) alone, hundreds of events have been associated with local hydraulic fracturing (HF) operations for shale gas exploration. In this thesis, I present my recent work that systematically analyzed two $M_L > 4$ HF induced earthquakes and explore the source characteristics of recent induced/natural earthquakes within the WCSB.

The first record-breaking (i.e., “red-light” earthquake with $M_L > 4$) earthquake ($M_L = 4.4$, $M_w = 3.9$) occurred on June 13, 2015 in western-central Alberta, Canada. Employing the moment tensor inversion metrics, I revealed the strike-slip mechanism of this earthquake and further improved the accuracy of its hypocentral location. Our spatial grid search, based on moment tensor inversion, confirmed the association between this event and nearby HF operations within the Duvernay play at a depth of around 3.5 km, coinciding with the hypocentral depth of this earthquake.

The largest earthquake (i.e., the second “red-light” earthquake) in Alberta in the past decade shook the town of Fox Creek, on January 12, 2016. Similar to other $M_w \sim 3$ earthquakes, the $M_L = 4.8$ event exhibits a dominant strike-slip (strike= 184°) mechanism with limited non-double-couple (non-DC) components ($\sim 22\%$). Furthermore, industry-contributed local seismic recordings permit high-precision detection analysis and unveil 1108 smaller events within 3 km radius of the

epicenter of the main event. The detected cluster shows close spatial-temporal relation to a nearby HF well and prefers high-angle N-S trending faults, which mirrors the Pine Creek fault zone reported by earlier studies of active source seismic and aeromagnetic data.

In chapter 5, I systematically compared 33 well-resolved focal mechanisms in the WCSB. Most of the regional seismicity is dominated by strike-slip/thrust faulting regimes, whereas limited (but consistent) non-DC components are obtained from injection-induced seismicity in central Alberta. I interpret the persistent compensated-linear-vector-dipole (CLVD) components (M_w 2.1-3.8) as reflecting fracture growth and/or non-coplanar faults slippages during HF stimulations. I further expand the moment tensor decomposition analysis to four representative classes of induced seismicity globally and find that the overall contribution of non-DC components is largely comparable between induced and tectonic earthquakes.

Preface

Chapter 3 has been published as Wang, R., Gu, Y. J., Schultz, R., Kim, A., & Atkinson, G. (2016). Source analysis of a potential hydraulic-fracturing-induced earthquake near Fox Creek, Alberta. *Geophysical Research Letters*, 43(2), 564-573. I was responsible for data collection and analysis as well as manuscript preparation. R. Schultz helped to identify the hypocentral location of the studied event. A. Kim assisted the moment tensor analysis using double-couple forward modeling, and G. Atkinson conducted the ground-motion analysis. Y. J. Gu was the supervisory author, and all co-authors were involved with concept formation and manuscript preparation as well as revision.

Chapter 4 has been published as Wang, R., Gu, Y. J., Schultz, R., Zhang, M., & Kim, A. (2017). Source characteristics and geological implications of the January 2016 induced earthquake swarm near Crooked Lake, Alberta. *Geophysical Journal International*, 210(2), 979-988. Part of this chapter is also included in Wang, R., Gu, Y. J., Schultz, R., & Zhang, M. (2017) Hydraulic fracturing induced seismicity in western Canada: insights from focal mechanism and swarm analysis. *2017 SEG Workshop: Microseismic Technologies and Applications*. I was responsible for data collection and analysis as well as manuscript preparation for both publications. Both R. Schultz and M. Zhang contributed to the analysis of special-temporal relationships between studied cluster and well. Y. J. Gu was the supervisory author, and all co-authors were involved with concept formation and manuscript preparation as well as revision.

Chapter 5 (excluding section 5.4) has been revised by *Geophysical Research Letters* as “Faults and non-double-couple components of induced earthquakes,” Wang, R., Gu, Y. J., Schultz, R., & Chen, Y. I was responsible for data collection and analysis as well as manuscript preparation. The explanation of the non-DC components for events near Fox Creek is mainly based on discussion with R. Schultz and Y. Chen. Y. J. Gu was the supervisory author, and all co-authors were involved with concept formation and manuscript preparation as well as revision.

I dedicate this thesis to my beloved parents.

Acknowledgments

I would like to express my sincere gratitude to my supervisor committees (Prof. Yu Jeffrey Gu, Prof. Mauricio Sacchi, and Prof. Claire Currie) for their excellent guidance and support during my Ph.D. Prof. Yu Jeffrey Gu has been instrumental in my scientific growth and all my accomplishments are impossible to achieve without his tolerance, patience, instructions, and encouragements. I appreciate my committee members and examiners (Prof. Honn Kao, and Prof. Jeffrey Kavanaugh) for their suggestions, which greatly improved the quality of my thesis. Other professors, especially Prof. Douglas Schmitt, Prof. Mirko van der Baan, and Prof. Vadim Kravchinsky in geophysics have been supportive of my research and teaching duties. I also appreciate the support and guidance from my current supervisors (Prof. Gail Atkinson and Prof. Robert Shcherbakov).

Special thanks are given to Ryan Schultz, who supported me as a friend, co-author, and mentor - with tremendous peer-pressure.

Thanks to Dr. Yunfeng Chen, Dr. Ramin Dohkt, Dr. Yuanyin Zhang, Jiayue Shen, Javad Yusifbayov, and Dr. Lei Wu for collecting data from CRANE stations. They all have been great officemates and always initiate insightful discussions. My colleague and friend, Yunfeng Chen offered generous help to me in both research and life, thus deserve tons of appreciation.

I also would like to thank Natural Resources Canada, Nanometrics, Saint Louis University Earthquake center, National Earthquake Information Center, and Alberta Geological Survey for preliminary information of the studied earthquakes. Earthquake catalogs and moment tensors in the United States are generated from USGS (United States Geological Survey) online catalog and GCMT (Global Centroid Moment Tensor Catalog). Data of RAVEN and TD stations are requested from Incorporated Research Institutions for Seismology (IRIS); the TD stations are contributed to IRIS by TransAlta.

I would also thank Dr. John Ristau, Dr. Simone Cesca, and Dr. Xinlin Lei for sharing the moment values of some studied events. Moment tensors in western Canada were computed based on the TDMT-INVC-ISO package developed by Douglas Dreger and Sean Ford of the Berkeley Seismological Laboratory, and Green's functions were computed using the FKRPROG software developed by Chandan Saikia. Most figures in this paper were generated using the Generic Mapping Tool (Wessel *et al.* 2013) and some plots (e.g., Figure 5.2) based on Matlab codes shared by Dr. Vaclav Vavryčuk.

The present thesis is partially supported by the Helmholtz-Alberta Initiative (HAI grant RES0019262), Natural Sciences and Engineering Research Council of Canada, and the Doctoral Recruitment Award from the Faculty of Graduate Studies and Research.

Contents

Abstract.....	ii
Preface.....	iv
Acknowledgments	vi
List of Tables	xi
List of Figures.....	xii
List of Abbreviations	xxiii
1 Introduction.....	1
1.1 Seismicity detection and classification in the WCSB	4
1.2 Geological setting of the WCSB	8
1.3 Industrial activities in the WCSB.....	11
1.3.1 Mining activities and wastewater disposal	11
1.3.2 Multistage hydraulic fracturing.....	14
1.4 Thesis outline	18
2 Data and Methods	20
2.1 Introduction	20
2.2 Focal mechanism determination and moment tensor decomposition	21
2.2.1 P-wave first motion determination.....	24
2.2.2 Full moment tensor inversion and forward modeling.....	25
2.2.3 Moment tensor decomposition and display	31
2.3 Cross-correlation based cluster location	36
2.3.1 Double difference relocation (HypoDD)	36
2.3.2 Match and Locate (M&L).....	39
3 First “Red-light” Event	43

3.1	Introduction	43
3.2	Data and improvements on method.....	45
3.3	Results	47
3.3.1	Focal mechanism and moment tensor decomposition	47
3.3.2	Improving hypocenter location and depth	50
3.3.3	Uncertainties	52
3.3.4	Analysis of ground-motion amplitudes.....	53
3.4	Discussion	55
3.5	Summary	60
4	Second “Red-light” Event	62
4.1	Introduction	62
4.2	Study region and data.....	64
4.3	Adjustment on the velocity model and method.....	64
4.4	Results	67
4.4.1	Magnitude and focal mechanism solution	67
4.4.2	Hypocenter location of the J12EQ.....	70
4.4.3	Detection and location of the earthquake swarm.....	72
4.5	Discussion	76
4.6	Summary	80
5	Faults and Non-double-couple Components	82
5.1	Introduction	82
5.2	Background and datasets.....	83
5.2.1	Recent intraplate events in western Canada.....	83
5.2.2	Representative world-wide cases.....	85

5.3	Results	86
5.3.1	Moment tensors solutions and decomposition.....	86
5.3.2	Moment magnitudes of recent events in the WCSB.....	87
5.4	Moment tensor decompositions and implications.....	91
5.4.1	Double-couple faulting in western Canada.....	91
5.4.2	Interpretations of non-double-couple components	93
5.4.3	The non-DC component: prevalence and implications.....	96
5.5	Summary	100
6	Conclusions and Future Work.....	101
6.1	Conclusions	101
6.2	Future work	102
	Bibliography	104
A	Appendix.....	125
A1.	Input parameter and velocity model set up for moment tensor inversion.....	125
A1.1	Hypocenter locations and synthetic tests setup.....	125
A1.2	Velocity model test	128
A1.3	SNR test	134
A1.4	Real data fitting and conclusions	149
A2.	Related software.....	150

List of Tables

Table 2.1: Analysis approaches based on magnitudes.	21
Table 3.1: Moment tensor decomposition and VR for various frequency ranges and inversion or forward modeling restrictions. Note the VR values show no difference between deviatoric and full moment tensor inversion for all choice of frequency ranges, indicating the isotropic component is negligible for the studied event.	48
Table 4.1: Comparison of inversion results at various hypocenter locations VR (see Equation 10) values and moment tensor decompositions for different hypocenter locations before and after the correction for individual components. The preferred solution is shown in red. The names and locations of the agencies are indicated in Figure 4.1.	71
Table A.1: Input moment tensor for the synthetic test.....	127
Table A.2: Summary of velocity model tests.....	128
Table A.3: Summary of SNR tests.....	135
Table A.4 List of used software for this thesis.....	150

List of Figures

Figure 1.1: Induced and triggered seismicity has been observed worldwide in conjunction with industrial activities. This figure shows the global distribution of anthropogenic seismicity and the maximum magnitude reported at each site. The catalog (source: Davies et al. 2013, updated in July 2018), shows the scientifically documented seismic events associated with different industrial operations (each type of industrial activity is represented by a particular color). The seismic sequences are decluttered, and only the maximum magnitude of the sequence (if $M_L > 1.5$) is reported. The highest number of induced seismic events are related to mining and hydrocarbon industrial activities, whereas those related to wastewater injection operations, although significant in terms of magnitude, are the fewest (plot on the bottom right corner). The label “Oil and Gas” includes hydrofracking (i.e., hydraulic fracturing, see section 1.3.2 in this thesis for details), secondary recovery, oil and gas extraction, and natural gas storage. Modified after Grigoli et al. 2017, with permission.. 2

Figure 1.2: Illustration of different types of industrial activities and their mechanisms of causing an earthquake: a) direct interaction between the injected fluid and pre-exist faults, b) fluid migration and stress load on pre-existing faults, and c) high-pressure fluid injected to create new fractures. (Figure from Francesco Grigoli, personal communication). 3

Figure 1.3: Seismic networks in the study area. The seismic active region of WCSB is roughly defined by the yellow box, following Zhang et al. (2016). Clusters of stations are not labeled with station names. Data used in the following analysis are obtained from 5 seismic networks: CRANE-Canadian Rockies and Alberta Network; RAVEN-Regional Observatory of Alberta Earthquake Network; TD-TransAlta Dam Monitoring Network; CNSN-Canadian National Seismograph Network, and NEBC-Northeast British Columbia Seismographic Network (plotted using the same symbol as CNSN stations). 5

Figure 1.4: Distribution of earthquakes (1985-2017), mining blasts, and seismic stations (brown triangles, see Figure 1.3 for seismic network details) in the WCSB. Significant induced earthquakes are marked by the red stars, and mining blasts are shown as small blue diamonds. 8

Figure 1.5: Isopach map of the WCSB showing the locations of the Alberta Basin and Williston Basin. The column on the right gives a general scheme for the evolution of Phanerozoic tectonic events recorded in the Cordillera that influenced sedimentation in the Alberta Basin. Figure from Ross and Eaton, 1999. 10

Figure 1.6: P-to-Surface wave amplitude ratio recorded at CRANE stations for earthquakes (red) and mining blasts (blue). The background is interpolated values from plotted stations.. 11

Figure 1.7: Time of day comparison for mining events and earthquakes activities in the southern WCSB (2006-2010). Eq-earthquake, mine-mining activities..... 13

Figure 1.8: Day of week comparison for mining events and earthquakes activities in the southern WCSB (2006-2010). Eq-earthquake, mine-mining activities..... 13

Figure 1.9: Schematic diagram for multistage hydraulic fracturing. A well is drilled down toward the targeted shale layer and then drilled horizontally along a layer. 14

Figure 1.10: Screenshot of the interface of GeoSCOUT for a 10×10km area near Crooked Lake (blue). Injection wells are shown with circles and squares. For multistage hydraulic fracturing wells, the line connecting the well pads (squares) and well bottom (circles) represent the well extension projected on the surface. Recent wells (after 2015) are shown in red and selected well is highlighted in pink..... 15

Figure 1.11: Major shale formations and maximum crustal stress orientation (S_H , yellow dashes) in the WCSB (Heidbach et al. 2016). From north to south the shale formations are commonly referred to as Liard Basin, Horn River Basin (Muskva formation), Cordova Embayment (ordered by color from left to right), Montney, Duvernay, Alberta Bakken (Rivard et al. 2014; BCOGC 2014, 2012). The earthquakes are shown by the small grey circles, and the tectonic boundaries in Alberta are marked by the dashed lines..... 17

Figure 2.1: Flow diagram for moment tensor determination and validation. The depth search and bootstrap parts are presented and discussed with corresponding events in chapters 3-5.. 21

Figure 2.2: 1D structure model used for full moment tensor inversion. The sedimentary layer is colored in red, and the upper mantle is colored in green. The velocity (V_p cmb, V_s cmb) and density model was resolved by Chen et al. (2015b; station PER). The attenuation model (Q_p , Q_s) is modified from Zelt and Ellis (1990). 23

Figure 2.3: First motion received at seismometer. Filled dots represent compressional (positive onset of the waveform) and open dots represent dilatational (positive onset of the waveform). Figure credit from USGS Earthquake Glossary. 25

Figure 2.4: Example for negative (dilatational) P-wave first motion: showing the Mw3.9 earthquake received by a RAVEN station (STPRA) at azimuth = 21°, distance = 181 km. 25

Figure 2.5: Example of output (Mw=3) for the full moment tensor inversion (TDMT_INV) program. Note that station BRLDA and SNUFA have both high and low-frequency ranges used while other stations are left with only high-frequency ranges due to the relatively low signal-to-noise ratio in low-frequency range. 31

Figure 2.6: Example of different moment tensor decomposition methods. The deviatoric part could be decomposed into six different combinations shown in the box. The first two methods are chosen and interpreted in the main text (see chapter 5). 34

Figure 2.7: Locations of mining blasts (2006-2010) in southern Alberta before relocation using HypoDD. 38

Figure 2.8: Locations of mining blasts (2006-2010) in southern Alberta after relocation using HypoDD. 39

Figure 2.9: Waveform similarity plot for the multiples of the Jan 12, 2016 earthquake. Multiples are detected based on a fix location and cross-correlation (CC) larger than 0.5 from M&L (Zhang & Wen 2015). Spatial and temporal distributions of a more complete detection are discussed in chapter 4. Color bar indicates the degree of similarity ranging from 0 to 1. Magnitudes of corresponding events are shown on the right. 40

Figure 2.10: Example of a smaller event (Mw=0, grey waveforms) is “matched” by a template event (red waveforms) during M&L. Three components data from four industry stations (listed on the left) are used here, and the cross-correlation value is larger than 0.7. Corresponding CC value for each component is labeled on the right. 42

Figure 3.1: Spatial distribution of seismic stations (triangles and diamonds) and earthquakes after 2006 (circles) with magnitudes greater than 3.0. The earthquake data are obtained from the Alberta Geological Survey (2006-2010) (Stern et al. 2013) and Natural Resources Canada (2011-2015, <http://earthquakescanada.nrcan.gc.ca/recent/index-eng.php>, last

accessed August 2015). The grey dashed lines denote the Proterozoic domain boundaries (Clowes et al. 2002; Ross et al. 1999). The map inset in the lower right corner highlights the hypocenter locations reported by different agencies: Natural Resources Canada (NRC), Nanometrics Athena (NMX), Saint Louis University Earthquake Center (SLU), Alberta Geological Survey (AGS), and National Earthquake Information Center (NEIC). 44

Figure 3.2: Inversion results and the vertical-component waveforms of low (0.05-0.1 Hz, 11 stations) and high (0.08-0.4 Hz, 8 stations) frequencies. The solid and dashed lines show the observed and best fitting synthetic data, respectively. The result of my full moment tensor inversion is shown in the center of the page and two DC solutions from forward modeling (left, this study) and moment tensor inversion (right, SLU, from http://www.eas.slu.edu/eqc/eqc_mt/MECH.NA/20150613235753-/index.html, last accessed Sep 2015) are shown in the upper-left corner. The latter two moment tensors used slightly different datasets and hypocenter locations (see text for details). For comparison, the non-DC component from the full moment tensor inversion is also plotted beneath the DC solutions. In all cases, the shaded quadrants are compressive. The small circles on the focal mechanisms indicate compressional (open) and dilatational (solid) P-wave first motion, determined from vertical component waveforms in the frequency range of 0.5-5.0 Hz. The takeoff angles are calculated from IASP91 (Kennett & Engdahl, 1991). 49

Figure 3.3: a) Interpolated VR (see Equation 10) for 14 uniformly distributed hypothetical source locations (yellow circles). The stars indicate the four reported epicenters as denoted. The maximum VR is obtained near the center of the grid. b) Interpolated RES/Pdc values (normalized residual, see Equation 11) for the same 14 source locations. The minimum RES/Pdc values roughly coincide with the AGS location, and consistently low values are observed along an N-W orientation. c) VR for a range of depths. The focal mechanism from independent inversions using body (red) and surface (blue) waves suggest optimal depths of 3 km (red triangle) and 4 km (blue triangle), respectively. The solid and dashed lines without focal mechanisms indicate the outcomes of joint inversions of surface and body waves with assumed amplitude ratios of 1 and 2. The arrows indicate the reported earthquake depths from four agencies. d) Fault plane solutions determined from a

bootstrap resampling test using 200 trials (Efron & Tibshirani 1991) (see section 3.3.3 for details)..... 51

Figure 3.4: Sensitivity of inversion results to input velocity and Q structures. Input shear and compressional velocities (solid and dashed lines in color) and density (black) models for full moment tensor inversions. The four models are edited from V_s model PER of Chen et al. (2015b) (blue), V_p model from Bouzidi et al. (2002) (yellow), a combined model from Welford & Clowes (2006) and Chen et al. (2015b) (red), and the combined model with 20% velocity reduction (green). The inverted double-couple solutions are shaded using the same color conventions. In all cases, the scaling factor between V_p and V_s is based on empirical equations from Brocher (2005). All four solutions show a similar strike, dip and rake angles. 53

Figure 3.5: Input Q models for moment tensor inversions based on Zelt and Ellis (1990). The scaling factors are 1.3 (optimal, black), 0.5 (blue) and 2.0 (red), respectively. Changing the input Q models only changes the moment magnitude from the moment tensor inversions by 0.03. 54

Figure 3.6: Horizontal-component response spectral amplitudes (PSA, 5%-damped pseudo-acceleration). a) PSA versus hypocentral distance at 1 Hz (blue) and 5 Hz (orange), compared to prediction equations of the simulation-based ground motion model of Yenier and Atkinson (2015) for central and eastern North America, for Mw = 3.9. b) Inferred PSA source spectrum, after correction for site response, in comparison to Brune-model spectrum for Mw = 3.9 and a stress drop of 60 bars. 55

Figure 3.7: Crustal stress and available focal mechanisms of Mw>3.5 earthquakes superimposed on a tectonic map of the study region. The thin solid lines denote the proposed Proterozoic domain boundaries (Ross et al. 1999). The rate and direction of the absolute present-day plate motion are indicated by the blue arrow (DeMets et al., 1990). The crustal stress from borehole breakout data are represented in yellow, and those determined from seismic source solutions are shown in red (Heidbach et al. 2010). The bottom left map inset highlights the source region, and the interpreted fault movements are indicated by the double arrows. The blue cross marks a graben (faults) in the depth range of 3.1–3.8 km, mapped by an earlier active-source seismic survey (Green & Mountjoy 2005, also see

Figure 3.8). The area shaded in green denotes the Wabamun domain. The area shaded in light blue indicates the shape and location of the Duvernay Formation, and the rich-gas region is highlighted in red (obtained from Oilweek Magazine, 2013). The map inset in the top right corner shows the hypocenter locations (stars) relative to two HF wells (blue squares) that were active during June 2015. The bottom depths and the latest well completion dates are as follows: M1: 2415.0 m, June 7, 2015; D1: 3434.7 m, June 2, 2015; D2: 3433.9 m, June 5, 2015; D3: 3445.0 m, May 10, 2015; D4: 3446.1 m, May 11, 2015.

..... 57

Figure 3.8: Vertical fault(s) within 10km of the hypocentral location of the June 12, 2015 earthquake mapped by a previous 3-D seismic survey. Figure from Green & Mountjoy (2005)..... 59

Figure 4.1: Spatial distribution of seismic monitoring stations and earthquakes (circles) since 2013; Mw>4 earthquakes are shown in red. The area of occurrence of the Duvernay Formation is shaded in light green, with the wet-gas region highlighted in yellow (Rokosh et al. 2012). Crustal stress orientations obtained from borehole breakouts are shown by the grey lines. The map inset shows the epicenters of the January 12, 2016 event reported by different agencies (red stars): U. S. Geological Survey (USGS); Nanometrics Athena (NMX); Saint Louis University earthquake center (SLU); Alberta Geological Survey (AGS); Natural Resources Canada (NRC), where “p” and “u” indicate the previous and updated locations, respectively. 63

Figure 4.2: Comparison of the focal mechanism before (bottom) and after (top) the secondary shifts applied to individual components of each local station (<250 km). 65

Figure 4.3: Example of waveform fitting from station TD002. The high-frequency body-wave waveforms are shown on the left, and the low-frequency surface-wave waveforms are shown on the right. The dark grey curves are the observed data, and the red/dash curves are the synthetic data after/before applying secondary shifts to correct the possible effect of anisotropy. 66

Figure 4.4: a) Moment tensor solution, observed (grey) and best-fit synthetic (red) vertical-component waveforms. Station names and the corresponding azimuths are labeled near the observed waveforms. High-frequency body waves are also used and displayed for

stations within 250 km (to the left of the low-frequency waveforms). The circles on the focal mechanism indicate compressional (filled black) and dilatational (filled white) P-wave first motions picked from vertical-component waveforms (including industry contributed stations). The crosses indicate unknown first motions due to low signal-to-noise ratios in P arrivals. The focal mechanism from pure-DC modeling is shown in the lower left corner. b) Inversion results for different epicenters and the possible responsible HF wells with drilling completed in early (green) and late (red) 2015. The focal mechanism for the June 13, 2015 earthquake is presented in the lower right corner with the corresponding HF wells (blue). c) Depth search using different input data. The black arrows indicate the available focal depths reported by different agencies and the red arrow indicates the injection depth of HF operations in the source area. 68

Figure 4.5: Bootstrap resampling tests of the inversion stability using the following four subsets of the recordings: near source stations (30×250 km); far source stations (250×700 km); azimuth between -125° to 45° (NW); azimuth between 45° to 235° (SE). Seventy percent of the stations from each group are used during bootstrapping, and the black lines show the corresponding fault planes from 200 trials. Corresponding result from the forward simulation are also shown. The red and blue dots mark the corresponding P- and T- axes from each solution..... 69

Figure 4.6: (a) Injection at the HF well (well ID: 100/15-25-062-23W5/00). Each bar represents a single HF stage, and the cumulative volume is shown by the solid black line. (b) Similar to (a) but for treatment pressure at each stage. Superimposed on the plot are the detected multiples (yellow circles) with $CC > 0.5$ and the cumulative seismic moment (red line). The grey dash line in both plots marks the period of HF stimulation (January 4 to 12, 2016). The largest event occurred during the last stage of stimulation, followed by a decrease in seismicity rate. 73

Figure 4.7: Frequency-magnitude distribution of the detected swarm (the Gutenberg-Richter law) containing 1108 events ($CC > 0.3$) with a magnitude of completeness $M_c \sim 0.4$ (in M_L). ... 74

Figure 4.8: (a) Locations of the January swarm (red, $CC > 0.5$) detected using data from 4 industry-contributed stations (yellow triangles). The HF well associated with the January 2016 earthquake swarm is shown by the red line and nearby the wells associated with an earlier

swarm (brown, January 2015) are shown in orange (Bao & Eaton 2016, Schultz et al. 2017). Other active wells in 2015 and 2016 are shown in green. (b) and (c) Cross-sectional views of the detected events for the swarm within the dashed box shown in a). Some events are overlapped due to the limited size of the search grid..... 75

Figure 4.9: (a) A summary of the resolved focal mechanism and moment magnitude of the moderate earthquakes around Fox Creek. The event triggered the “traffic-light” protocol is highlighted by pink, and the two red-light cases are highlighted by red. When the data quality is insufficient for full moment tensor inversion (blue), focal mechanisms are resolved from DC forward modeling (black). The latter one may have larger uncertainty in fault plane orientations. Note there are eight $M_L > 3$ events took place during November and December 2016, out of which seven were resolved with focal mechanism solutions, as presented. (b) A model showing vertical fault(s) and the flower structure along the north-south orientation as suggested by Berger & Davies (1999). The directions of motion on the suggested fault (red solid arrows) and auxiliary (red dash arrows) planes from event investigated in this chapter are as indicated..... 79

Figure 5.1: Distribution of stations (triangles) and earthquakes (small red circles) in western Canada (1985-2017). The magnitude-scaled “beachballs” show the focal mechanisms of tectonic (green), hydraulic-fracturing induced (red), and secondary recovery induced (blue) events. See list of abbreviations for the network names..... 84

Figure 5.2: The difference between different magnitude scales. Green diamonds are natural ones, and red dots are recently induced ones. The equations in corresponding colors are best linear fits represented by the dashed lines. The solid lines show fits with a fixed slope (1), parallel to the black line representing $M_w = M_L$ 88

Figure 5.3: The relationship between seismic moment and total injected volume has been examined in a recent study by Atkinson et al. 2016, showing world’s largest HF induced earthquakes (red stars). From top to bottom: $M_w = 4.9$ ($252,000\text{m}^3$, Lei et al. 2017); $M_w = 4.6$ ($320,000\text{m}^3$, Mahani et al. 2017); $M_w = 4.1$ ($298,000\text{m}^3$, Wang et al. 2017a). The red arrows indicate how the coordinate for a specific event moves after obtaining the moment magnitude through moment tensor inversion and revised injection volumes. Figure modified after Atkinson et al. 2017 (with permission). 90

Figure 5.4: a) Examples of fault plane solutions (uniform sizes) determined from bootstrap resampling test for events in the WCSB. The P-axes are consistently aligned along NE-SW for both strike-slip (top) and reverse (bottom) faulting mechanisms, comparable to nearby S_H orientation (Heidbach et al. 2016). b) Variance reduction (fit) vs. noise level during synthetic tests (see Appendix for detailed results and test on velocity model variation). Real noise is multiplied by N times and added to synthetic waveforms generated with 20% of CLVD and 0% of isotropic components. Only the non-DC components after decomposition are plotted, and the corresponding percentages are labeled on top. 92

Figure 5.5: Decomposition of the deviatoric parts for the hydraulic fracturing induced events in central Alberta. The event dates are indicated at the bottom and sizes of the different components are scaled to the magnitudes. Events are aligned by variance reduction values (see legend for the shade) and the red dashed line indicated 70% value. Two methods are presented: max DC and CLVD (rows 1-2) or major DC and minor DC (rows 3-4). Normalized summations of each row are on the right. All decompositions are consistent regardless of the magnitude and date of these events, except for the event on 5 December 2016. b) Map view of the interpretations of the two decomposition styles related to hydraulic fracturing: CLVD components (left) and minor DC components (right). Black arrows indicate relative motions. The minor fault (right) is extensional possibly due to the external pressure load on the highly fractured zone along the HF well..... 95

Figure 5.6: Percentage of DC components v.s. moment magnitude for the studied earthquake catalogs. 97

Figure 5.7: Decompositions of the collected dataset. a) Averaged percentages (shaded bars) and standard deviations (black error bars) of the DC, CLVD, and isotropic components (ISO). b) Hudson’s plot summarizing the decomposed moment tensors for the listed regions. Geothermal induced events (purple bars) in the western U.S. are only presented in Figure a (moment tensor values are unavailable). For both plots, tectonic events (labeled with ‘N’) are shown in grey scale, and induced events (labeled with ‘I’) are shown in color. 99

Figure A.1: Station distribution for the synthetic tests. The red star denotes the location of earthquake hypocenter (depth = 4 km). 126

Figure A.2: Decomposition of zero-noise recovered moment tensor. The isotropic (ISO) part is zero (0%), and the deviatoric part can be decomposed into 1) DC (80%) and CLVD (20%) or 2) major (M=3.1) and minor (M=2.4) DCs.	128
Figure A.3: Outcomes of the change on my preferred 14-layer model (solid lines) for $\pm 10\%$ (dot-dashed lines) and $\pm 20\%$ (dashed lines) perturbations to all layers.	129
Figure A.4: Random perturbation (up to $\pm 10\%$) on the velocity model (dashed lines) relative to the preferred velocity model is shown in solid lines.	129
Figure A.5: Waveform fitting using synthetic data and model with decreased velocity by 20%. The Zcorr are relative shifts and are all negative in this case. The solid lines show the input (simulated) waveforms and the grey dashed lines show the outcomes of the moment tensor inversion. The definitions are consistent for subsequent plots of A6-9.....	130
Figure A.6: Waveform fitting using synthetic data and model with decreased velocity by 10%. The Zcorr are relative shifts and are all negative in this case.	131
Figure A.7: Waveform fitting using synthetic data and model with increased velocity by 10%. The Zcorr are relative shifts and are all positive in this case.	132
Figure A.8: Waveform fitting using synthetic data and model with increased velocity by 20%. The Zcorr are relative shifts and are all positive in this case.	133
Figure A.9: Waveform fitting using synthetic data and model with randomly permuted ($< 10\%$) velocity (relative to the preferred model, also see Figure A2).	134
Figure A.10: Synthetic waveforms (solid lines) fitted with 10% random noise added (dashed lines).	136
Figure A.11: Synthetic waveforms (solid lines) fitted with 15% random noise added (dashed lines).	137
Figure A.12: Synthetic waveforms (solid lines) fitted with 20% random noise added (dashed lines).	138
Figure A.13: Synthetic waveforms (solid lines) fitted with 25% random noise added (dashed lines).	139
Figure A.14: Synthetic waveforms (solid lines) fitted with 30% random noise added (dashed lines).	140

Figure A.15: Synthetic waveforms (solid lines) fitted noise equal to the observed value at each station (dashed lines).....	141
Figure A.16: Synthetic waveforms (solid lines) fitted with 2 times of real noise added (dashed lines).....	142
Figure A.17: Synthetic waveforms (solid lines) fitted with 3 times of real noise added (dashed lines).....	143
Figure A.18: Synthetic waveforms (solid lines) fitted with 4 times of real noise added (dashed lines).....	144
Figure A.19: Synthetic waveforms (solid lines) fitted with 5 times of real noise added (dashed lines).....	145
Figure A.20: Synthetic waveforms (solid lines) fitted with 6 times of real noise added (dashed lines).....	146
Figure A.21: Synthetic waveforms (solid lines) fitted with 6 times of real noise added (dashed lines).....	147
Figure A.22: Synthetic waveforms (solid lines) fitted with 8 times of real noise added (dashed lines): (a) use all four stations and (b) use only two stations with high SNR.....	148
Figure A.23: Synthetic waveforms (with 15% noise) fitted with the randomly perturbed model (relative to the preferred model, see Figure A2). The result resembles my input focal mechanism.	149

List of Abbreviations

AGS	Alberta Geological Survey
NMX	Nanometrics Athena
NRC	Natural Resources Canada
SLU	Saint-Louise University Earthquake Center
NEIC	National Earthquake Information Center
USGS	United States Geological Survey
GCMT	Global Centroid Moment Tensor Catalog
BCOGC	British Columbia Oil and Gas Cooperation
CRANE	Canadian Rockies and Alberta Network
CNSN	Canadian National Seismograph Network
NEBC	Northeast British Columbia Seismographic Network
RAVEN	Regional Observatory of Alberta Earthquake Network
TD	TransAlta Dam Monitoring Network
ATSN	Albert Telemetered Seismic Network
TDMT_INV	Time Domain Moment Tensor Inversion (Dreger 2003)
hypoDD	double-difference earthquake relocation (Waldhauser & Ellsworth 2000)
M&L	Match and Locate (Zhang & Wen, 2015)
GMT	Generic Mapping Tool (Wessel <i>et al.</i> 2013)

CC	Cross-correlation
WCSB	Western Canada Sedimentary Basin
CENA	central and eastern North America
STZ	Snowbird Tectonic Zone
HF	hydraulic fracturing
WWD	waste-water disposal
PSA	pseudo-acceleration
J12EQ	January 12, 2016 earthquake near Crooked Lake, Alberta (i.e., the second “red-light event”)
M _w	moment magnitude
M _L	local magnitude (as defined by Richter, 1935)
mb_Lg	Lg wave amplitude (as defined by Nuttli, 1973)
DC	double-couple (component)
non-DC	non-double-couple (component)
CLVD	compensated-linear-vector-dipole (component)
ISO	Isotropic (component)
VR	Variance Reduction (equation 10)
RES/Pdc	Residual over percentage of double-couple (equation 11)
S _H	Maximum horizontal compressional stress

1 Introduction

In recent years, man-made seismicity has attracted significant scientific attention all over the world (Figure 1.1). Hundreds of earthquake clusters have been linked various types of industrial activities involving fluid injection/extraction or material removal from the underground (Foulger *et al.* 2017; Grigoli *et al.* 2017). Despite the debatable triggering potential of devastating earthquakes (e.g., Mw=7.9, Zipingpu, China), several Mw>5 induced earthquakes in the United States (Yeck *et al.* 2017; McGarr & Barbour 2017) and South Korea (Kim *et al.* 2018; Grigoli *et al.* 2018) have been identified as induced seismicity. In the United States and Canada, oil and gas-producing activities are the dominant factors for the occurrence of such induced seismicity (Atkinson *et al.* 2016; Ellsworth *et al.* 2016).

Accompanying the exponentially increased amount of induced seismicity comes an increase in studies on identifying, understanding, and mitigating these earthquakes. Multi-scale analyses have been conducted, ranging from geomechanical modeling and laboratory experiments to field observations and hazard assessment. I refer readers to Foulger *et al.* (2017) for the collection and summary of case studies of induced seismicity worldwide. Driven by the increasing occurrence of induced earthquakes, several physical mechanisms are proposed, inherited from Coulomb's failure criterion (Figure 1.2; Ellsworth 2013; Grigoli *et al.* 2017). Furthermore, efforts have been made toward robust detection and discrimination of induced earthquakes via enhanced monitoring (e.g., Eaton *et al.* 2018; Karimi *et al.* 2018) and investigation of source parameters (e.g., Davis & Frohlich 1993; Dahm *et al.* 2013). Since an overarching goal is to control and mitigate the seismic hazard (e.g., Peterson *et al.* 2018, 2017, 2016), incorporating induced seismicity, recent studies focus on 1) the estimation the maximum magnitude using injection parameter (e.g., McGarr 2014) and/or statistical catalog simulation (e.g., Beirlant *et al.* 2017) and 2) the determination of the key (industrial or geological) factors that contribute to the occurrence of induced earthquakes (e.g., Holtzman *et al.* 2018; Hincks *et al.* 2018; Schultz *et al.* 2017).

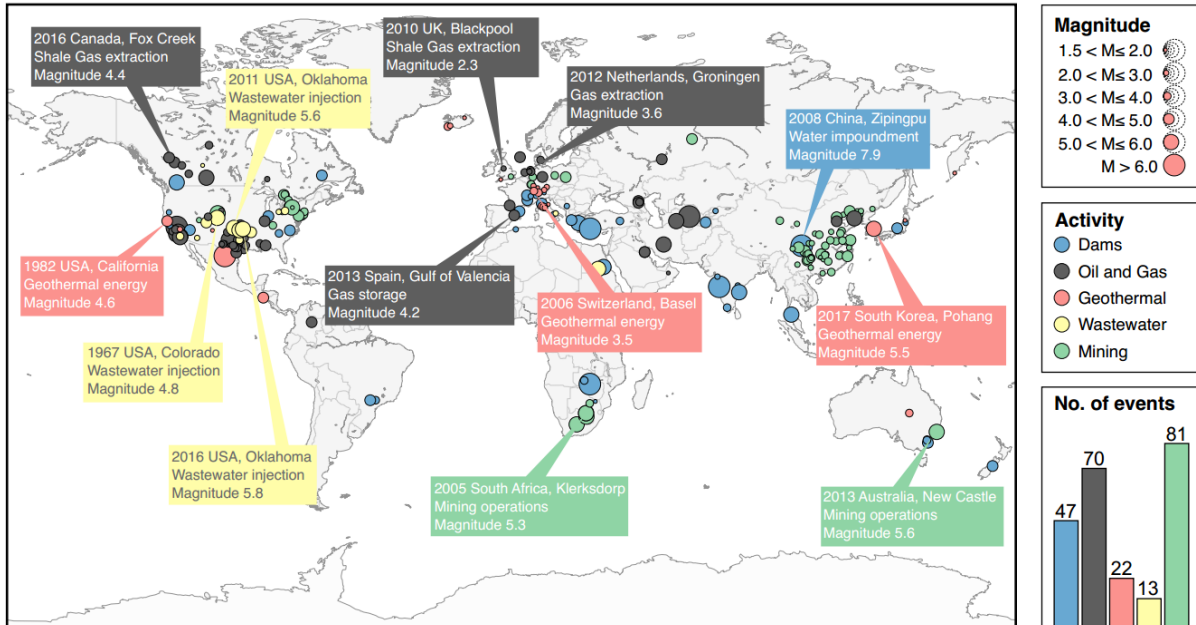


Figure 1.1: Induced and triggered seismicity has been observed worldwide in conjunction with industrial activities. This figure shows the global distribution of anthropogenic seismicity and the maximum magnitude reported at each site. The catalog (source: Davies et al. 2013, updated in July 2018), shows the scientifically documented seismic events associated with different industrial operations (each type of industrial activity is represented by a particular color). The seismic sequences are decluttered, and only the maximum magnitude of the sequence (if $M_L > 1.5$) is reported. The highest number of induced seismic events are related to mining and hydrocarbon industrial activities, whereas those related to wastewater injection operations, although significant in terms of magnitude, are the fewest (plot on the bottom right corner). The label “Oil and Gas” includes hydrofracturing (i.e., hydraulic fracturing, see section 1.3.2 in this thesis for details), secondary recovery, oil and gas extraction, and natural gas storage. Modified after Grigoli et al. 2017, with permission.

Since the contribution of anthropogenic activities on the stress release cannot be quantified, it is difficult to unequivocally differentiate between “triggered” and “induced” earthquakes (i.e., with minor “triggered” or dominant “induced” human contribution; also see Dahm *et al.* 2013). The former term has been associated more frequently with naturally occurring events that take place within short time intervals (e.g., Fan & Shearer 2016; Wang *et al.* 2015). Following the convention of recent studies (Eaton 2018; Ghofrani & Atkinson 2016; Atkinson *et al.* 2016; Rubinstein & Mahani, 2015; Ellsworth 2013), my thesis simply refers to earthquakes associated with human activities as “induced”.

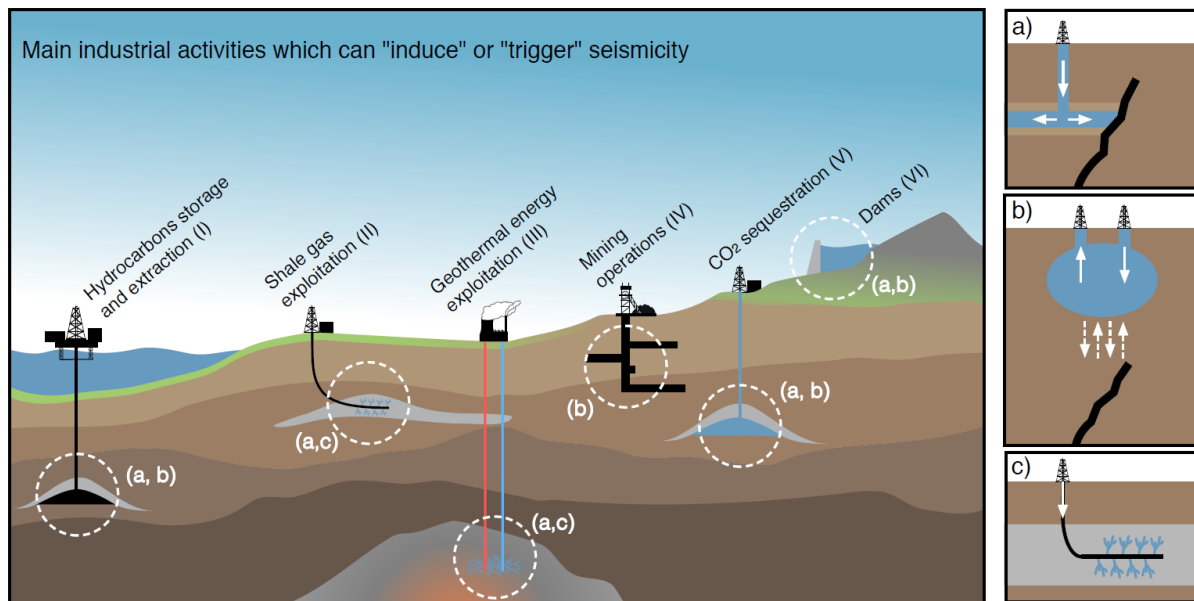


Figure 1.2: Illustration of different types of industrial activities and their mechanisms of causing an earthquake: a) direct interaction between the injected fluid and pre-exist faults, b) fluid migration and stress load on pre-existing faults, and c) high-pressure fluid injected to create new fractures. (Figure from Francesco Grigoli, personal communication).

For induced seismicity in western Canada, hydraulic fracturing (HF) is largely responsible for the increasing number of intraplate earthquakes. The largest earthquakes triggered by HF was recorded in the WCSB (Mahani *et al.* 2016) and is only exceeded by a recent Mw=4.9 in Sichuan, China (Lei *et al.* 2017). Unlike wastewater disposal that accumulates stress load from multiple

suspected wells over months or years, HF shows direct spatial and temporal coupling with specific injection activities (Rubinstein & Mahani 2015). The distribution of induced earthquakes remains debated, though the geological history of the subsurface of the WCSB could play a major role (Schultz *et al.* 2016). Among thousands of injection wells in the WCSB, induced clusters exhibit 1) large spatial and temporal variations and 2) swarm-like behavior that may not follow traditional recurrence laws (i.e., pre-shock and after-shock pattern with dominant main shock; Skoumal *et al.* 2015a).

1.1 Seismicity detection and classification in the WCSB

Historically, broadband seismic monitoring in Alberta-the central part of the WCSB-mostly relies on two broadband stations belonging to the CNSN network: EDM in Leduc and WALA near Waterlon Lake (Figure 1.3). Since 2006, the coverage has been greatly improved by the continuous expansion establishment of CRANE, which is jointly sponsored by the University of Alberta and Alberta Geological Survey. The CRANE network contains over 20 broadband seismic stations operating in campaign mode¹, forming the backbone seismic monitoring system for central Alberta (Gu *et al.* 2011). The Alberta Telemetered Seismic Network (ATSN, sponsored by University of Calgary) was also established in 2009 and includes nine stations to densify the coverage in northern Alberta. Both CRANE (except PER station) and ATSN are stationary permanent seismic networks with limited access to the public. In 2013, the TD and RAVEN (Schultz & Stern 2015) network were established: TD forms dense array around central-eastern Alberta and RAVEN is spread out over the whole province with slightly denser distribution in regions with active exploration activities.

The combination of networks provides relatively uniform coverage throughout Alberta and British Columbia. The frequency range of those stations provides ideal information for locating seismicity (e.g., Schultz *et al.* 2015a) and analyzing crustal structure (e.g., Shen *et al.* 2015; Chen *et al.* 2015b, 2017; Gu *et al.* 2017). Most of the seismic stations use seismic equipment from Nanometrics with a minimum recording frequency range of 0.01 – 20 Hz. In recent years, some of the telemetered

¹ Not telemetered

stations have been upgraded with a recording frequency up to 100 Hz, comparable to the range of company-owned local arrays.

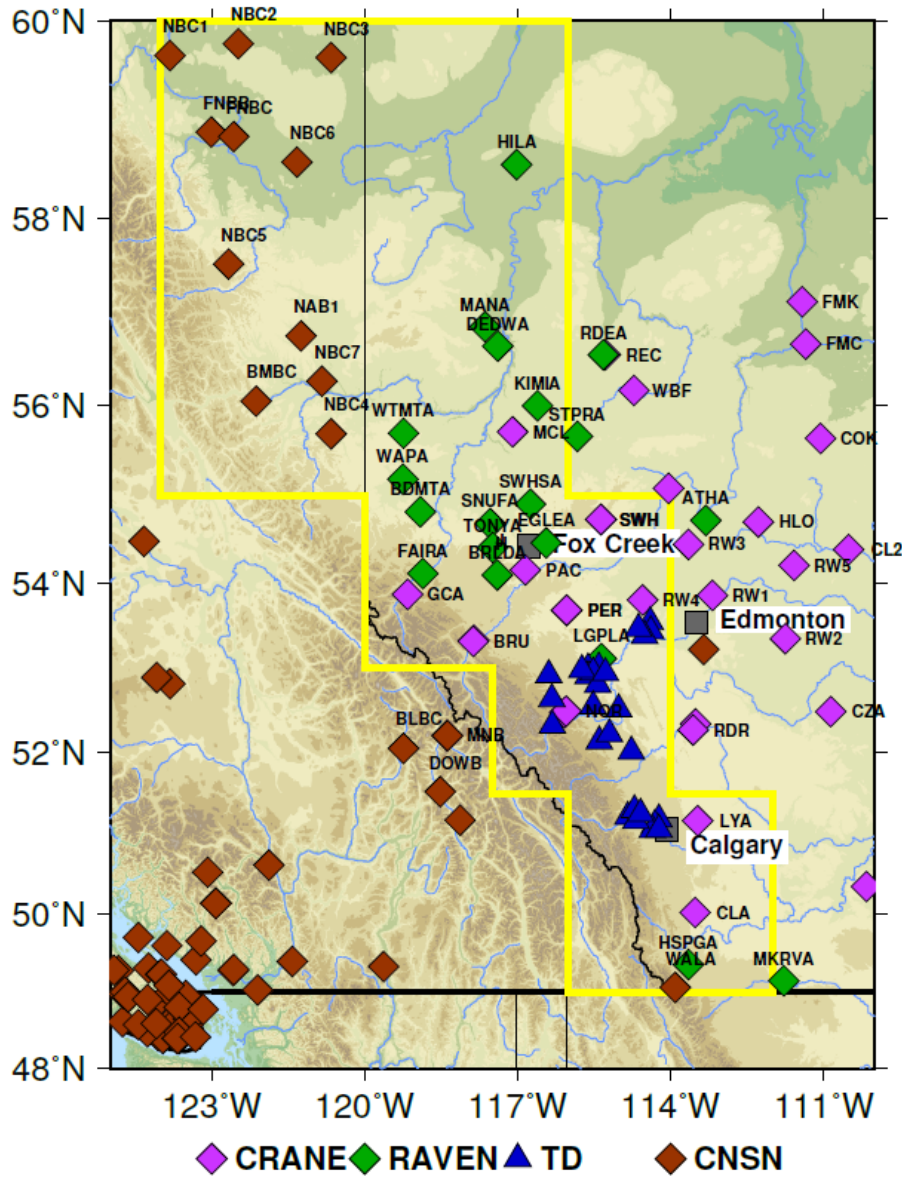


Figure 1.3: Seismic networks in the study area. The seismic active region of WCSB is roughly defined by the yellow box, following Zhang et al. (2016). Clusters of stations are not labeled with station names. Data used in the following analysis are obtained from 5 seismic networks: CRANE-Canadian Rockies and Alberta Network; RAVEN-Regional Observatory of Alberta Earthquake

Network; TD-TransAlta Dam Monitoring Network; CNSN-Canadian National Seismograph Network, and NEBC-Northeast British Columbia Seismographic Network (plotted using the same symbol as CNSN stations).

Seismicity in the WCSB primarily consists of three types of source: mining blasts, natural earthquakes and induced earthquakes (Figure 1.4). From 2006 to 2010, more than 90% (out of ~3500) detected seismicity were mining blasts. These events were mainly recorded by CRANE stations along the Rocky Mountains (i.e., PER, NOR, CLA, and LYA), characterized by highly confined source locations and identical waveforms (see section 1.2.1). In recent years, the expansion of broadband seismic networks provides valuable data that make moment tensor inversion possible for the moment magnitude (M_w) ~ 4 earthquakes. In addition, most of these master events, especially the induced ones, are accompanied by hundreds of pre-/after-shocks ($M_w < 3$) that also share waveforms with high similarity. The growing networks also enable better detection and analysis of these low-magnitude events: for example, ice-quakes with local magnitude (M_L) as small as 2 are also recorded in 2018 (CBC news, 2018).

Earthquakes associated with anthropogenic activities in WCSB, most notably in the Horn River Basin (B.C. Oil and Gas Commission 2012), Montney Formation (Babaie Mahani *et al.* 2017; B.C. Oil and Gas Commission 2014), Cordel Field (Schultz *et al.* 2014), near Cardston (Schultz *et al.* 2015c), Rocky Mountain House (Wang *et al.* 2015; Wetmiller 1986) and Crooked Lake (Schultz *et al.* 2017; Bao & Eaton 2016; Clerc *et al.* 2016; Deng *et al.* 2016; Schultz *et al.* 2015b), have garnered significant scientific interest and public attention in the past 4 years. While the vast majority of these earthquakes could only be detected by sensitive seismic instruments, several events with moment magnitude close to $M_w = 4$ were felt hundreds of kilometers away (e.g., 280 km, CBC 2016; Global News 2016) and have been linked to nearby HF operations (Schultz *et al.* 2017). In the Fox Creek/Crooked Lake region alone, the number of $M_w > 3$ earthquakes increased from 3 over a 28-year period prior to Nov. 2013 to 35 in the last 4 years (Dec. 2013-Feb. 2017) (Earthquakes Canada, 2018). Based on the regional seismic monitoring, no $M_L > 4$ (local magnitude) events were reported in 2017, but the total number of $M_L > 3$ events (72) surpassed that of previous years (Earthquake Canada, 2018). The first moderate earthquake ($M_w 3.6$) occurred in January 2015 (Bao & Eaton 2016) and was accompanied by hundreds of smaller events and became the catalyst in the drafting of the “traffic-light” protocol for completion operations in the Duvernay Formation in this region (Alberta Energy Regulator 2015). Since then, two events have triggered the stoplight (i.e., “red-light” event) in compliance with this regulation, including the

$M_L=4.8$ (Alberta Geological Survey, AGS) earthquake on January 12, 2016 near Crooked Lake, which is the largest in Alberta, Canada in the past decade.

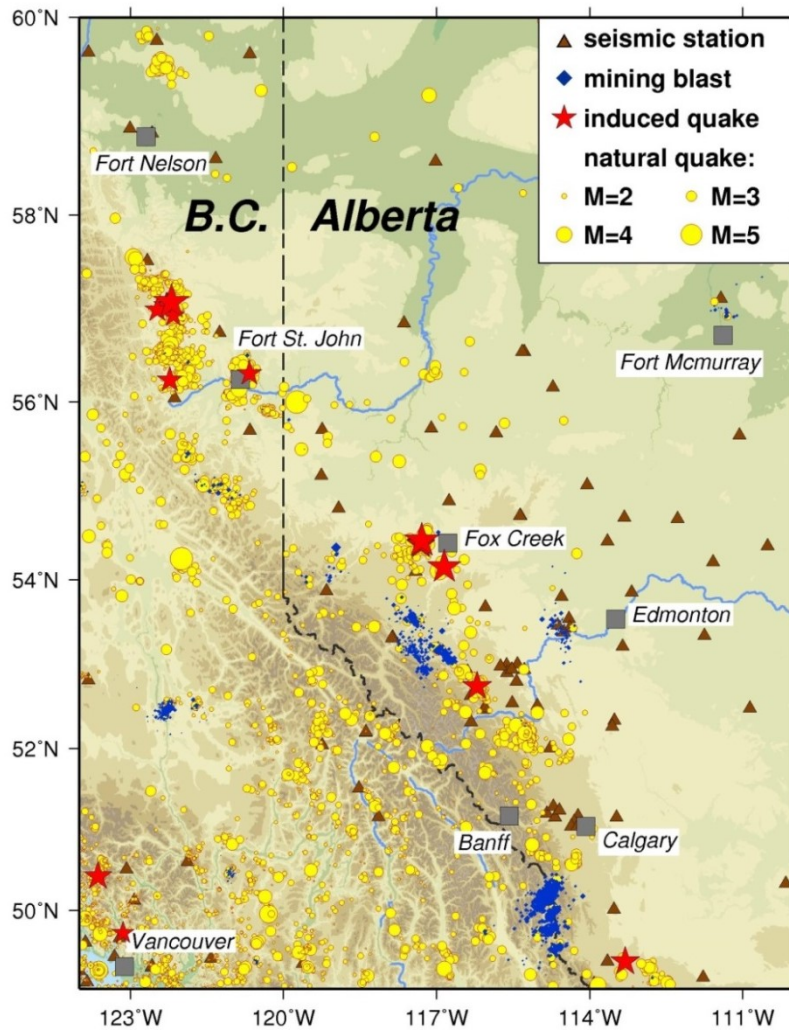


Figure 1.4: Distribution of earthquakes (1985-2017), mining blasts, and seismic stations (brown triangles, see Figure 1.3 for seismic network details) in the WCSB. Significant induced earthquakes are marked by the red stars, and mining blasts are shown as small blue diamonds.

1.2 Geological setting of the WCSB

Regardless of the nature of an event, intraplate earthquakes in the WCSB are all located within the upper crust, with most of their hypocenters being constrained to <10 km depth. Therefore, the

origin of all recent earthquakes in the WCSB can be attributed to the slippages of faults within the sedimentary layers and the upper section of the basement. This section gives a brief overview of the key characteristics for the shallow basin structures, with a special focus on the fault and stress conditions.

The WCSB is a foreland basin (Figure 1.5) that has undergone at least three major stages of development, with its initial origin dating back to 750 Ma ago. This involves 1) an initial stage as a passive intra-plate continent-ocean boundary until middle Devonian (~ 390 Ma); 2) a convergent inter-plate boundary until Jurassic (~185 Ma); and 3) foreland basin development until Tertiary or late Cretaceous (~ 90 Ma) due to the continuing cumulative convergence of the exotic terranes (Ross & Eaton 1999). Most of the mapped major thrust faults along the Canadian Cordillera are relatively young and formed during the last phase (i.e., terrane accretion; Monger & Price 2002). The current maximum crustal stress orientation (S_H) within the crust is aligned NE-SW throughout the basin (Heidbach *et al.* 2016), in alignment with the current absolute plate motion. The thickness of the sedimentary layers ranges from 0 km at exposed the Canadian Shield (east) to 6 km beneath the Rocky Mountains (west) (Hope *et al.* 1999). All the current oil and gas reservoirs were formed in the second phase, located at the depths up to 4 km (see section 1.3.2) (Green & Mountjoy 2005) while the basin fault systems likely originated earlier (i.e., deeper or even within the basement). In addition, the orientation for the fast axis of seismic anisotropy (NE) within the crust could be associated with the subsidence since middle Devonian (Lei Wu, personal communication, 2018).

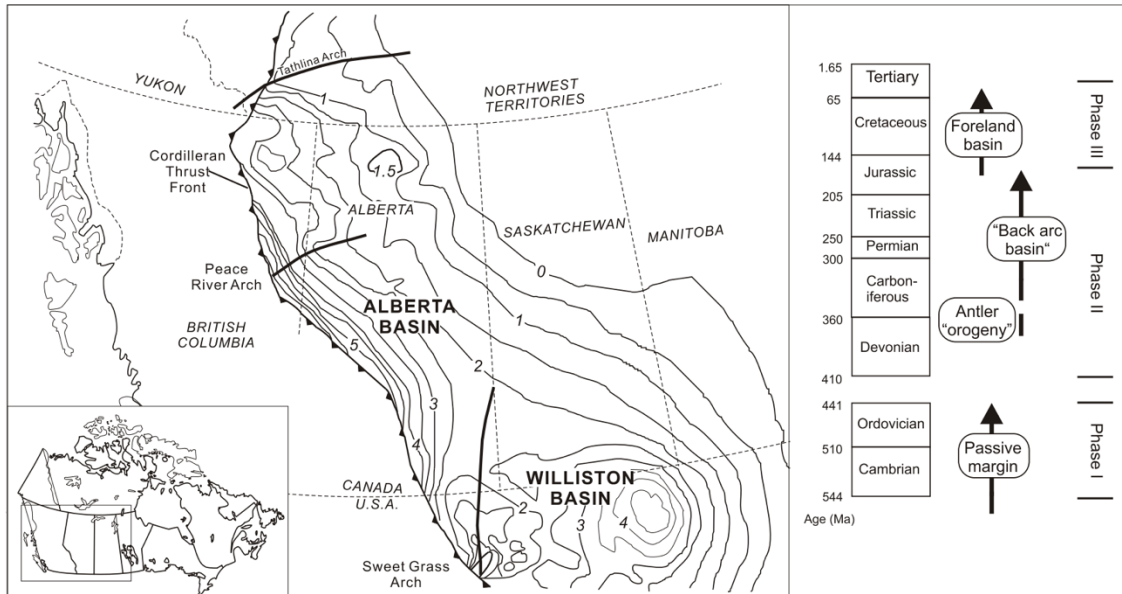


Figure 1.5: Isopach map of the WCSB showing the locations of the Alberta Basin and Williston Basin. The column on the right gives a general scheme for the evolution of Phanerozoic tectonic events recorded in the Cordillera that influenced sedimentation in the Alberta Basin. Figure from Ross and Eaton, 1999.

The Precambrian crust (thickness 36-48 km; Bouzidi *et al.* 2002) in the WCSB can be laterally subdivided into several domains based on their distinctive aeromagnetic measurements, with their collisional history dating back to at least 1.8-2.0 Ga (Hoffman 1988). Despite the lack of detailed maps of the basement faults, the anomalous (linear) features within the sedimentary section are less likely to be controlled by the basement structures, i.e., Precambrian structural fabrics within the crystalline basement (Ross & Eaton 1999). The boundary lines between different provinces do not necessarily indicate the location of potential faults, especially the small-scale, shallow faults that could be reactivated by industrial activities (see chapter 3 for details). More importantly, evidence shows that even detailed faults mapped by 3D seismic data are not the origin for recent intraplate earthquakes (Corlett *et al.* 2018; Eaton *et al.* 2018). Updated findings on the crustal and lithosphere structures beneath the western Laurentia can be found in Gu *et al.* (2018) and Chen *et al.* (2015b, 2017).

1.3 Industrial activities in the WCSB

1.3.1 Mining activities and wastewater disposal

Most of detected seismicity with $M_w \sim 2$ within the WCSB is mining blasts generated during by open-pit mine exploration (i.e., zero km event depth). Due to the relatively small magnitude and a lack of local monitoring, the events are typically recorded only by a few seismic stations, insufficient for waveform-based analysis. For example, frequency spectra of mining blasts (located within the mountains) show no delay-fired pattern² and the P-to-Surface wave amplitude ratio are generally comparable³ (Figure 1.6).

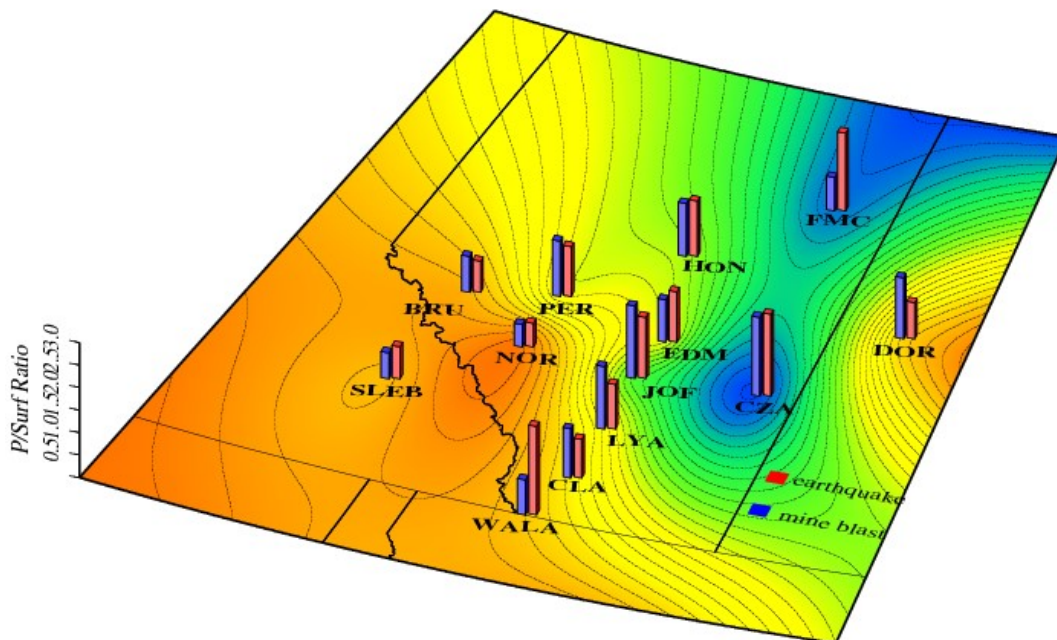


Figure 1.6: P-to-Surface wave amplitude ratio recorded at CRANE stations for earthquakes (red) and mining blasts (blue). The background is interpolated values from plotted stations.

² A clear separation in time that contains several explosions; source time function that have multiple peaks

³ Ideally, mining blasts (explosive seismic source) have stronger body wave, thus, relatively large P amplitude and low P-to-Surface wave amplitude ratio.

To date, classifications of mining blasts in the WCSB are mainly based on event time (Figure 1.7 and 1.8) and location (see Figure 1.4, also see section 2.2). Thus, I cannot rule out the possibility that mining-induced seismicity may exist and has been misinterpreted as mining blasts within the abovementioned clusters. In particular, events occurred in the early morning or late night are suspected of being induced (see Figure 1.7). To date, a few events have been identified as susceptible mining-induced earthquake during 2006-2010, while further investigation is required. Ideally, one should cross-check industry reports with recorded seismicity to verify the classification (e.g., Arrowsmith *et al.* 2006). Unfortunately, the blasting records are usually confidential, and remain inaccessible at the current time..

Many oil and gas exploration activities (i.e., mining, hydraulic-fracturing) are supplied with wastewater disposal (WWD), which is characterized by long duration continuous injection to deep high-permeability formations (Rubinstein & Mahani 2015). Within the WCSB, more than a thousand WWD wells have been drilled between 1985 and 2015, leading to an average monthly injection volume on the order of 10^3 m^3 , much less than that of Oklahoma (Atkinson *et al.* 2016; Ellsworth 2013). The disposal activity in Alberta mainly focuses on deeper formations: for example, the upper Rundel Group which is $\sim 3.9 \text{ km}$ deep and $\sim 2 \text{ km}$ above the crystalline basement (Schultz *et al.* 2017).

Unlike Oklahoma, wastewater disposal wells are rarely linked ($\sim 1\%$) with regional seismicity in the WCSB (Atkinson *et al.* 2016). The first (and only) confirmed a case of WWD induced cluster is located in the southern part of Alberta (Cordel Field; Schultz *et al.* 2014), showing a time lag of ~ 3 years (vs. several months in Oklahoma; also see Langenbruch & Zoback 2016). Among this cluster, the largest event was reported to be $M_L=3.5$, and this region has remained inactive since 2011. Since then, no more $M_L>3$ regional earthquakes have demonstrated a clear spatial-temporal relationship⁴ to a WWD well in and around the WCSB.

⁴ Earthquakes within 20 km of an injection well with a time delay showing correlation between injection volume and seismic rate (also see Schultz & Telesca 2018)

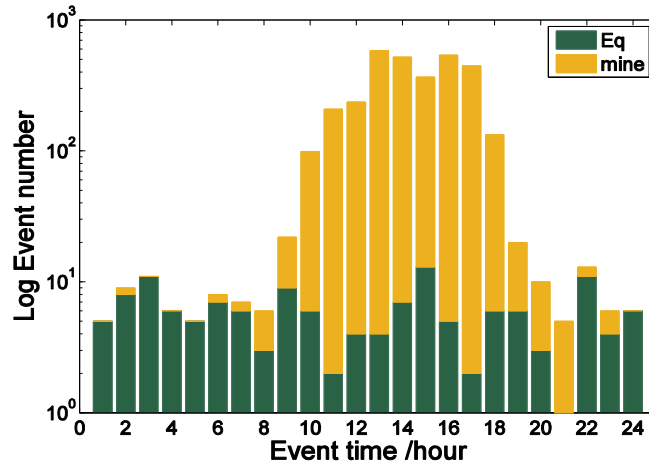


Figure 1.7: Time of day comparison for mining events and earthquakes activities in the southern WCSB (2006-2010). Eq-earthquake, mine-mining activities.

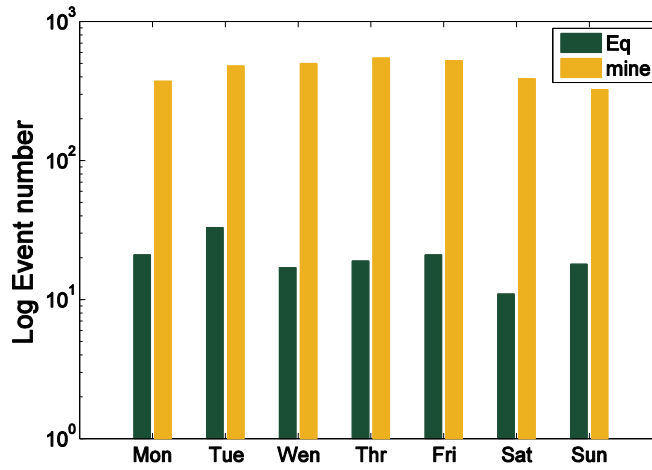


Figure 1.8: Day of week comparison for mining events and earthquakes activities in the southern WCSB (2006-2010). Eq-earthquake, mine-mining activities.

1.3.2 Multistage hydraulic fracturing

Since 2013, multistage HF operations, which require the drilling of horizontal wells and injection of fluid mixture underground, have been widely utilized in the WCSB (Atkinson *et al.* 2016; Wang *et al.* 2016; Schultz *et al.* 2015b). The horizontal well is usually more than 1 km long with a depth ranging from 1 to 4 km, depending on the targeting shale gas formations. Figure 1.9 illustrates how multistage HF works: the first step is to inject fluid to open fractures and let gas flow back during the second step. Characterized by high-rate and high-pressure injections, this procedure can take several weeks to fracture the shale rocks surrounding the well and generate $M_w < 0$ microseismic earthquakes. The total volume of fluid injected by a single well is on the order of 10^4 m^3 , while less than half of the fluid will flow back. For example, the percentage is only 7% for a well near Fox Creek (Bao & Eaton 2016).

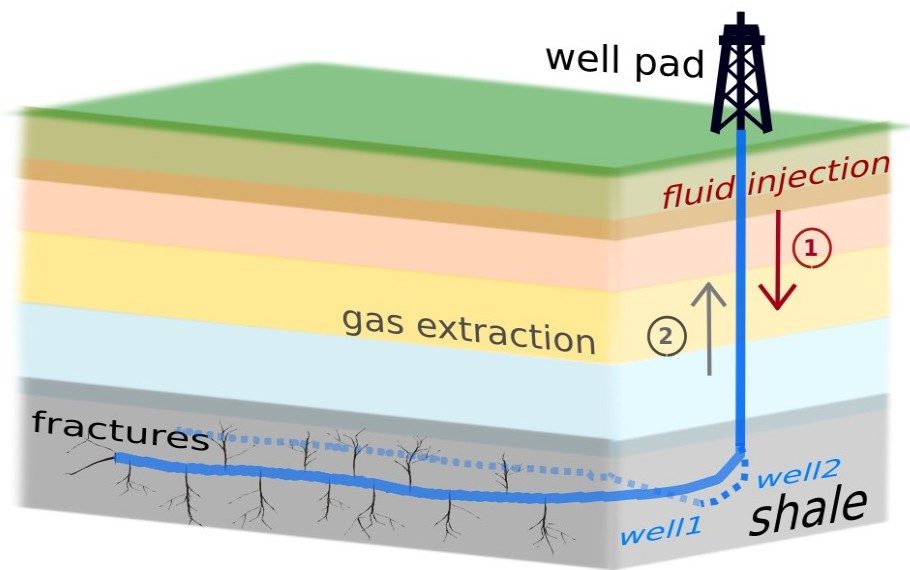


Figure 1.9: Schematic diagram for multistage hydraulic fracturing. A well is drilled down toward the targeted shale layer and then drilled horizontally along a layer.

In many cases, more than one well is drilled from a shared well pad (Figure 1.9 and 1.10; also see Schultz *et al.* 2018). Due to potential economic competition, detailed injection information is usually owned and withheld by oil and gas companies and is therefore unavailable to the public for at least 1 year after the well completion. Such confidentiality presents major challenges to the academic community during a real-time evaluation of potentially induced seismicity. Fortunately, partial ground motion information has been made available via the GeoSCOUT software and its licenses to Canadian universities⁵ (see Figure 1.10). The license and database are updated annually to provide basic header information of the wells in British Columbia, Alberta, and Saskatchewan.

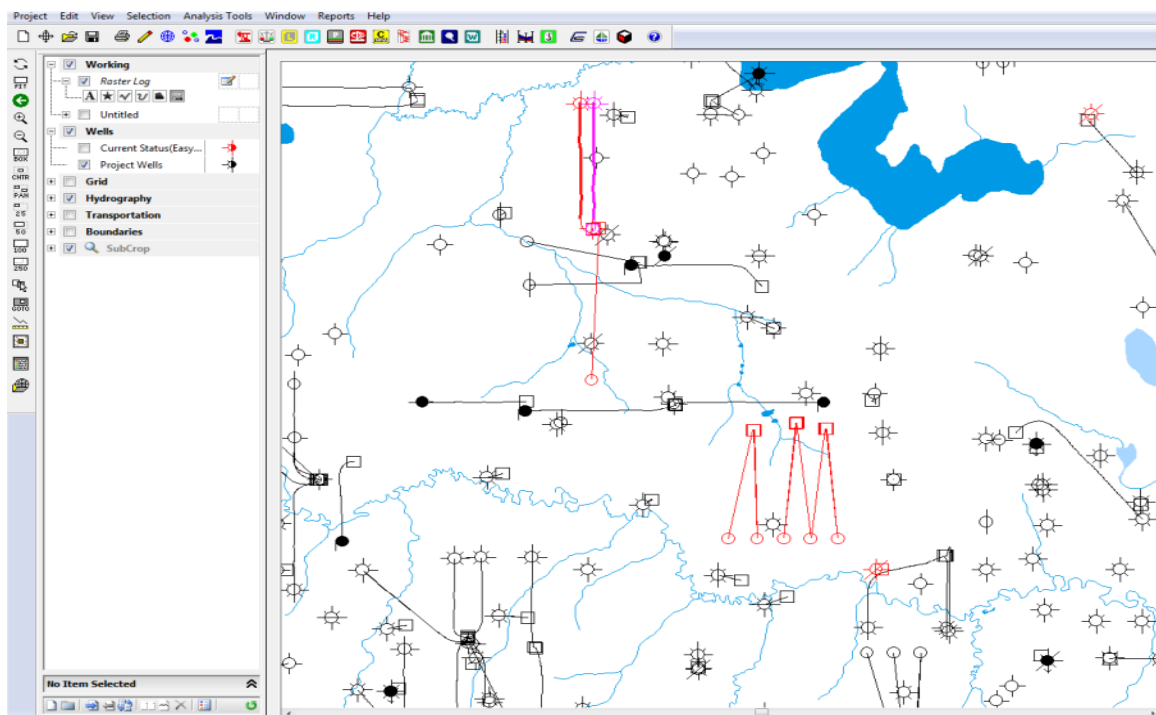


Figure 1.10: Screenshot of the interface of GeoSCOUT for a 10×10km area near Crooked Lake (blue). Injection wells are shown with circles and squares. For multistage hydraulic fracturing wells, the line connecting the well pads (squares) and well bottom (circles) represent the well extension projected on the surface. Recent wells (after 2015) are shown in red and selected well is highlighted in pink.

⁵ In particular, the GeoSCOUT software has been installed in the computer lab room located in the Earth Science Building for University of Alberta.

Major shale formations are located along the Rocky Mountains within the WCSB (Figure 1.11). On the one hand, shale permeability is greatly enhanced through the opening of fractures accompanied by microseismicity ($M_w < 0$). On the other hand, HF has been linked to a substantial increase in seismicity rate (which is calculated for hazard-related, regional earthquakes) since 2013 in the WCSB (Schultz *et al.* 2017; Wang *et al.* 2016; Atkinson *et al.* 2016, 2014). Induced earthquakes have been reported in the Horn River Basin, Montney, Duvernay, and Alberta Bakken (BCOGC 2012 2014; Schultz *et al.* 2015c), showing the maximum moment magnitude of 4.3 on the Montney formation in 2015. This Aug 17, 2015 earthquake represents the largest HF induced earthquake in North America and the second largest one of its kind worldwide (last updated Aug 2018).

To date, most HF induced earthquakes occurred on Montney and Duvernay, which has been suggested to be associated with their over-pressured nature (Eaton & Schultz 2018). Both formations are organic-rich and have hundreds of multistage HF wells operated by various oil companies. The Lower-Triassic Montney formation belongs to the Daiber Group and is characterized by shale (and silty shale) dominant contents supplied by a mix of siltstone and sandstone (Dixon 2000). The depth of Montney play is ~ 2 km, shallower than that of Duvernay (~ 3.5 km). In terms of the rock types, Montney contains a higher amount of sandstone than Duvernay. The Duvernay Formation formed in late Devonian and belongs to the Woodbend Group (Wendte & Uyeno 2005). The thickness of the Duvernay Formation varies mainly between 25 and 60 m in a broad region covering $\sim 56,000$ km² in total area (Davis & Karlen 2014; Dunn *et al.* 2012).

The exploitation of the Montney fairway⁶ mostly takes place in northern British Columbia, and only limited number of wells are drilled in west-central Alberta. To date, no induced earthquake associated with the Montney has been reported in Alberta. For this reason, provincial regulations (traffic-light system) have been introduced to monitor and control the potential seismic risk in two regions: (1) Montney in British Columbia and (2) Duvernay in Alberta.

⁶ A trend of particular geological feature, in this case, is hydrocarbon reservoir

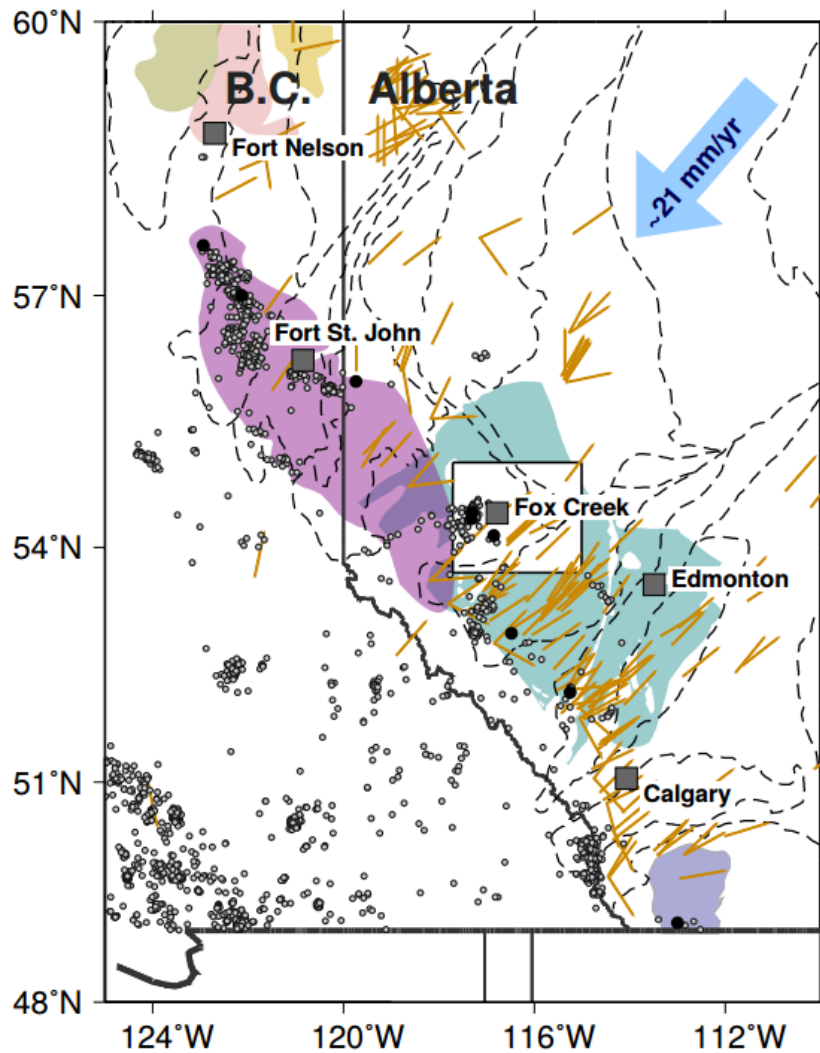


Figure 1.11: Major shale formations and maximum crustal stress orientation (S_H , yellow dashes) in the WCSB (Heidbach et al. 2016). From north to south the shale formations are commonly referred to as Liard Basin, Horn River Basin (Muskva formation), Cordova Embayment (ordered by color from left to right), Montney, Duvernay, Alberta Bakken (Rivard et al. 2014; BCOGC 2014, 2012). The earthquakes are shown by the small grey circles, and the tectonic boundaries in Alberta are marked by the dashed lines.

1.4 Thesis outline

The increasing seismicity raises many critical questions pertaining to the seismic risk assessment of shale gas exploration in the WCSB. A first step in the process of addressing some of these questions is an accurate determination of the source locations and their temporal relationship to the nearby industrial operations (section 1.2). Further understanding relies on the robustly resolved focal mechanisms, as well as knowledge of local geological background (section 1.3).

The rise of induced seismicity drives the enhancement of site-based seismic monitoring, which targets minor, repeating earthquakes between the two end members: microseismicity ($M_w < 0$) and potentially damaging earthquakes ($M_w > 5$). On the one hand, unique properties that defer from either category may be obtained: the key differences and similarities between microseismicity, induced seismicity, and tectonic earthquakes are under debate (e.g., Huang *et al.*, 2018; Dahm *et al.*, 2015). On the other hand, classic detection and imaging techniques can be adopted and applied to such datasets. Therefore, great research potential resides within investigating such regional data and bridging our knowledge gap between microseismicity and hazard dominating earthquakes.

This thesis focuses on the source properties of $M_w \sim 4$ earthquakes in the WCSB and other induced events worldwide. In this thesis, chapter 2 introduces several metrics used to determine and evaluate the focal mechanism as well as two cross-correlation based methods used to relocate repeating events. Determination of source parameters is based on the moment tensor analysis (i.e., Dreger 2003) that is assisted by additional detection/location methods (i.e., hypoDD, Waldhouser & Ellsworth, 2000; Match&Locate, Zhang *et al.*, 2015). To avoid repetitive information, the fundamentals of these methods are removed from chapter 3, 4 and 5 (in comparison with the published versions) while other event-based modification on the method and velocity model are introduced in these three chapters. Chapter 3 focuses on the first “red-light” event with detailed uncertainty evaluations (Wang *et al.* 2016). Chapter 4 presents an integrated analysis of the second “red-light” earthquake (Wang *et al.* 2017a, 2017b; Schultz *et al.* 2017). Chapter 5 expands my study scope and compares intraplate natural events with induced earthquakes in western Canada, with detailed discussion on the non-double-couple (non-DC) components (Wang *et al.* 2018). Chapter 6 summarizes the main findings in this thesis and offers suggestions and recommendations

for future work. The outcomes validated the induced nature of several events and had greatly contributed to the understanding of the morphology of reactivated critical-stage faults at a regional scale.

2 Data and Methods

2.1 Introduction

The work presented in this thesis focuses on the locations and mechanisms of seismic sources. The outcome will provide first-order constraints on the unmapped reactivated faults for induced seismicity. My analysis is data-driven and focuses on two main tasks: 1) determine the focal mechanism of the relatively larger magnitude earthquakes; 2) detect and locate the corresponding seismic cluster. The former undertaking targets potential fault orientations and reflects the anthropogenic contributions (e.g., fluid involvement for non-DC components) while the latter reveals potential spatial-temporal relationships between the industrial activities and near-site geological structures.

Considering the magnitude differences and data availability (Table 2.1), various methods are adopted to constrain the source properties: 1) hypocentral locations and full moment tensors of several earthquakes with $M_L > 4$ that are well resolved during both inversions (see section 2.1), forward modelling as well as P-wave first motion analysis; 2) dozens of events with M_L 2-3 are identified as “after-shocks” or “fore-shocks” and the detection of smaller events (e.g., in the Fox Creek area, see section 4.4.3); 3) other smaller events with insufficient station recording cannot be resolved with a robust focal mechanism, thus are only detected and located based on wave-form similarities. The magnitude and location information of all events are used for statistical analysis. In the following sections, I provide an overview of the key methods and packages for this thesis study. The moment tensor forward modeling and inversion and Match & Locate are waveform-based analysis, while the P wave first motion and double-difference relocation approach mainly consider the phase arrivals.

M_L	TDMT_INV	DC Forward Modelling	P-Wave Analysis	Detection
>4	yes	yes	yes	yes
3.5-4	maybe	yes	yes	yes
3-3.5	maybe	maybe	maybe	yes
2-3	no	maybe (if repeating)	maybe	yes
1-2	no	no	no	yes
<1	no	no	no	maybe (if repeating)
	low frequency < 0.5 Hz		high frequency > 0.5 Hz	

Table 2.1: Analysis approaches based on magnitudes.

2.2 Focal mechanism determination and moment tensor decomposition

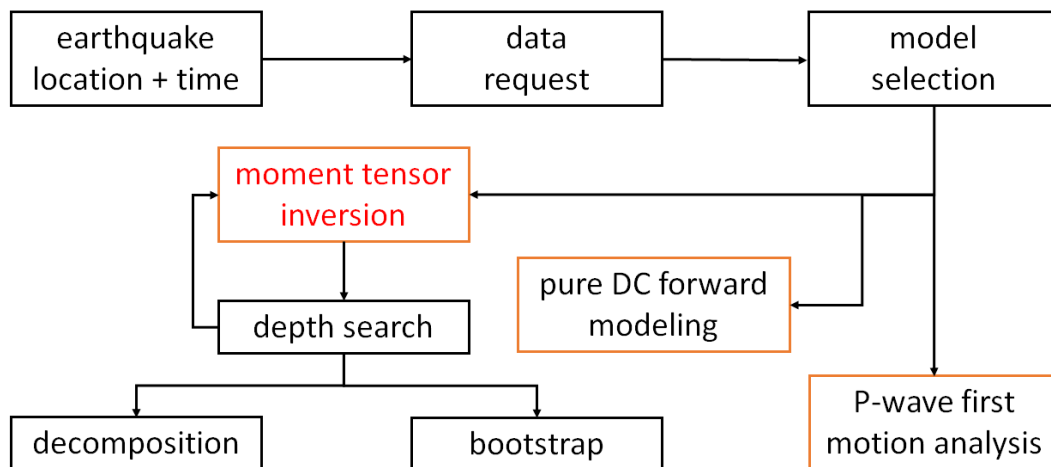


Figure 2.1: Flow diagram for moment tensor determination and validation. The depth search and bootstrap parts are presented and discussed with corresponding events in chapters 3-5.

Figure 2.1 illustrates my integrated approach to determine the moment tensor of a given event. After collecting the broadband waveforms from all available regional network stations, I carefully select a subsurface structure model from earlier seismic surveys based on source-station distribution. Based on the quality of the recorded waveform I separate them into three categories: 1) high quality (mostly $M_w > 3.5$) events for full moment tensor determinations, 2) solid quality events susceptible to forward moment tensor modeling, and 3) events that are unsuitable for source mechanism determination. For category 2 earthquake I use a grid search method to determine a pure DC solution. For both categories 1 and 2, I independently measure the first P wave motion (see section 2.1.1) to verify the outcomes of the moment tensors. A break-down of the events is given in Table 2.1.

A stable moment tensor analysis requires information on the approximate earthquake location and timing. In this thesis, the location and on-set time of an earthquake are obtained from near-real-time online catalogs including NRC (Earthquake Canada); NMX (Nanometrics Athena); SLU (Saint-Louis University Earthquake Centre); USGS (United States Geological Survey). The USGS reports $M_L > 4$ events and NRC provide alerts for $M_L > \sim 3.5$ due to the limited seismic network used during automatic detection. Earthquakes around $M_L = 3$ can be searched via online searching engine (Earthquake Canada) while the catalog for smaller ones may be incomplete. I also incorporate SAC header information for several potentially induced earthquakes, once all the potential reports are collected for earthquakes, their locations are compared, and a preferred (e.g., effective averaged) location is used for the initial run.

To compute the Green's functions, I adopt a one-dimensional velocity model consisted of 14 layers (Figure 2.2). The upper crust in this model is modified from Welford & Clowes (2006) based on an active source experiment. The lower crust velocity model is from the recent receiver function analysis (Chen *et al.* 2015b) beneath station PER (Gu *et al.* 2011). The attenuation model is modified from Zelt & Ellis (1990) by Wang *et al.* (2016), and the forward waveforms are computed using a frequency-wavenumber integration approach (Saikia 1994). This calculation was repeated for all depths (1-10 km), and a Green's functions database (with a sample rate of 0.5s) was generated for stations from 30-700 km with the model shown in Figure 2.2. This database is used as the backbone for most regional moment tensor inversions, supplemented by event-based

adjustments on the model/sample rate (i.e., 0.2s for stations < 30 km and filtered with higher frequency ranges).

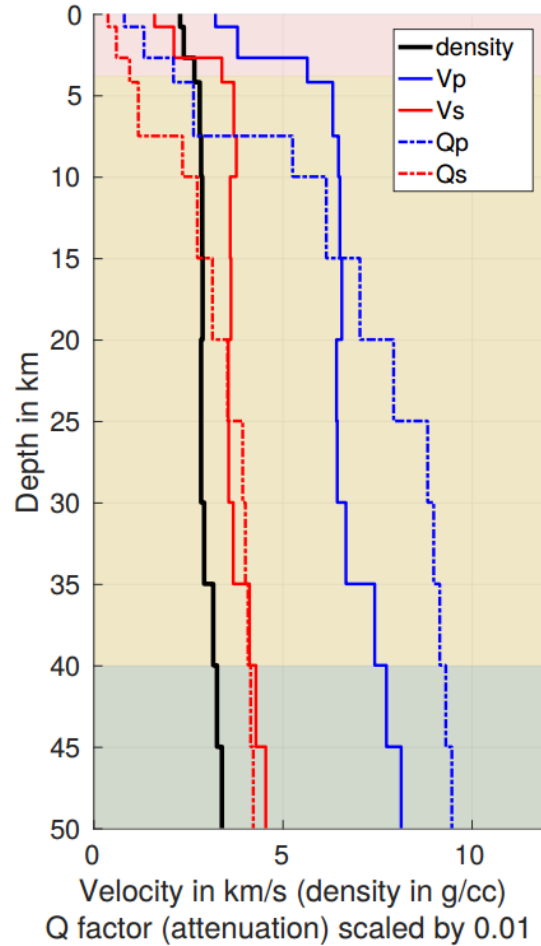


Figure 2.2: 1D structure model used for full moment tensor inversion. The sedimentary layer is colored in red, and the upper mantle is colored in green. The velocity (V_p cmb, V_s cmb) and density model was resolved by Chen et al. (2015b; station PER). The attenuation model (Q_p , Q_s) is modified from Zelt and Ellis (1990).

2.2.1 P-wave first motion determination

P-wave (Pn or Pg phases) is the usually first arrival received at seismic stations. Therefore, its polarity and amplitude directly reflect the stress alternation when an earthquake indicated (Figure 2.3). For example, compressive stress will lead to a “push” at seismometer and leads to positive displacement (Figure 2.4). Different from surface waves, which travels along the surface plane, the P-wave dives into the subsurface and are recorded with an incident angle. In this thesis, the incidence angles are calculated using the regional velocity model (see Figure 2.2) with Taup (Cortwell *et al.* 1999). When plotting the polarities on a “beachball”, stations with larger incidence angles (far-source) will be presented closer the center of a “beachball” and vice versa. Thus, robust polarities recorded by near-source stations are critical to determining the focal mechanism. With sufficient station coverage, each station is plotted as a dot on an empty “beachball” and provides constraints on the potential fault plane orientations (see Figure 2.3). The amplitude information could also be included to invert the focal mechanism using P-wave first motions since the receiver closer to the strike orientation will record smaller displacement. Due to relatively low SNR⁷, this thesis does not consider the amplitudes of P-wave first motion and only uses the polarities to validate results from moment tensor inversions.

⁷ Signal-to-noise ratio: in this thesis all SNR are calculated using `sac_snr` (written by Dr. Zhigang Peng), which is defined as ratio for the standard variation within the signal and noise window.

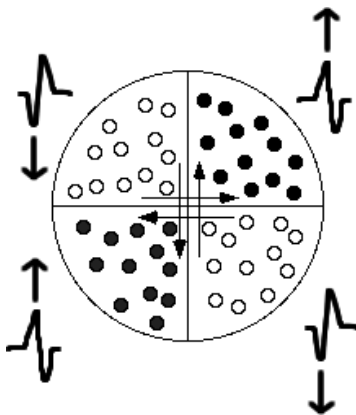


Figure 2.3: First motion received at seismometer. Filled dots represent compressional (positive onset of the waveform) and open dots represent dilatational (negative onset of the waveform). Figure credit from USGS Earthquake Glossary.

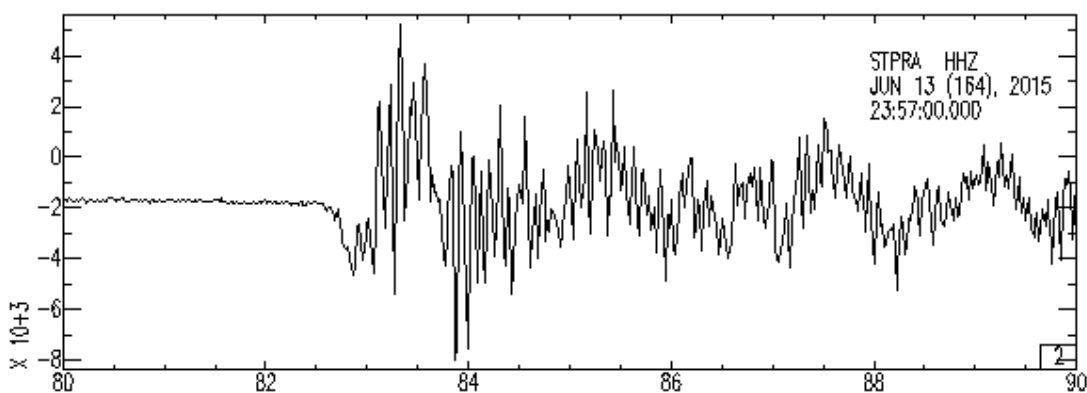


Figure 2.4: Example for negative (dilatational) P-wave first motion: showing the Mw3.9 earthquake received by a RAVEN station (STPRA) at azimuth = 21°, distance = 181 km.

2.2.2 Full moment tensor inversion and forward modeling

Throughout this thesis, the earthquake source is assumed as a spatial and temporal point-source (as calculated in FKRPROG package; also see Saikia *et al.* 1994). Based on the monitoring geometry (see Figure 1.3), the source-station distances are also sufficient to approximate the earthquake as a point source (Honda, 1962). For a single point source, stress distribution can be fully described by a 3×3 matrix, which is named moment tensor (\mathbf{M}) (Aki & Richards 1980). In

the following text bold capitalized letter (e.g., \mathbf{M}) represent a matrix, bold uncapitalized letter represent a vector (e.g., \mathbf{d}_z).

$$\mathbf{M} = \begin{bmatrix} M_{xx} & M_{xy} & M_{xz} \\ M_{yx} & M_{yy} & M_{yz} \\ M_{zx} & M_{zy} & M_{zz} \end{bmatrix} \text{ (dyne}\cdot\text{cm, or N}\cdot\text{m) ,} \quad (1)$$

where, x, y, and z denote the directions (Shearer 1998). Each element in this matrix represents a pair of force couple applied on a plane pointing toward a direction. Since seismic moment tensor is real and symmetric ($M_{xy} = M_{yx}$, $M_{xz} = M_{zx}$, $M_{yz} = M_{zy}$), only six elements (scalars) are required to fully describe the time independent source mechanism. Special cases for the moment tensors exist when certain element(s) vanishes. Those are discussed later in the section 2.2.3.

For a single seismic station, data are recorded as velocity variations over time in three orthogonal orientations. One can remove instrument responses, filter and transfer those velocity recordings into displacements (\mathbf{d}) in SAC (Seismic Analysis Code). The three components are also rotated from the geographical coordinate (e.g., N for the north component, E for east component and Z for vertical component) to a new system relative to wave path, based on the locations of a seismic source and station. After the rotation, the seismic recordings $\mathbf{d}_z, \mathbf{d}_r, \mathbf{d}_t$ (unit: cm, or m) at a seismic station are denoted by vertical (z), radial (r) and tangential (t):

$$\begin{aligned} \mathbf{d}_z &= \mathbf{zee} \cdot A_1 + \mathbf{zds} \cdot A_2 + \mathbf{zdd} \cdot A_3 + (\mathbf{zep} \cdot m_{iso}) \\ \mathbf{d}_r &= \mathbf{rss} \cdot A_1 + \mathbf{rds} \cdot A_2 + \mathbf{rdd} \cdot A_3 + (\mathbf{rep} \cdot m_{iso}) \\ \mathbf{d}_t &= \mathbf{tss} \cdot A_4 + \mathbf{zdd} \cdot A_5 , \end{aligned} \quad (2)$$

where $m_{iso} = tr(\mathbf{M})/3$, is the isotropic (explosion or implosion) coefficient; $\mathbf{zss}, \mathbf{zds}, \mathbf{zdd}, \mathbf{rss}, \mathbf{rds}, \mathbf{rdd}, \mathbf{tss}, \mathbf{tds}, \mathbf{zep}$, and \mathbf{rep} represent ten⁸ Green's functions as functions of time (or frequency, for frequency domain moment tensor inversion). In those ten Green's functions (unit 1/dyne, or 1/N), "ss", "ds", "dd" are the vertical strike-slip, vertical dip-

⁸ten for layered model, if not, a complete set contains 27 functions.

slip and 45° dip-slip Green's functions, reprehensively; “ep” is the explosion Green's function (Aki & Richards 1980). When the velocity model is assumed to be one dimensional, Green's functions are functions of source-receiver distance and azimuth (az). The Greens' function in this thesis is calculated using the frequency-wavenumber integration software (FKPROG, Saikia, 1994) and a regional 1-D velocity model as input (see Figure 2.2). In equation (2), A_i represents the stress field caused by certain source force and are a linear combination of moment tensors defined in equation (3).

$$\begin{aligned}
 A_1 &= \frac{1}{2}(M_{xx} - M_{yy}) \cdot \cos(2az) + M_{xy} \cdot \sin(2az) \\
 A_2 &= M_{zz} \cdot \cos(az) + M_{yz} \cdot \sin(az) \\
 A_3 &= -\frac{1}{2}(M_{zz} + M_{yy}) \\
 A_4 &= \frac{1}{2}(M_{xx} - M_{yy}) \cdot \sin(2az) - M_{xy} \cdot \cos(2az) \\
 A_5 &= M_{yz} \cdot \cos(az) + M_{zz} \cdot \sin(az) .
 \end{aligned} \tag{3}$$

Equation (3) is the expression for A_i generated from equation (2) without considering M_{iso} terms for vertical and radial displacement, which is commonly used for the traditional method, as explained by Jost & Herrmann (1989). However, when the isotropic contribution to displacements in those two directions is included, the coefficient A_3 should be expressed as:

$$A_3 = -\frac{1}{6}(M_{xx} + M_{yy} - 2M_{zz}) . \tag{4}$$

This correction was made by Minson & Dreger (2008), which is referred as the stable inversions for complete moment tensors method⁹. Combining and rearranging the above equations (2-4), the

⁹ note that sources without isotropic part (CLVD and DC) are not affected because when $M_{xx} + M_{yy} + M_{zz} = 0$, both methods yield the same results.

displacement at free surface (received by the seismic station) can be expressed as a sum of moment tensor elements times the corresponding Green's functions:

$$\begin{aligned}
\mathbf{d}_z = & M_{xx} \left[\frac{\mathbf{zss}}{2} \cdot \cos(2az) - \frac{\mathbf{zdd}}{6} + \frac{\mathbf{zep}}{3} \right] \\
& + M_{yy} \left[-\frac{\mathbf{zss}}{2} \cdot \cos(2az) - \frac{\mathbf{zdd}}{6} + \frac{\mathbf{zep}}{3} \right] \\
& + M_{zz} \left[\frac{\mathbf{zdd}}{3} + \frac{\mathbf{zep}}{3} \right] + M_{xy} [\mathbf{zss} \cdot \sin(2az)] \\
& + M_{xz} [\mathbf{zds} \cdot \cos(az)] + M_{yz} [\mathbf{zds} \cdot \sin(az)]
\end{aligned} \tag{5}$$

$$\begin{aligned}
\mathbf{d}_r = & M_{xx} \left[\frac{\mathbf{rss}}{2} \cdot \cos(2az) - \frac{\mathbf{rdd}}{6} + \frac{\mathbf{rep}}{3} \right] \\
& + M_{yy} \left[-\frac{\mathbf{rss}}{2} \cdot \cos(2az) - \frac{\mathbf{rdd}}{6} + \frac{\mathbf{rep}}{3} \right] \\
& + M_{zz} \left[\frac{\mathbf{rdd}}{3} + \frac{\mathbf{rep}}{3} \right] + M_{xy} [\mathbf{rss} \cdot \sin(2az)] \\
& + M_{xz} [\mathbf{rds} \cdot \cos(az)] + M_{yz} [\mathbf{rds} \cdot \sin(az)]
\end{aligned} \tag{6}$$

$$\begin{aligned}
\mathbf{d}_t = & M_{xx} \left[\frac{\mathbf{tss}}{2} \cdot \sin(2az) \right] \\
& + M_{yy} \left[-\frac{\mathbf{tss}}{2} \cdot \sin(2az) \right] \\
& + M_{xy} [-\mathbf{tss} \cdot \cos(2az)] \\
& + M_{xz} [\mathbf{tds} \cdot \cos(az)] \\
& + M_{yz} [-\mathbf{tds} \cdot \sin(az)].
\end{aligned} \tag{7}$$

Note that equations (5-7) are different from equation A5.4-A5.5 by Jost & Herrmann (1989), to take the isotropic component into the inversion problem (Minson & Dreger, 2008). Combining equation (3-7) and include all (n) stations, the inversion problem is set up as:

$$\mathbf{d} = [\omega_1 \mathbf{d}_1 \quad \omega_2 \mathbf{d}_2 \quad \dots \quad \omega_n \mathbf{d}_n] = \begin{bmatrix} \omega_1 \mathbf{G}_1 \\ \omega_2 \mathbf{G}_2 \\ \vdots \\ \omega_n \mathbf{G}_n \end{bmatrix} \begin{bmatrix} M_{xx} \\ M_{yy} \\ M_{zz} \\ M_{xy} \\ M_{xz} \\ M_{yz} \end{bmatrix} = \mathbf{G} \mathbf{m}, \quad (8)$$

where $\mathbf{d}_n = [\mathbf{d}_z \ \mathbf{d}_r \ \mathbf{d}_t](3l_n \times 1)$ is the data vector, ω_n is the weight and \mathbf{G}_n ($3l_n \times 6$) is the coefficient matrix for the n_{th} station (l_n is the length of time samples for the n_{th} station). Therefore, \mathbf{d} is a vector of $N \times 1$ ($N = \sum_1^n (3 \times l_n)$, total length for all three-component recordings) and our goal is to invert for the \mathbf{m} vector (6×1):

Equation (8) can be further expanded by breaking one station into more: treating different seismic phases (i.e., body waves and surface waves) as recordings at “another station” with same \mathbf{G}_n while a different weight (ω_n) (i.e., “Cut and Paste”; see Zhu *et al.* 1997 and Zhang *et al.* 2013). Usually, high-frequency body waves are weighted higher to overcome their higher attenuation and smaller amplitude than surface waves. The inversion procedure is simply defined as:

$$\mathbf{m}_{sol} = (\mathbf{G}^T \mathbf{G})^{-1} \mathbf{G}^T \mathbf{d}. \quad (9)$$

From equation (8), it is obvious that the moment tensor inversion is an overdetermined problem and no damping is introduced. To compare and validate the inversion results, I determine the pure DC moment tensors from forward modeling (Kim *et al.* 2011) by searching over all possible strike, dip, and rake angles with a uniform step size of 5 degrees. Both the input data and Green’s functions are the same as moment tensor inversion. The forward modeling can only model purely DC focal mechanisms. For a purely double-couple source, \mathbf{m} only contains four independent variables (rather than six, for a full moment tensor). Thus, a set of double couple moment tensors (\mathbf{m}_{fwd}) can be generated from different combinations of strike, slip, and dipping angles, as well as the size of the seismic source (seismic moment m_0). The corresponding synthetic displacement seismic record is then calculated as $\mathbf{s} = \mathbf{G} \mathbf{m}_{fwd}$.

The quality of the waveform matching is assessed through the variance reduction (VR) and normalized residual (RES/Pdc) (Pasyanos *et al.* 1996) defined as follows:

$$VR = \left[1 - \frac{\sum_{i=1}^N (d_i - s_i)^2}{\sum_{i=1}^N d_i^2} \right] \cdot 100\% \quad (10)$$

$$RES/Pdc = \frac{\sum_{i=1}^N (d_i - s_i)^2}{\sum_{i=1}^N d_i^2 \cdot Pdc}, \quad (11)$$

where d_i and s_i are the i_{th} elements of the concatenated data (\mathbf{d}) and synthetic ($\mathbf{s} = \mathbf{G}\mathbf{m}_{sol}$) time series, respectively, and Pdc is the percentage of DC moment tensor decomposition (see section 2.2.3 for calculation). For the forward modelling approach, the \mathbf{m}_{fwd} that produce the highest VR is kept as the optimal solution.

Considering the large variances in earthquake magnitudes and source-station distances (Figure 2.5) multiple frequency ranges (0.08-0.4 Hz and 0.05-0.1 Hz) are adopted during the moment tensor inversion to ensure relatively high SNR and robust inversion. More than 4 and 12 three-component recordings are used for $M_w > 3$ and $M_w > 4$, respectively. When both frequency ranges are acceptable, the higher one is kept to maximize the energy of body wave by varying the weights of the individual waveforms based on both source-station distances and the relative amplitude in the corresponding frequency ranges.

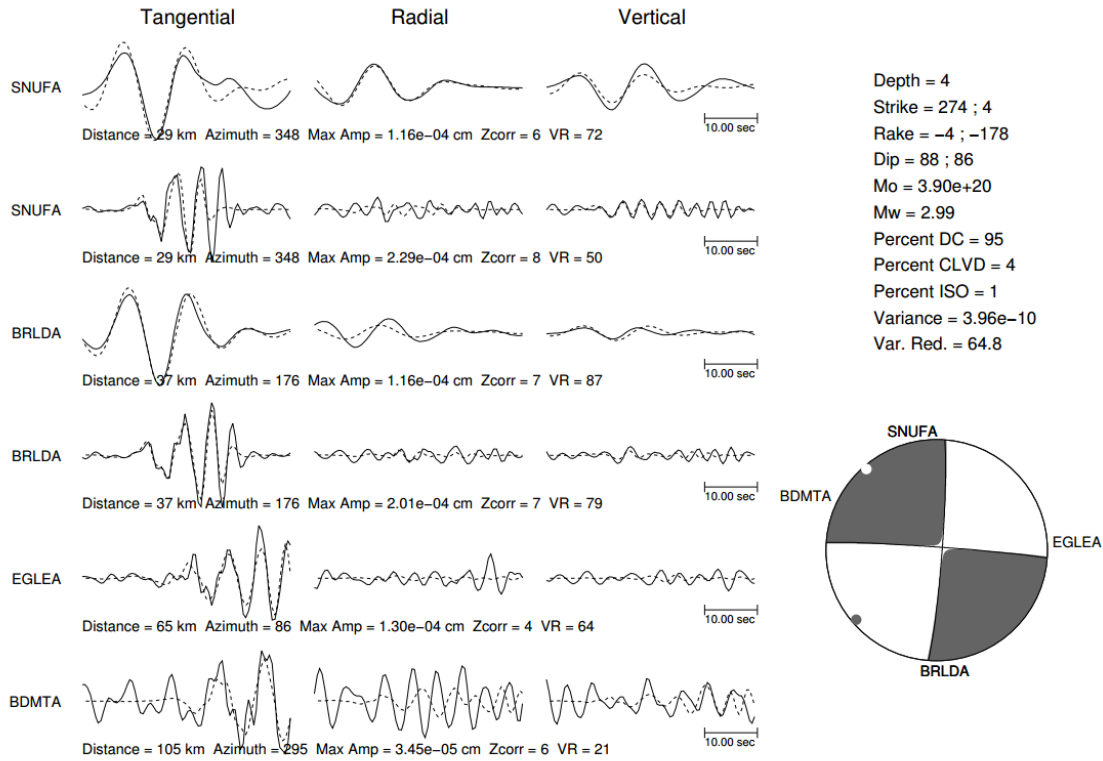


Figure 2.5: Example of output ($M_w=3$) for the full moment tensor inversion (TDMT_INV) program. Note that station BRLDA and SNUFA have both high and low-frequency ranges used while other stations are left with only high-frequency ranges due to the relatively low signal-to-noise ratio in low-frequency range.

2.2.3 Moment tensor decomposition and display

When decomposing a given moment tensor, the isotropic part can be uniquely determined and separated from the deviatoric part. However, further calculations of the percentage and property for various components of the deviatoric part are non-unique and can be conducted in many different ways. A common approach is to separate it into a major DC and an orthogonal compensated-linear-vector-dipole (CLVD) tensor (Jost & Herrman 1989; Chapman & Leaney 2012):

$$\mathbf{M} = \begin{bmatrix} M_{xx} & M_{xy} & M_{xz} \\ M_{yx} & M_{yy} & M_{yz} \\ M_{zx} & M_{zy} & M_{zz} \end{bmatrix} = \mathbf{M}_{iso} + \mathbf{M}_{dev}. \quad (12)$$

The decomposition is accomplished by eigenvalue decomposition:

$$\mathbf{A} \cdot \begin{bmatrix} \lambda_1 & 0 & 0 \\ 0 & \lambda_2 & 0 \\ 0 & 0 & \lambda_3 \end{bmatrix} \mathbf{A}^T = \begin{bmatrix} m_{iso} & 0 & 0 \\ 0 & m_{iso} & 0 \\ 0 & 0 & m_{iso} \end{bmatrix} + \mathbf{A} \cdot \begin{bmatrix} \lambda_1^* & 0 & 0 \\ 0 & \lambda_2^* & 0 \\ 0 & 0 & \lambda_3^* \end{bmatrix} \cdot \mathbf{A}^T \quad (13)$$

Again, $m_{iso} = \frac{m_1+m_2+m_3}{3} = \frac{tr(\mathbf{M})}{3}$ and \mathbf{A} is the matrix contains all three eigenvectors:

$$\mathbf{A} = \begin{bmatrix} a_{1x} & a_{1y} & a_{1z} \\ a_{2x} & a_{2y} & a_{2z} \\ a_{3x} & a_{3y} & a_{3z} \end{bmatrix} \quad (14)$$

and \mathbf{M}_{dev} is the deviatoric part of a full moment tensor:

$$\mathbf{M}_{dev} = \begin{bmatrix} \widehat{M}_{xx} & \widehat{M}_{xy} & \widehat{M}_{xz} \\ \widehat{M}_{yx} & \widehat{M}_{yy} & \widehat{M}_{yz} \\ \widehat{M}_{zx} & \widehat{M}_{zy} & \widehat{M}_{zz} \end{bmatrix} \quad (15)$$

with $\widehat{M}_{xx} + \widehat{M}_{yy} + \widehat{M}_{zz} = 0$. \mathbf{M}_{dev} can be further decomposed into a best DC (\mathbf{M}_{dc}) and CLVD (\mathbf{M}_{clvd}) components by rearranging the eigenvalues to $\lambda_{min}, \lambda_{mid}, \lambda_{max}$, based on the absolute values of $\lambda_1^*, \lambda_2^*, \lambda_3^*$ and the corresponding eigenvectors are $\mathbf{a}_1^*, \mathbf{a}_2^*, \mathbf{a}_3^*$, which represents the three rows in \mathbf{A} . Let us first define the ratio ε :

$$\varepsilon = \left| \frac{\lambda_{min}}{\lambda_{max}} \right| = -\frac{\lambda_{min}}{\lambda_{max}}. \quad (16)$$

Equation (16) is always true since $\lambda_1^* + \lambda_2^* + \lambda_3^* = \lambda_{min} + \lambda_{mid} + \lambda_{max} = 0$. Calculation for the percentages of ISO, CLVD and best DC in percentages is shown below:

$$\begin{aligned}
P_{iso} &= \frac{|m_{iso}|}{|\lambda_{max}| + |m_{iso}|} \times 100\% \\
P_{ctvd} &= 2\varepsilon \times (100\% - P_{iso}) \\
P_{dc} &= (1 - 2\varepsilon) \times (100\% - P_{iso}) .
\end{aligned}
\tag{17}$$

The definition of P_{iso} from Bowers & Hudson (1999) is used in this thesis and is consistent with the source-type plot used by Hudson (1998).

Alternatively, similar major DC can be maximized and extracted while the rest is represented by a minor DC (Jost & Herrman 1989):

$$\mathbf{M}_{dev} = \mathbf{M}_{dc1} + \mathbf{M}_{dc2} .
\tag{18}$$

Four more decomposition methods can be carried out in a similar concept by constraining the physical type of each decomposed components while they are hardly linked to sound geologic or physical meanings (Figure 2.6). I refer the readers to Jost & Herrman (1989) and Vavryčuk (2014) for more details.

20140809 M=3.8

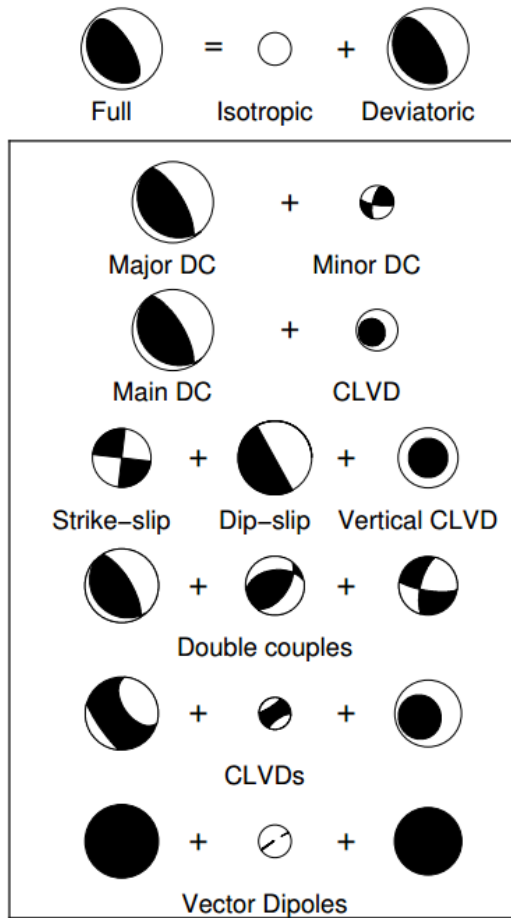


Figure 2.6: Example of different moment tensor decomposition methods. The deviatoric part could be decomposed into six different combinations shown in the box. The first two methods are chosen and interpreted in the main text (see chapter 5).

It worth noting that the Cartesian system (coordinates marked by “xyz”) is used for all above equations and illustrations, another popular coordinate in source seismology is the rtp¹⁰ (or rtf) system (i.e., GCMT solutions). One should pay extra attention to this when calibrating various source of moment tensors and plotting the focal mechanisms (e.g., use “psmecha” in GMT). The conversion between the two systems are:

$$\begin{aligned}
 M_{rr} &= M_{zz} \\
 M_{tt} &= M_{xx} \\
 M_{ff} &= M_{yy} \\
 M_{rt} &= M_{xz} \\
 M_{rf} &= -M_{yz} \\
 M_{tf} &= -M_{xz} .
 \end{aligned}
 \tag{19}$$

This conventional decomposition has been widely used to generate source-type plots. For example, Hudson *et al.* (1989) proposed the symmetric plot to present negative/positive ISO as well as CLVD at four corners of a skewed diamond shape and remain the DC components in the center. Alternative source-type plots are also developed while no method show a significant advantage over one another (Vavryčuk 2014; Tape & Tape 2012). In addition, seismic potency sensor decomposition is proposed as a more reliable metric than the above-presented moment tensor decomposition and yields different percentages of non-DC components (Zhu & Ben-Zion 2013). The potential inconsistency between various methods should be more concerning if one uses gCAP for moment tensor inversion and wants to compare with the output from TDMT_INV (as well as the majority of online available full moment tensor decomposition results), since the recent version of gCAP adopted the updated decomposition method (Zhu & Ben-Zion 2013). In this thesis, I adopt the classic/traditional decomposition method in chapter 5 to ensure my results

¹⁰ r=upper, t=south, p=east; for the Cartesian system, x=north, y=east, z=down. See Aki & Richard 1980.

comparable and consistent with previous studies. It should be noted that the choice of the source-type plot, as well as decomposition method, have no effect our discussion or conclusion.

2.3 Cross-correlation based cluster location

Accurate location is vital for spatial based analysis of seismic clusters. In this thesis, most events with $M_L > 2$ detected by a regional network (see Figure 1.3) are relocated with hypoDD (Waldhauser & Ellsworth 2000), and smaller events are detected and located with M&L¹¹ (Zhang & Wen 2015a).

2.3.1 Double difference relocation (HypoDD)

Once detected and categorized as multiples, the location of clustered events can be refined by a double-difference relocation approach (Waldhauser & Ellsworth 2000). In general, the code tends to tighten a cluster based on the physical assumption that repeating (similar) earthquakes occur on shared fault(s). Thus, the different travel time for a pair of earthquakes can be attributed to the small (i.e., compare to the source-station distance) spatial offset between them. The name “double-difference” comes from the two steps of calculations:

$$dr_k^{ij} = (t_k^i - t_k^j)^{obs} - (t_k^i - t_k^j)^{cal}. \quad (20)$$

In the first step, travel time differences between a pair (i_{th}, j_{th}) of similar earthquakes are calculated ($t_k^i - t_k^j$); in the second step, the differential travel time data of all pairs are used to determine/refine the hypocenter locations of a seismic cluster. The inversion problem is set up to minimize the differences (residuals) between observed and calculated travel-time differences (Equation 20). The hypoDD method is sensitive to the input preliminary locations, and the outputs should be treated as relative relocations instead of improvements on the absolute initial locations. Damping parameters are added at the end of the (sparse) matrix containing all pairs of observed time differences during the inversion (matrix regularization). The package also permits shifts on

¹¹ Cross-correlation based, grid-search method to capture smaller event using template (usually larger) event determine the event time and location simultaneously. See Zhang & Wen 2015a for details on method. Package available via request to Dr. Miao Zhang.

the center of relocated cluster(s). Thus, the relocated cluster may not be located exactly on the ruptured faults and requires reconciling, I refer readers to Waldhouse & Ellsworth (2000) for more details on the method as well as the use of the hypoDD package.

Confined locations and depths can provide critical information on (1) identifying if an event is a mining blast or mining-induced earthquake, (2) comparing the depth of hydraulic-fracturing simulations and the possible induced earthquake and (3) determining the true fault orientation (i.e., discriminate the true and auxiliary fault plane from focal mechanism analysis). Figure 2.7-2.8 shows the relocation of the “mining blasts” in southern Alberta, which can be clearly divided into five independent clusters that overlap with five known open-pit coal mines: Fording river, Greenhills, Elkviews, Line Creek and Coal Mountain (Figure 2.8, from top to bottom). In this thesis, the locations of clustered regional events are supplied by the outputs from hypoDD. In particular, detailed discussion and location of HF induced clusters around the Crooked Lake are presented in Schultz *et al.* (2017).

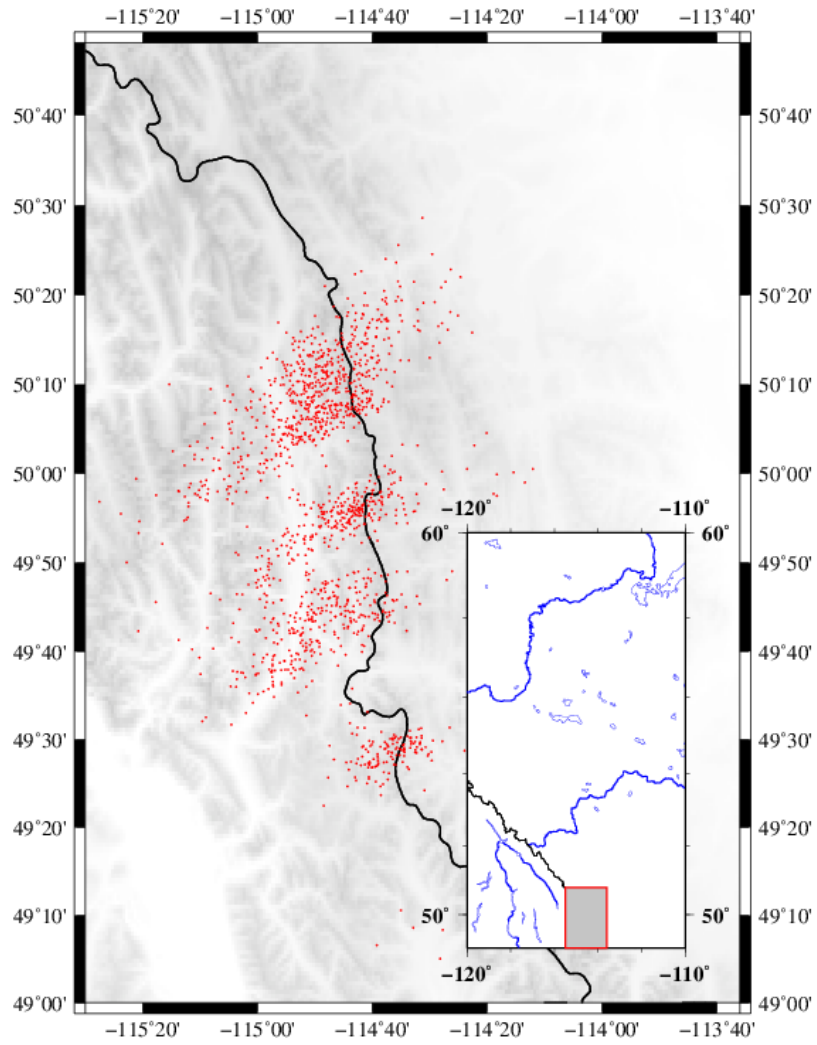


Figure 2.7: Locations of mining blasts (2006-2010) in southern Alberta before relocation using HypoDD.

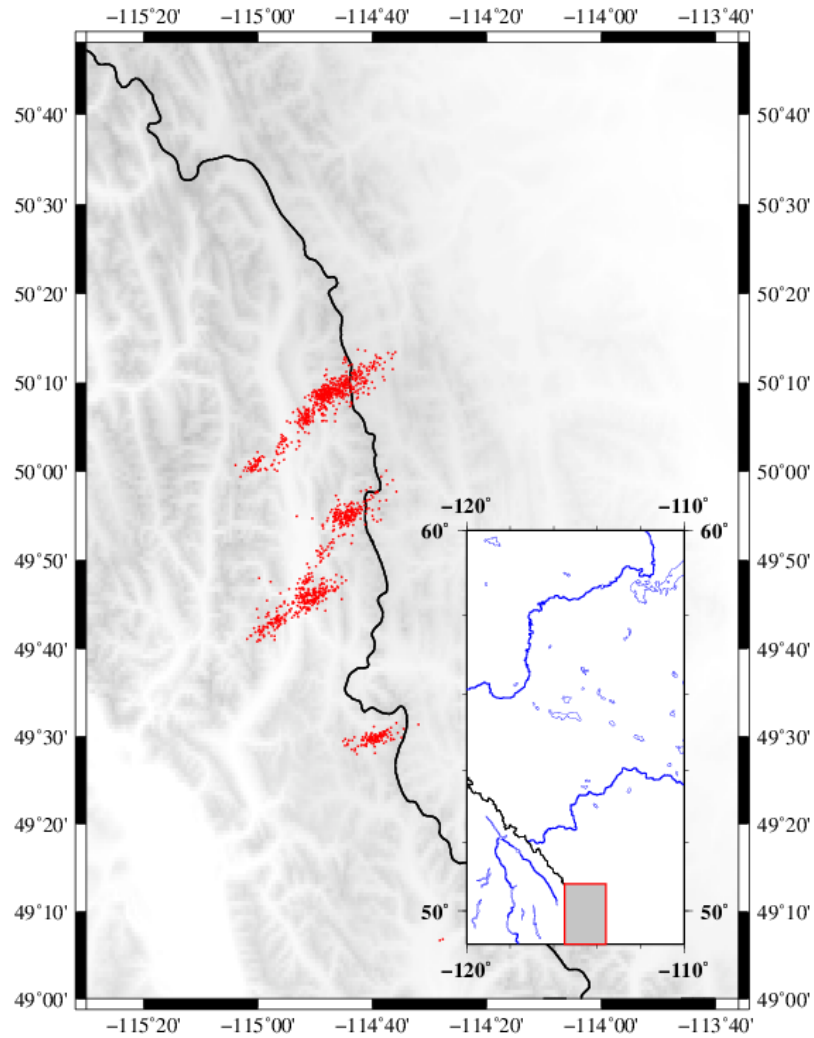


Figure 2.8: Locations of mining blasts (2006-2010) in southern Alberta after relocation using HypoDD.

2.3.2 Match and Locate (M&L)

Most of the induced events are accompanied by earthquake swarms¹² with much lower magnitude but similar waveforms, which could be recorded by the near-source stations. In addition, due to

¹² Earthquake swarms are earthquake clusters located within a relatively small region and shock period and lack a dominating main event, which is on the opposite side of typical “pre-shock” and “after-shock” sequences.

the nature of mineral exploration, mining blasts also repeat themselves at near surface and the same location. Both types of seismicity can form clusters with hundreds of multiples ($M_w < 3$) and are suitable for further analyses such as velocity variation study. The similarity between the waveforms of the multiples from the same cluster can be evaluated by the cross-correlation coefficient that ranges from zero to one (Figure 2.9). The high similarity between the swarms and the selected master event (usually the largest event reported by other agencies) also enables us to detect more multiples with the M&L method (Zhang & Wen 2015).

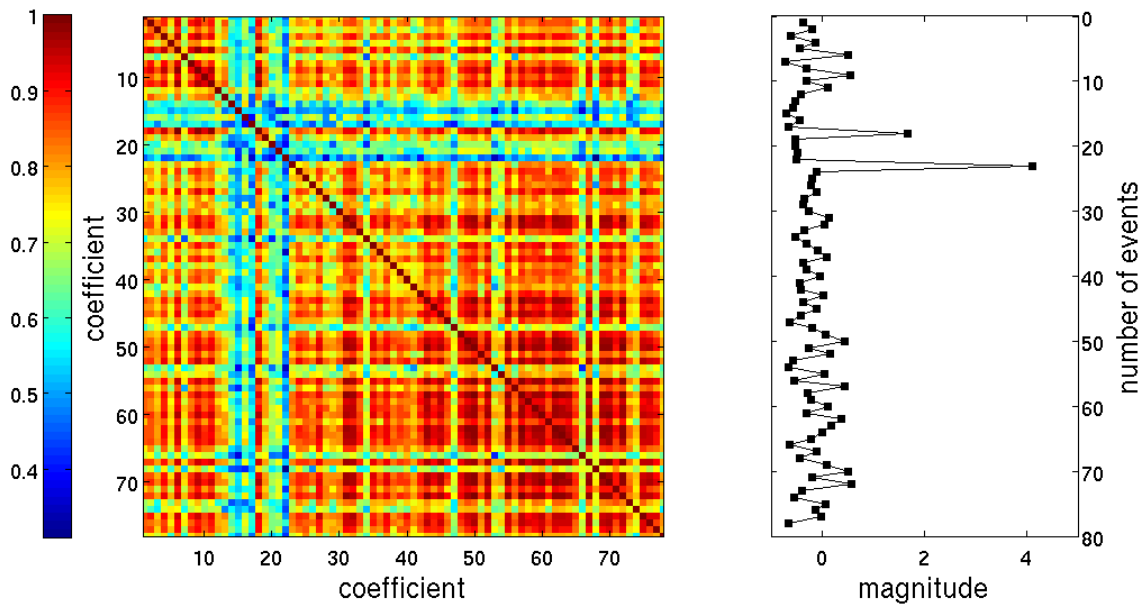


Figure 2.9: Waveform similarity plot for the multiples of the Jan 12, 2016 earthquake. Multiples are detected based on a fix location and cross-correlation (CC) larger than 0.5 from M&L (Zhang & Wen 2015). Spatial and temporal distributions of a more complete detection are discussed in chapter 4. Color bar indicates the degree of similarity ranging from 0 to 1. Magnitudes of corresponding events are shown on the right.

The availability of near-source broadband data contributed by the operator (i.e., stations WSK01-04, more details in chapter 5) enables a closer examination of the seismic activities leading to, and immediately following the January 12 event. I adopt 15 events with $M_L > 2$ (reported by Earthquakes Canada and AGS, Schultz *et al.* 2017), as master events and systematically search for

potential repeating earthquakes within 3 km of the suspected well using M&L method (Figure 2.10, Zhang & Wen 2015a). Unlike the traditional template matching method that assumes the template event and slave event are collocated or sufficiently close, the M&L method scans over potential event locations around the template, by making relative travel-time corrections based on the relative locations of the template event and the potential event before their cross-correlogram stacking (Zhang & Wen 2015a, 2015b). In my analysis, the S-wave phases with relatively large amplitude are used. The search space is divided into uniform grids with respective dimensions of 300 m and 100 m in hypocentral location and depth. Based on the matching procedure, I identify 1108 events with $M_w < 2$ using a minimum (CC) threshold value of 0.3. For a robust determination, only events with $CC > 0.5$ were kept for the analysis on spatial-temporal relationship with the HF wells. Detailed results are presented in chapter 4.

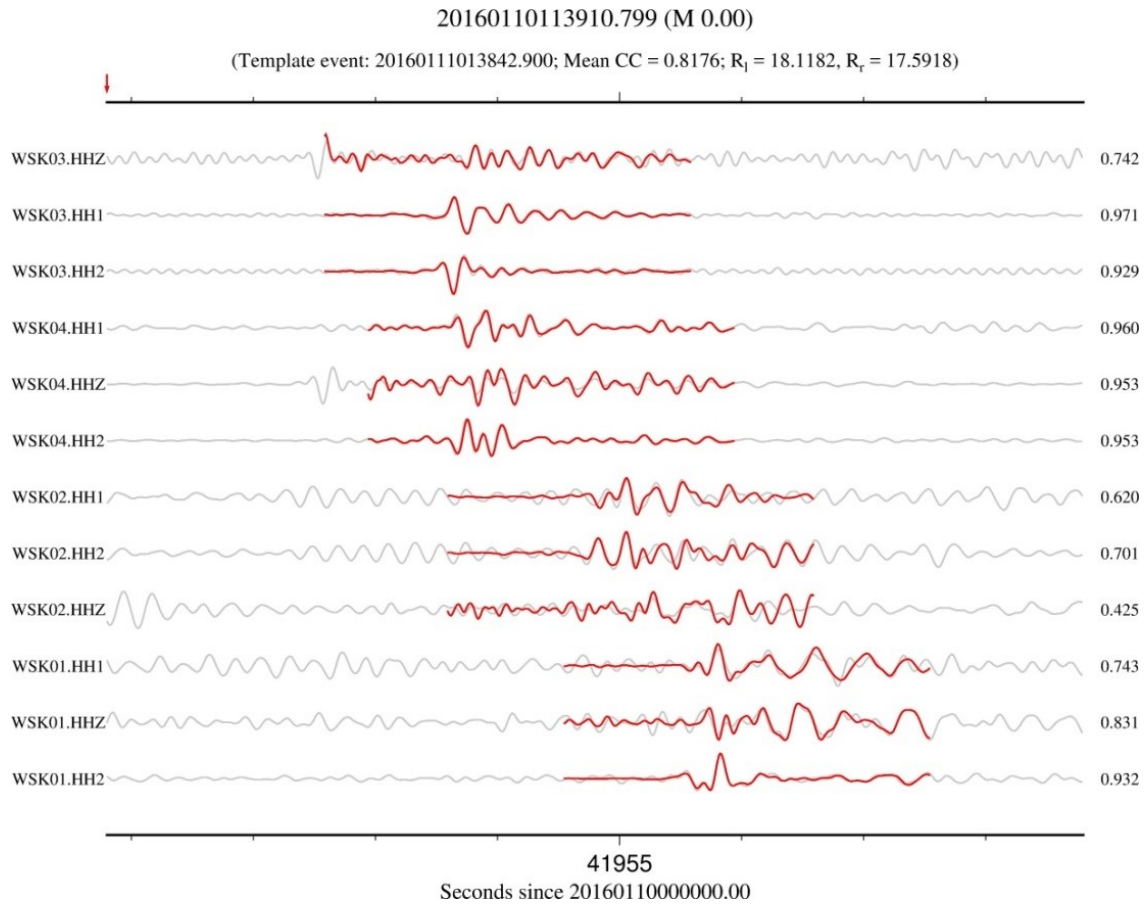


Figure 2.10: Example of a smaller event ($M_w=0$, grey waveforms) is “matched” by a template event (red waveforms) during M&L. Three components data from four industry stations (listed on the left) are used here, and the cross-correlation value is larger than 0.7. Corresponding CC value for each component is labeled on the right.

3 First “Red-light” Event

3.1 Introduction

On June 13, 2015, an earthquake with a reported magnitude (M_L) of 4.4 occurred roughly 30 km south of Fox Creek, Alberta, Canada. This was the third moderate¹³ earthquake in this historically quiescent region in less than 6 months; no $M_L > 3.5$ events have been recorded within 100 km of the hypocenter prior to 2015 (Earthquake Canada, 2018). All three events have been suspected to be associated with HF operations, which were responsible for the 2013-2014 Crooked Lake earthquake swarm 30 km west of Fox Creek (Schultz *et al.* 2015b). The June 2015 earthquake is significant for both political and scientific reasons. It was potentially the largest HF-induced earthquake in the world by 2015 and was the first earthquake that triggered the stop light for HF operations in compliance with a newly enacted “traffic light” regulation in Canada (Alberta Energy Regulator 2015).

The hypocenter of this earthquake is within the Chinchaga domain, an early Proterozoic plutonic/metamorphic terrane roughly 30 km from a splay of the Snowbird Tectonic Zone (Gu & Shen 2015; Jones 2002) near basement depth (3.8 km; Pilkington *et al.* 2000). The sedimentary strata above the basement rocks include the Duvernay formation, which originated as a fill-in basin coeval with the Leduc reef (Rokosh *et al.* 2010; Switzer *et al.* 1994). Both conventional and unconventional hydrocarbon exploration activities are presently taking place in the Duvernay play, many assisted by HF, the suspected source of recent earthquakes in this region (Bao & Eaton 2016; Atkinson *et al.* 2016).

¹³ Or light earthquake (magnitude 4-4.9) based on: <http://ds.iris.edu/ds/support/faq/52/how-do-i-interpret-magnitudes-and-magnitude-types/>

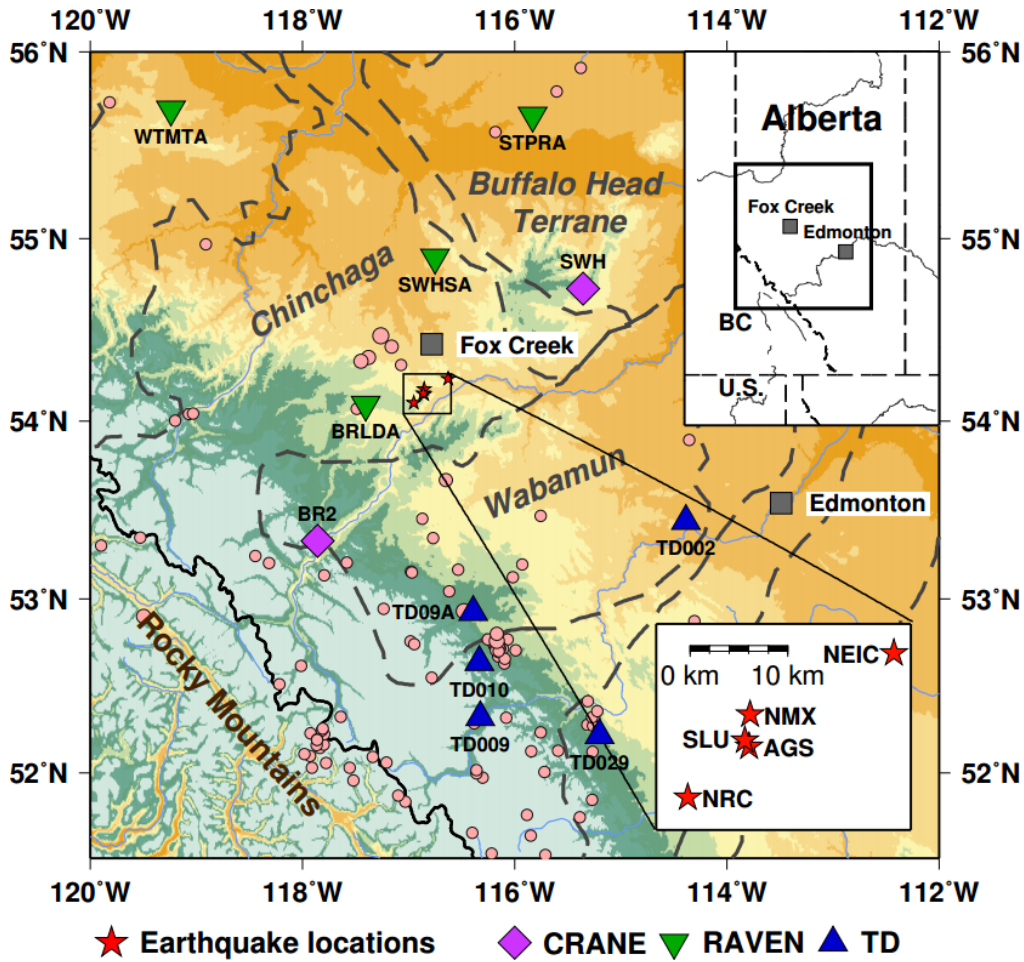


Figure 3.1: Spatial distribution of seismic stations (triangles and diamonds) and earthquakes after 2006 (circles) with magnitudes greater than 3.0. The earthquake data are obtained from the Alberta Geological Survey (2006-2010) (Stern et al. 2013) and Natural Resources Canada (2011-2015, <http://earthquakescanada.nrcan.gc.ca/recent/index-eng.php>, last accessed August 2015). The grey dashed lines denote the Proterozoic domain boundaries (Clowes et al. 2002; Ross et al. 1999). The map inset in the lower right corner highlights the hypocenter locations reported by different agencies: Natural Resources Canada (NRC), Nanometrics Athena (NMX), Saint Louis University Earthquake Center (SLU), Alberta Geological Survey (AGS), and National Earthquake Information Center (NEIC).

However, questions have surfaced in the few months after this earthquake regarding the reported magnitude, which differs by 0.6 magnitude units among five different reporting agencies (i.e., as large as $M_w=4.6$ by NRC); additionally, hypocenter locations vary by as much as 26 km (Figure 3.1). Much of the discrepancy may be attributed to: (1) limited seismic station density and/or incomplete use of available data; (2) uneven station coverage, especially along the NE-SW orientation; (3) phase picking inaccuracies associated with automatic solutions; and (4) the lack of consideration of an appropriately-calibrated attenuation model for the WCSB. Disagreements among the existing source solutions underscore the challenges in the assessment of the nature of this event, which is crucial for regional seismic monitoring, regulatory practices, and hazard mitigation (Bent 2011).

This chapter presents an updated analysis of the earthquake source parameters from full moment tensor inversions of broadband recordings and a discussion of regional ground motion observations. The availability of local data, particularly recordings from two recently installed stations, and a grid search algorithm enable us to determine the hypocenter location and depth to an accuracy of ~ 1 km. My analysis shows that this event ($M_w=3.9$) is located within the Duvernay play at a depth close to the basement and exhibits a strike-slip mechanism. The significance of these findings is discussed in relation to regional geology and HF operations in section 3.4.

3.2 Data and improvements on method

The waveforms analyzed in detail in this chapter are the broadband recordings from five TD stations, four RAVEN station (Schultz & Stern 2015), and two CRANE stations (Gu *et al.* 2011) (Figure 3.1). The stations are uniformly distributed around the source area, with distances ranging from 30 km to 300 km. Other recordings that are publicly available in real time from all networks are also used to compare ground motion amplitudes to regional attenuation models. After deconvolving the instrument responses, I rotate the three-component seismograms to the great circle and then filter the waveforms based on frequency ranges of 0.08-0.4 Hz and 0.05-0.1 Hz to enable simultaneous inversions of both body and surface wave waveforms. Various source parameters are then retrieved from full and deviatoric moment tensor inversions and verified against solutions from an independent forward modeling with the constraint of the pure DC (i.e.,

no ISO and CLVD components; e.g., Henry *et al.* 2002). Six moment tensor elements are determined through full moment tensor inversions, whereas the deviatoric solution assumes no net volume change (i.e., isotropic component = 0) (Julian *et al.* 1998) and recovers five independent tensor elements. My inversion method is based on the TDMT-INVC-ISO package (Minson & Dreger 2008; Dreger 2003) and the Green's functions are computed from frequency wave number integrations (Saikia, 1994) (see chapter 2 for details). This chapter extends the original package and enables a flexible, simultaneous inversion of multiple frequencies and phases (Chen *et al.* 2015a). Moreover, pure DC moment tensors are generated from forward modeling of a possible strike, dip and rake angles with a step size of 5° (see section 2.1.1). Independent solutions of full, deviatoric and pure DC are obtained using an assumed focal depth of 5 km, an effective average of the reported values from five different agencies (SLU, AGS, NRC, NMX, NEIC).

Two weighting schemes are explored during inversion and forward modeling based on considerations of (1) the amplitude ratio between body and surface waves and (2) the reciprocal of source-station distances. Time shifts are introduced during the fitting procedure to minimize the effects of velocity heterogeneity and earthquake mislocation (Dreger 2003). The maximum dimension m is the total number of time samples from all components (3), frequency bands (2), and stations. Both parameters are sensitive measures of solution stability during velocity model and source location perturbations. The uncertainty of the best-fit moment tensor is evaluated from a bootstrap resampling test (Efron & Tibshirani 1991). During these tests, I randomly select 14 out of 19 stations/bandwidths and determine the full moment tensor. This experiment is repeated 200 times to obtain statistically significant distributions for all elements of the moment tensor as well as the strike, slip and rake angles. The standard deviations of these distributions are effective measures of variation.

In addition, the ground motion amplitudes are determined using pseudo-acceleration (PSA) spectral amplitudes¹⁴. Distances up to 400 km are selected to show the effect of attenuation, and

¹⁴ *Work by coauthor Gail Atkinson. Included with permission.

a regional model (Yenier & Atkinson 2015; Atkinson *et al.* 2014) is used to obtain the moment magnitude and estimate the Brune-model stress drop (Brune 1970).

3.3 Results

The focal mechanisms, moment magnitude, source location, and depth are obtained as the best-fit solution from high-frequency body waves recorded by 8 stations and low-frequency surface waves recorded by 11 stations. The final inversion result indicates an epicenter close to the reported source location by AGS (for brevity, AGS location), with an optimal depth of 3-4 km and a moment magnitude of 3.9.

3.3.1 Focal mechanism and moment tensor decomposition

The solutions from waveform inversions generally achieved VRs (see Equation 10) greater than 70% regardless of whether one considers full, deviatoric, or pure DC moment tensor solutions. The fault plane solutions from these three different approaches are highly consistent, suggesting a strike-slip mechanism with candidate fault planes along E-W and N-S orientations (Figure 3.2). The components of the moment tensors and VRs are influenced by the modeling approach and data selection (Table 3.1). The result of full and deviatoric moment tensor inversions achieve identical VRs in all frequency ranges, indicating a negligible ISO component (<4%) and a limited CLVD component (see Figure 3.2). In comparison, the pure DC solutions determined through a forward routine yield lower VRs, especially at frequencies above 0.08 Hz. These VR values are comparable to those attained by SLU (<65%) based on inversions for pure DC sources. The dominance of the DC component makes RES/Pdc a reasonable metric for the assessment of hypocenter location and depth accuracies (Ichinose *et al.* 1998).

Method	Low Frequency		High Frequency		Joint	
	DC/CLVD/ISO	VR	DC/CLVD/ISO	VR	DC/CLVD/ISO	VR
DC	100/0/0	78.8	100/0/0	49.8	100/0/0	64.6
DEVIATORIC	59/41/0	90.6	82/18/0	73.5	70/30/0	77.4
FULL	62/37/1	90.6	78/18/4	73.5	70/27/3	77.4

***Table 3.1:** Moment tensor decomposition and VR for various frequency ranges and inversion or forward modeling restrictions. Note the VR values show no difference between deviatoric and full moment tensor inversion for all choice of frequency ranges, indicating the isotropic component is negligible for the studied event.*

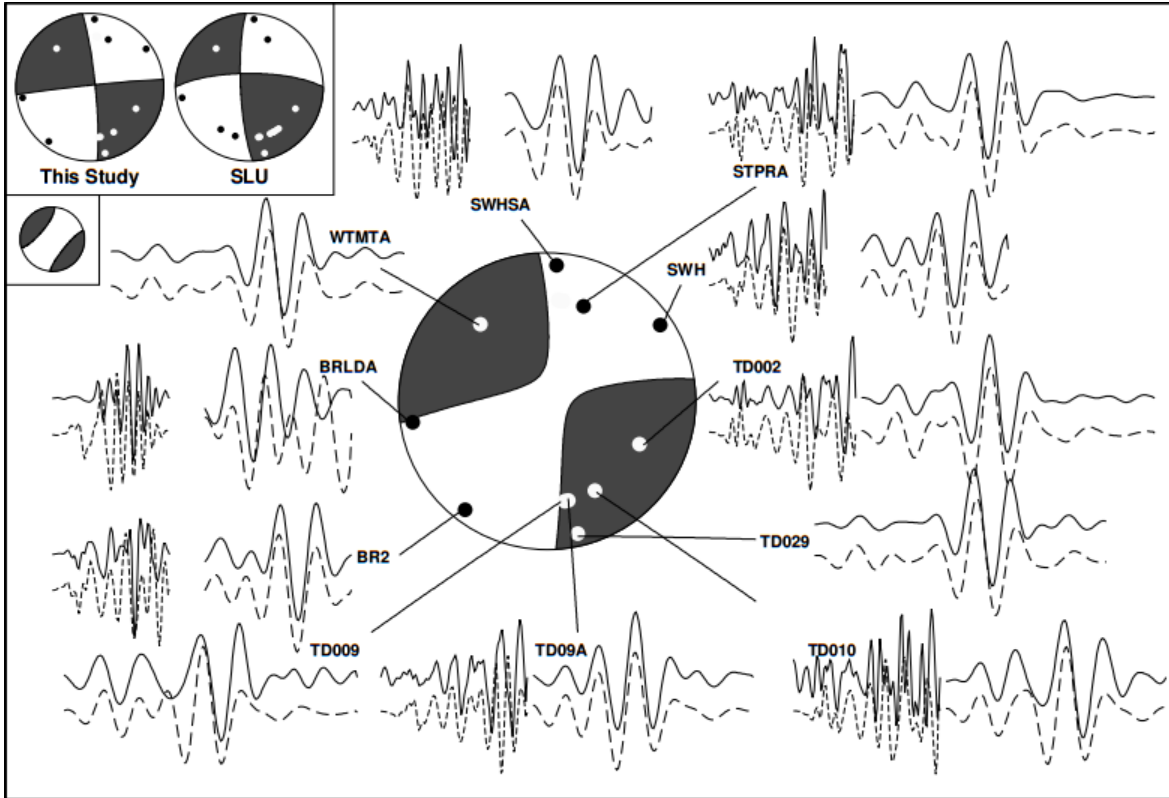


Figure 3.2: Inversion results and the vertical-component waveforms of low (0.05-0.1 Hz, 11 stations) and high (0.08-0.4 Hz, 8 stations) frequencies. The solid and dashed lines show the observed and best fitting synthetic data, respectively. The result of my full moment tensor inversion is shown in the center of the page and two DC solutions from forward modeling (left, this study) and moment tensor inversion (right, SLU, from http://www.eas.slu.edu/eqc/eqc_mt/MECH.NA/20150613235753-/index.html, last accessed Sep 2015) are shown in the upper-left corner. The latter two moment tensors used slightly different datasets and hypocenter locations (see text for details). For comparison, the non-DC component from the full moment tensor inversion is also plotted beneath the DC solutions. In all cases, the shaded quadrants are compressive. The small circles on the focal mechanisms indicate compressional (open) and dilatational (solid) P-wave first motion, determined from vertical component waveforms in the frequency range of 0.5-5.0 Hz. The takeoff angles are calculated from IASP91 (Kennett & Engdahl, 1991).

It is worth noting that inversions based on low frequencies (VR ~90%) are more stable than their high-frequency counterpart (VR ~75%). On the other hand, the inclusion of higher frequencies imposes greater constraints on the direct P and S phases with relatively high signal-to-noise ratios and reduced sensitivities to the complex shallow subsurface velocities. The joint inversion procedure (my method of choice), which incorporates both high and low frequencies, represents a reasonable compromise between VR and Pdc.

3.3.2 Improving hypocenter location and depth

The availability of near-source stations, especially recently-installed stations BR2 and SWH, enables us to provide a more accurate hypocenter location than was previously possible. To determine the best location and minimize its bias, I introduce 14 test locations within a grid of 20 km \times 20 km as the input for a series of full moment tensor inversions of both body and surface waves (Figures 3.3a and 3.3b). This grid contains four out of five reported epicenter locations, centering on the AGS/SLU location. The VR and RES/Pdc values from the solutions from all test locations of the epicenter are subsequently interpolated using 2-D splines algorithm (Smith & Wessel 1990). The highest observed VR is 69.1%, which is below the value of the final solution due to an assumed focal depth of 5 km, and the lowest RES/Pdc is ~7.4. The optimal location based on 1) a high VR and 2) RES/Pdc (see Figures 3.3a and 3.3b) is within 0.5 km of the center of test grid, coinciding with the proposed earthquake epicenter location (latitude 54.1742, longitude -116.8525) by AGS. Also notable is low RES/Pdc toward the SSW (see Figure 3b), which reflects increased Pdc (e.g., 89% at NRC location; 81% at most south location) and reduced resolution along this orientation.

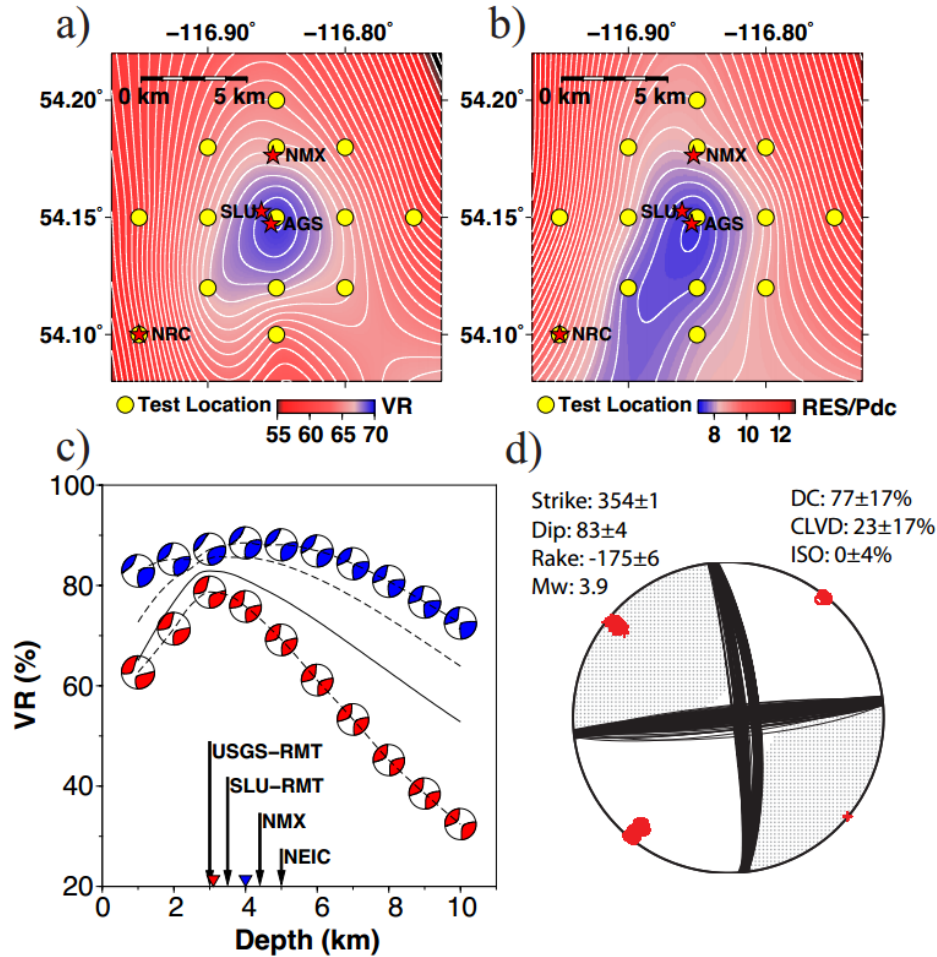


Figure 3.3: a) Interpolated VR (see Equation 10) for 14 uniformly distributed hypothetical source locations (yellow circles). The stars indicate the four reported epicenters as denoted. The maximum VR is obtained near the center of the grid. b) Interpolated RES/Pdc values (normalized residual, see Equation 11) for the same 14 source locations. The minimum RES/Pdc values roughly coincide with the AGS location, and consistently low values are observed along an N-W orientation. c) VR for a range of depths. The focal mechanism from independent inversions using body (red) and surface (blue) waves suggest optimal depths of 3 km (red triangle) and 4 km (blue triangle), respectively. The solid and dashed lines without focal mechanisms indicate the outcomes of joint inversions of surface and body waves with assumed amplitude ratios of 1 and 2. The arrows indicate the reported earthquake depths from four agencies. d) Fault plane solutions determined from a bootstrap resampling test using 200 trials (Efron & Tibshirani 1991) (see section 3.3.3 for details).

The optimal depth determined from independent inversions of low- and high- frequency ranges are 4.0 km and 3.1 km, respectively (Figure 3.3c). Both solutions exhibit relatively constant values between the depths of 2.5 and 4.5 km, beyond which the VR decreases substantially. The results of joint inversions are moderately dependent on the subjective weights (see Figure 3.3c) of the subsets of the data. An independent experiment based on inversions of the broadband (0.02-1.0 Hz) data yields a focal depth of 3.8 km (SLU), which also falls within my end-member models of 3 and 4 km.

3.3.3 Uncertainties

The reported hypocenter locations vary by as much as 26 km between the solutions of the NRC and NEIC. The variability of these solutions can be as large as 5 km (Schultz *et al.* 2015a; Farahbod *et al.* 2015) and is largely attributable to the availability /choice of stations and picking errors of the arrival times. Based on improved station coverage and a grid search algorithm (see section 3.3.2), I am able to determine the epicenter location to accuracies of ~ 1 km. Most of the distributions of the six moment tensor elements and fault angles are approximately Gaussian. Their standard deviations provide effective measures of the uncertainties for the various source parameters. The adopted velocity model (see chapter 2) produces stable source inversion results that are relatively indifferent to minor structural perturbations (Figure 3.4). The orientations of two candidate fault plane solutions and stress regimes remain stable (see Figure 3.3d). The strike, dip, and rake values determined from the means of their distributions equal to 354° , 83° , and -175° , respectively. The largest variation is observed from the rake value, which is only 6° . However, the bootstrapping test shows a standard error of 17% in CLVD based on the 95% confidence interval, which is comparable to the observed CLVD contribution (23%) to the final focal solution. Hence, I conclude that the CLVD component is poorly constrained and most likely represents only a modest contribution to the focal mechanism.

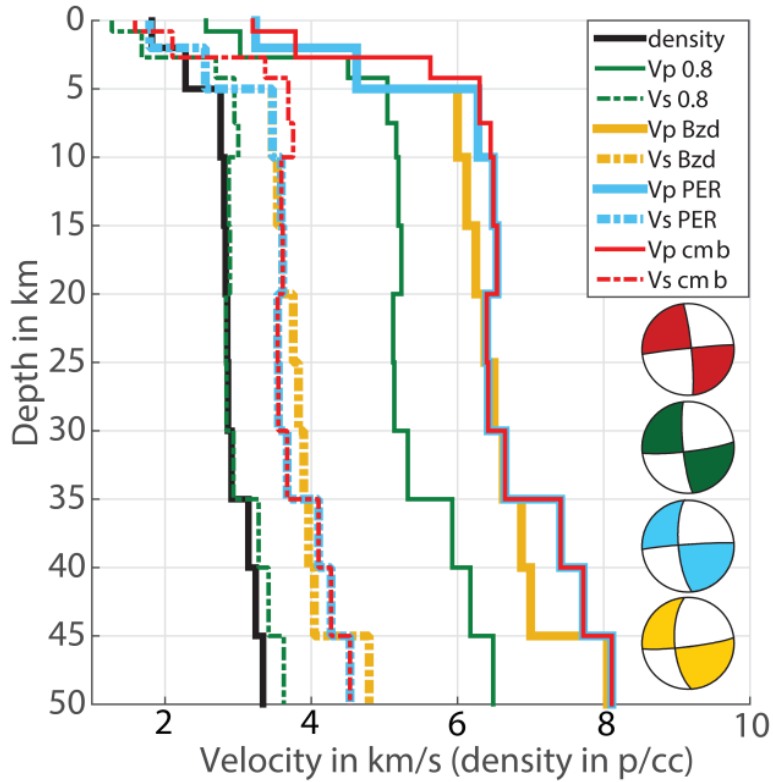


Figure 3.4: Sensitivity of inversion results to input velocity and Q structures. Input shear and compressional velocities (solid and dashed lines in color) and density (black) models for full moment tensor inversions. The four models are edited from V_s model PER of Chen et al. (2015b) (blue), V_p model from Bouzidi et al. (2002) (yellow), a combined model from Welford & Clowes (2006) and Chen et al. (2015b) (red), and the combined model with 20% velocity reduction (green). The inverted double-couple solutions are shaded using the same color conventions. In all cases, the scaling factor between V_p and V_s is based on empirical equations from Brocher (2005). All four solutions show a similar strike, dip and rake angles.

3.3.4 Analysis of ground-motion amplitudes¹⁵

Large variability also exists in reported observatory magnitude measures of local magnitude (M_L 4.6; NEIC) and Lg wave amplitude (mb_Lg 4.0; SLU) (Nuttli 1973; Herrmann & Nuttli 1982).

¹⁵ Work by coauthor Gail Atkinson. Included with permission.

For this reason, we use the vertical-component 1 Hz PSA amplitudes (with 5% damping) of publicly available stations, and a distance less than 400 km to provide an alternative estimate of moment magnitude (see the algorithm Atkinson *et al.* 2014). Using the model for central and eastern North America (CENA), which provides the best fit to the observed attenuation, we obtain a value of $M_w = 3.9$, identical to that from my moment tensor inversion (Figures 3.5 and 3.6). We further estimate the source spectrum for the event by correcting all amplitudes to the source, following the equations provided in Yenier & Atkinson (2015). After correcting for average site effects (Farrugia *et al.* 2015), we obtained a stress drop of 6 MPa by matching the high-frequency amplitudes of the median horizontal PSA amplitudes (the observed earthquake source function, see Yenier & Atkinson, 2015). The value of 6 MPa is near the upper range of the stress drops for shallow (induced) events in CENA, consistent with those determined for regional events in other studies (Atkinson *et al.* 2014; Rebollar *et al.* 1982).

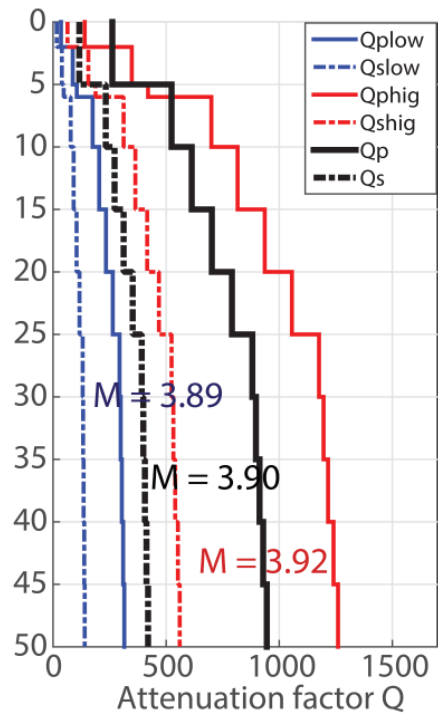


Figure 3.5: Input Q models for moment tensor inversions based on Zelt and Ellis (1990). The scaling factors are 1.3 (optimal, black), 0.5 (blue) and 2.0 (red), respectively. Changing the input Q models only changes the moment magnitude from the moment tensor inversions by 0.03.

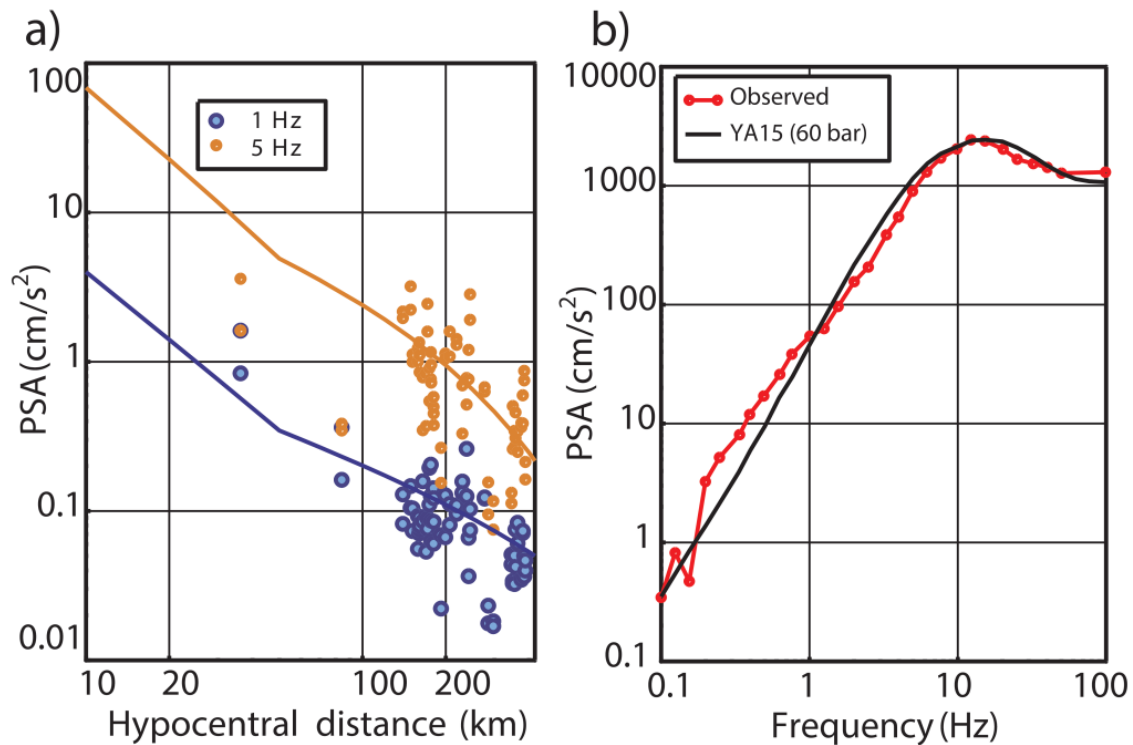


Figure 3.6: Horizontal-component response spectral amplitudes (PSA, 5%-damped pseudo-acceleration). a) PSA versus hypocentral distance at 1 Hz (blue) and 5 Hz (orange), compared to prediction equations of the simulation-based ground motion model of Yenier and Atkinson (2015) for central and eastern North America, for $M_w = 3.9$. b) Inferred PSA source spectrum, after correction for site response, in comparison to Brune-model spectrum for $M_w = 3.9$ and a stress drop of 60 bars.

3.4 Discussion

The earthquake source parameters from my moment tensor inversions offer improved constraints on the hypocenter location, faulting geometry, and the state of stress in the subsurface, which are all critical in the assessment of seismic hazard in central Alberta. The final focal mechanism solution produces an outstanding fit to the recorded three-component waveforms reaching a VR as high as 79.8% (see Figure 3.2). The inverted magnitude of this event ($M_w = 3.93$) is consistent

with the solution obtained using PSA amplitudes and an independent, pure DC moment tensor inversion ($M_w = 3.94$; SLU). This value, which falls slightly below the red-light threshold ($M_w = 4.0$) defined by the provincial traffic-light regulation (Alberta Energy Regulator, 2015), is significantly smaller than the initial report of $M_L = 4.4$.

Aside from a relatively large magnitude, this event attracted significant media attention due to its proximity to the unconventional oil and gas exploration. The earthquake is located ~27 km south of Fox Creek within the Duvernay shale gas play, an area characterized by significant HF activities (e.g., Kaybob south and Pine Creek reservoirs). Multistage fracturing is conducted (Haug *et al.* 2013) with horizontal wells drilled to depths up to 3.5 km, close to the basement (~ 4 km, Majorowicz *et al.* 2014; Pilkington *et al.* 2000; Bachu 1993). Five horizontal wells have been identified within 2 km of my proposed hypocenter location. Based on recently published reports (obtained through GeoSCOUT), HF operations took place during the month preceding the earthquake (injection data released and updated, see cluster SS10 in Figure S2 of Schultz *et al.* 2016). The publicly accessible records suggest no evidence of other major industrial activities associated with enhanced oil recovery or waste-water disposal in the vicinity during 2015. The depth of the earthquake determined from my full moment tensor inversion is 3-4 km, overlapping with the dolostone-hosted shale gas reservoirs in the depth range of 3.1-3.6 km (Rokosh *et al.* 2012) and the bottom depth of HF. In the WCSB, correlations between the focal and injection depths have been documented in the Cordel Field (Schultz *et al.* 2014), Crooked Lake (Schultz *et al.* 2015b), Cardston (Schultz *et al.* 2015c), Rocky Mountain House (Rebollar *et al.* 1982) and British Columbia (BC Oil and Gas Commission 2012, 2014) where earthquake swarms with magnitudes 1-3.5 are possibly caused by increased pore pressure near the basement. Globally, larger earthquakes triggered by fluid injection/extraction have been observed in Colorado (McGarr 2014; Ake *et al.* 2005), Ohio (Skoumal *et al.* 2015b; Friberg *et al.* 2014; Kim 2013), and Switzerland (Evans *et al.* 2012; Häring *et al.* 2008). Judging from the hypocenter location, focal depth and timing, an association of this event with nearby HF operations cannot be excluded.

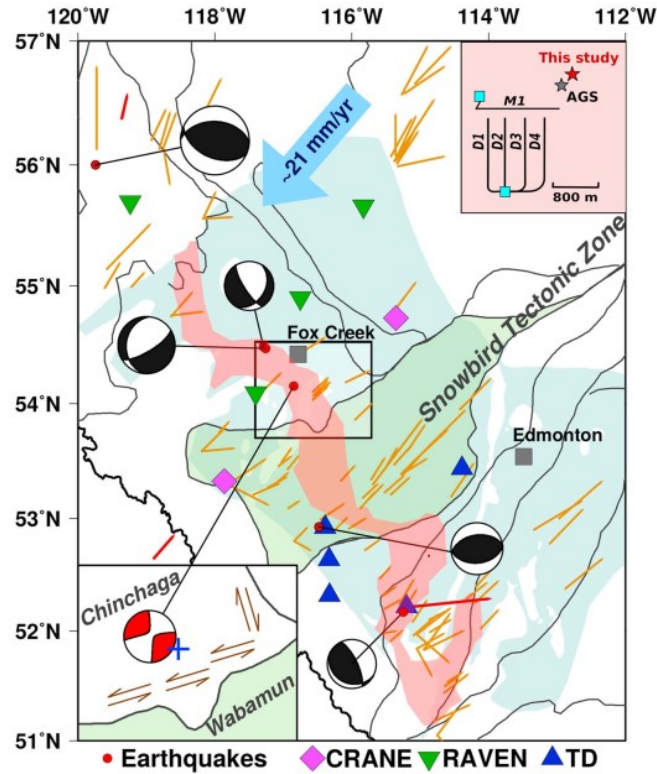


Figure 3.7: Crustal stress and available focal mechanisms of $M_w > 3.5$ earthquakes superimposed on a tectonic map of the study region. The thin solid lines denote the proposed Proterozoic domain boundaries (Ross et al. 1999). The rate and direction of the absolute present-day plate motion are indicated by the blue arrow (DeMets et al., 1990). The crustal stress from borehole breakout data are represented in yellow, and those determined from seismic source solutions are shown in red (Heidbach et al. 2010). The bottom left map inset highlights the source region, and the interpreted fault movements are indicated by the double arrows. The blue cross marks a graben (faults) in the depth range of 3.1–3.8 km, mapped by an earlier active-source seismic survey (Green & Mountjoy 2005, also see Figure 3.8). The area shaded in green denotes the Wabamun domain. The area shaded in light blue indicates the shape and location of the Duvernay Formation, and the rich-gas region is highlighted in red (obtained from Oilweek Magazine, 2013). The map inset in the top right corner shows the hypocenter locations (stars) relative to two HF wells (blue squares) that were active during June 2015. The bottom depths and the latest well completion dates are as follows: M1: 2415.0 m, June 7, 2015; D1: 3434.7 m, June 2, 2015; D2: 3433.9 m, June 5, 2015; D3: 3445.0 m, May 10, 2015; D4: 3446.1 m, May 11, 2015.

Among these induced earthquakes observed worldwide, a moderate percentage shows a strike-slip focal mechanism (Zang *et al.* 2014). Movements along buried faults, which are difficult to detect based on active-source seismic surveys, are likely responsible (Mcnamara *et al.* 2015; Zhang *et al.* 2013). My moment tensor inversions with full, deviatoric, and pure DC constraints suggest ~80% DC and a strike-slip mechanism with vertical fault planes. The stability of the fault geometry is further evidenced by the consistency between my best fit result and the solution from SLU, determined from independent crustal velocity and attenuation models (see Figure 3.2). The two candidate fault planes, which are E-W and N-S oriented, suggest an NE-SW maximum compressional axis consistent with the regional crustal stress orientations from borehole breakouts and drilling-induced fractures (Reiter *et al.* 2014; Kao *et al.* 2012) (Figure 3.7). Similar compressional axes are also obtained from other $M_w > 3.5$ earthquakes in central and western Alberta (Eaton & Mahani 2015; Kao *et al.* 2012). However, the mechanism of this earthquake (strike-slip) differs considerably from those of the aforementioned regional events (mainly normal and thrust) and favors a potential association with a pre-existing vertical fault.

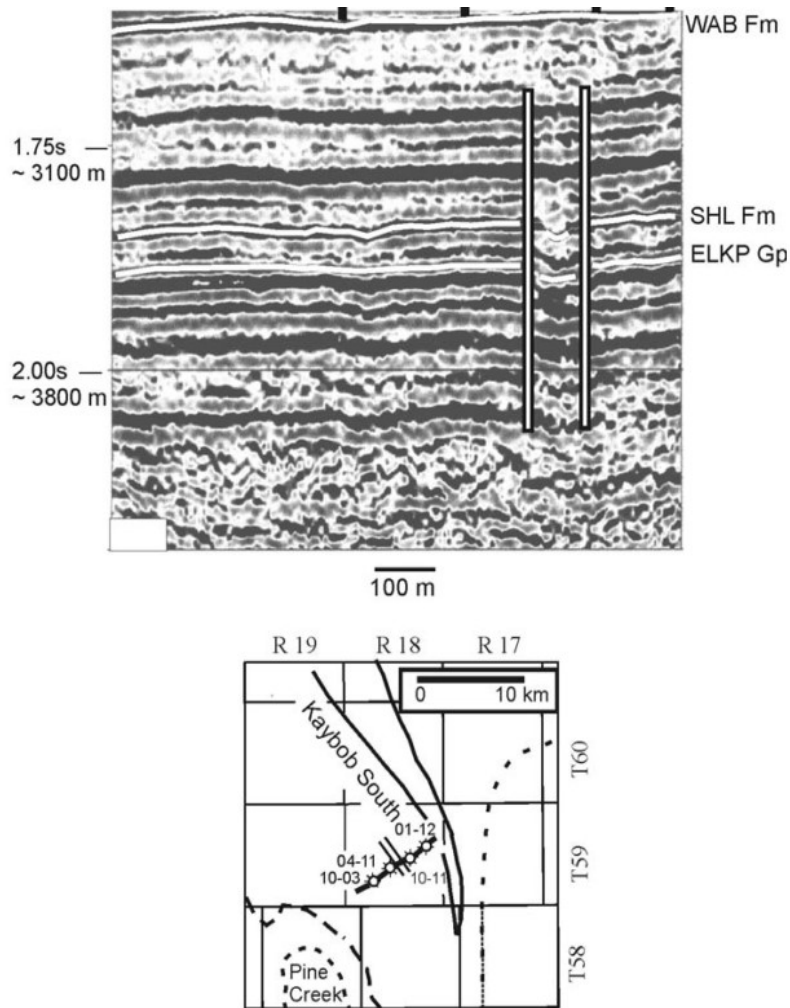


Figure 3.8: Vertical fault(s) within 10km of the hypocentral location of the June 12, 2015 earthquake mapped by a previous 3-D seismic survey. Figure from Green & Mountjoy (2005).

Based on geochemical, well-logging and reflection seismic data, Green & Mountjoy (2005) suggest that high-angle faults are present 10 km away from my proposed hypocenter location (see Figure 3.7 and 3.8). At a depth of 3.1-3.8 km, two of these faults mark the boundaries of a 100 m wide graben with a dimension of ~0.7 km. The expected maximum earthquake magnitude on a fault of such dimension is close to 4 (Zang *et al.* 2014; Wells & Coppersmith 1994), comparable to that of the June 2015 earthquake. While these faults may not be directly associated with this event, reactivation of a similar vertical fault with a common origin is a realistic possibility.

Proterozoic tectonic history of the study region is also conducive to significant crustal deformation and the existence of buried faults. In the proximity of the epicenter location, the Snowbird Tectonic Zone (STZ) was suggested as either a trans-continental suture (Berman *et al.* 2007; Ross *et al.* 2000; Hoffman 1988) or shear zone (Hanmer *et al.* 1995; Lewry *et al.* 1994) that bifurcates around the Proterozoic Wabamun domain (see Figure 3.7). The southern branch of STZ has been widely linked to subduction (Berman *et al.* 2007), while the origin of the northern branch (~30 km away from the proposed earthquake hypocenter location) remains debated. Regardless of the nature of STZ, the interaction/collision between the Proterozoic micro-continents (Wabamun and Chinchaga domains) is potentially responsible for the pre-existing faults parallel, or perpendicular, to the domain boundary.

It is worth noting that despite being mostly strike-slip, the June 2015 earthquake may contain ~20% non-DC components. The interpretation of CLVD remains controversial, mainly centering on (1) an improper assumption that multiple subevents (Kuge & Kawakatsu 1990) or fracturing along on curve/complex geometry (Kawakatsu 1991) can be represented by a single source and (2) fluid-driven opening (or closing) of tensile cracks (Miller *et al.* 1998). The second explanation is favored by shallow earthquakes, especially at depth involving fluid injection or extraction (Zhang *et al.* 2016; Frohlich 1994). The horizontal CLVD obtained (see Figure 3.2) is frequently observed in microearthquakes in connection with HF (Baig & Urbancic, 2010). Whether the same type of mechanism is responsible for earthquakes that are orders of magnitude larger, such as this case, remains questionable (see chapter 5 for recent updates and discussion on this point).

3.5 Summary

This chapter presents our solution of seismic source parameters for a moderate earthquake near Fox Creek, Alberta using time-domain full moment tensor inversions. We conclude that:

- The location of this event is 27 km south of the town of Fox Creek, and the focal depth is between 3 to 4 km, at the junction between sedimentary and basement layers.

- The magnitude of this event determined from full moment tensor inversion is $M_w 3.9$, consistent with that from PSA calculations; the observed ground motions are consistent with a stress drop of 6 MPa.
- The focal mechanism is predominately vertical strike-slip with N-S, and E-W orientated fault planes. The maximum stress direction is consistent with horizontal crustal stress orientation.
- We observed $\sim 20\%$ non-DC component, which is dominated by a horizontal CLVD with relatively large uncertainty.

A reliable correlation or dissociation between this earthquake and local shale gas exploration activities will require improved subsurface information and well-completion data. The key parameters of this event (e.g., timing, depth, and mechanism) are symptomatic of an earthquake induced by HF operations in the vicinity of Fox Creek Alberta. Overall, the broadband seismic data and the approach adopted by this chapter may benefit a future assessment of the seismic hazard in and around the WCSB.

4 Second “Red-light” Event

4.1 Introduction

Following the June 13, 2015 earthquake, a $M_w=4.1$ earthquake (known as the second “red-light” event) occurred to the west side of Fox Creek, which attracted significant media attention and raised public concern. The second “red-light” earthquake took place on January 12 2016, and is the largest earthquake in Alberta for the past decade. For simplicity, I will refer to this event as the J12EQ hereinafter. Fortunately, injection parameters from the suspected HF well and data from four industry-owned stations have been made available to the public. In this chapter, I present an integrated source analysis for the January 12, 2016 earthquake with data both from the regional seismic arrays and near-source stations contributed by the industry. Based on existing geological information and the distribution of the detected earthquake swarm, I am able to 1) determine the true fault orientation and place it in the regional geological context, and 2) establish the connection between the seismicity and the nearby HF activities. This thesis suggests that the J12EQ is representative of the majority of HF related earthquakes (i.e., eight $M_w>3$ earthquakes in late 2016) around the Crooked Lake region, and the new information on the source properties could greatly benefit future analyses of natural and induced earthquakes in the WCSB.

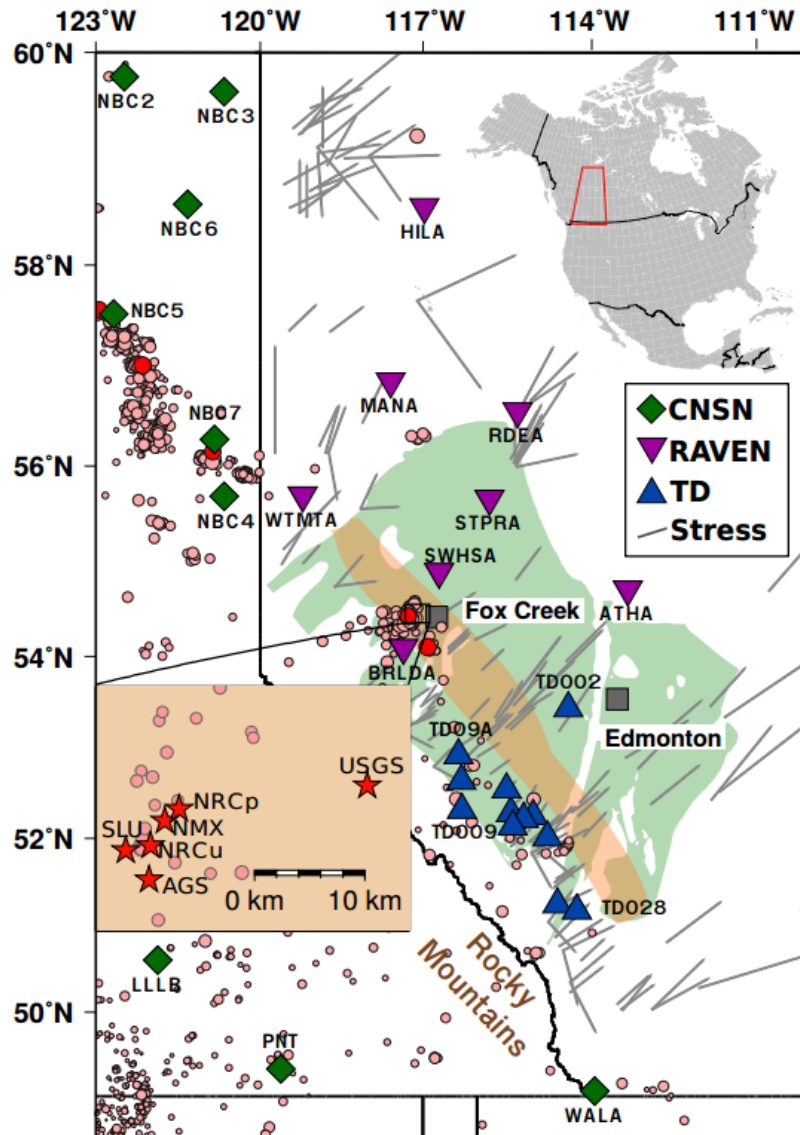


Figure 4.1: Spatial distribution of seismic monitoring stations and earthquakes (circles) since 2013; $M_w > 4$ earthquakes are shown in red. The area of occurrence of the Duvernay Formation is shaded in light green, with the wet-gas region highlighted in yellow (Rokosh et al. 2012). Crustal stress orientations obtained from borehole breakouts are shown by the grey lines. The map inset shows the epicenters of the January 12, 2016 event reported by different agencies (red stars): U. S. Geological Survey (USGS); Nanometrics Athena (NMX); Saint Louis University earthquake center (SLU); Alberta Geological Survey (AGS); Natural Resources Canada (NRC), where “p” and “u” indicate the previous and updated locations, respectively.

4.2 Study region and data

The hypocenter of the J12EQ is located approximately 30 km west of Fox Creek, Alberta (Figure 4.1). The depths reported by several agencies vary between 3–8 km (Figure 4.4c), overlapping with the depth of the Precambrian crystalline basement (3.8 km, Majorowicz *et al.* 2014; Pilkington *et al.* 2000). Early sedimentation in this area occurred in a marine environment, resulting in the Beaverhill Lake Group and Elk Point Group carbonates, shales, and evaporites underlying the Duvernay Formation (Switzer *et al.* 1994). The Duvernay Formation is a late Devonian aged (~370 Ma), organic-rich, silica-rich stratigraphic unit within the Woodbend Group at an approximate depth of 3 km (Wendte & Uyeno 2005). The thickness of the Duvernay Formation varies mainly between 25 and 60 m in a broad region covering ~56,000 km² in total area, where ~24,000 km² is within the wet-gas or volatile-oil maturity window (Davis & Karlen 2014; Dunn *et al.* 2012). Much of the mature area is overpressured with a pressure-depth ratio reaching 19kPa/m (Fox *et al.* 2015).

My dataset contains three-component recordings of the J12EQ from three regional telemetered networks: TransAlta Dam Monitoring Network (TD), Canadian National Seismograph Network (CNSN), and the Regional Alberta Seismic Observatory for Earthquake Studies Network (RAVEN) (Schultz & Stern 2015) (Figure 4.1). The distances of the selected stations from the epicenter range from 30 to 700 km, providing relatively uniform coverage except for an azimuth gap of 86° toward the NW. After the removal of instrument responses, I integrate the original velocity seismograms to displacement and rotate the source-receiver paths to the great circle. Based on the signal-to-noise ratios of the recorded waveforms, 24 out of 29 stations are retained after quality control. Finally, the swarm associated with the J12EQ is detected with the continuous waveform data from four near-source (<10 km) stations recently made public by industry operators.

4.3 Adjustment on the velocity model and method

Full moment tensor solutions are obtained from time domain inversions based on the TDMT_INV package (Dreger 2003). Improvements were made to the original package to enable the

simultaneous inversion of multiple frequencies, data channels, and phases. A low-frequency range (0.05–0.1 Hz) is chosen for surface-waves, and a slightly higher-frequency (0.08–0.4 Hz) range is used to emphasize the body-wave constraints. I vary the weights of the individual waveforms based on both source-station distance and the relative amplitude in the corresponding frequency ranges. For a detailed analysis of the effects of the model perturbations on the moment tensor solutions, which are mostly secondary, I refer the reader to chapter 2 and the Appendix.

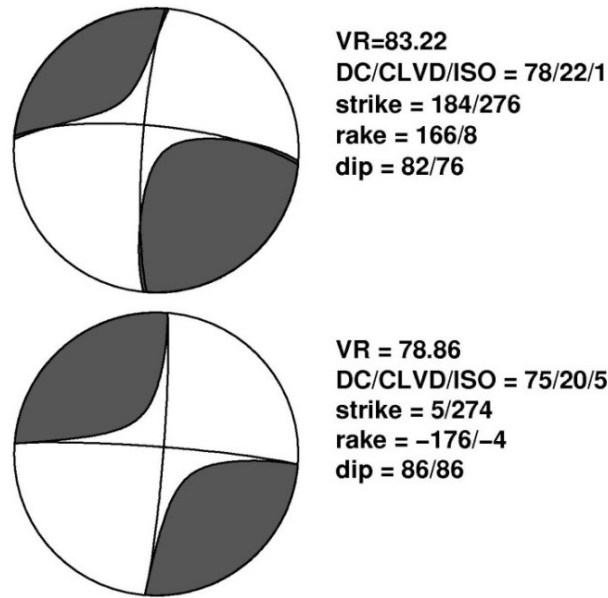


Figure 4.2: Comparison of the focal mechanism before (bottom) and after (top) the secondary shifts applied to individual components of each local station (<250 km).

The VR (see Equation 10) is also used to compare the results from different locations as well as to determine the best focal depth. While all stations from 30 to 700 km are used to resolve the full moment tensor, I only consider data recorded by regional stations within 250 km during the location and depth searches to ensure sufficient sensitivities to the hypocentral location.

Since the Green's functions are only calculated based on a one-dimensional velocity model, it is useful to introduce time shifts to the three-component waveforms of a given station to minimize the effects of (1) uncertain source location, (2) inaccurate velocity model, and (3) path heterogeneity among stations. After the waveforms are adjusted optimally (VR>70%), the

transverse, radial and vertical components for each station are shifted independently (Figures 4.2 and 4.3) to further improve the fit and minimize the potential effects of anisotropy (Vavryčuk *et al.* 2008; Frohlich 1994). The latter shifts are secondary, typically within 1s and smaller than the shortest half period (1.25 s). Effects of path uncertainty and heterogeneity have been tested in Wang *et al.* (2016) for a comparable case study and the effect of anisotropy, especially around the Duvernay Formation, has been detailed in section 3.3.3.

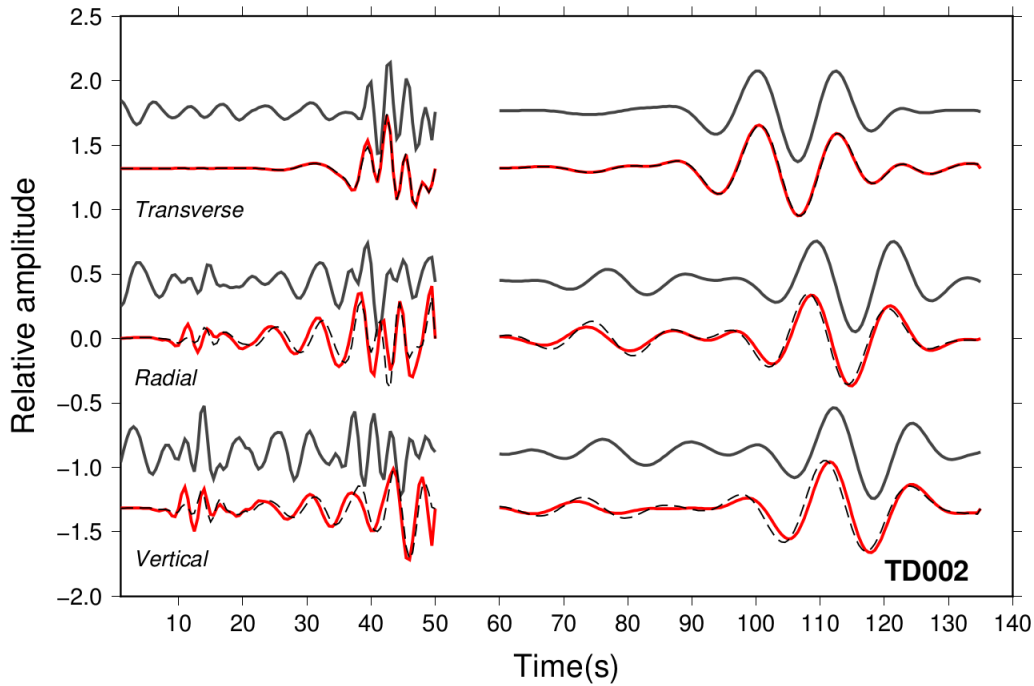


Figure 4.3: Example of waveform fitting from station TD002. The high-frequency body-wave waveforms are shown on the left, and the low-frequency surface-wave waveforms are shown on the right. The dark grey curves are the observed data, and the red/dash curves are the synthetic data after/before applying secondary shifts to correct the possible effect of anisotropy.

4.4 Results

4.4.1 Magnitude and focal mechanism solution

The moment tensor solution obtained from the J12EQ produces excellent waveform matches to the recordings from regional (30-700 km) stations (Figure 4.4a). This solution is predominately strike-slip with N-S, and E-W oriented fault planes, consistent with solutions obtained from forward simulations (inset, Figure 4.4a). This solution also resembles the focal mechanisms for other events within the Crooked Lake region (further discussed in chapter 5). It is worth mentioning that the moment magnitude is independently obtained during full moment tensor inversions and forward modeling. Both methods yield a value of $M_w 4.1$, which is consistent with the moment magnitude from SLU ($M_w 4.14$), but smaller than the other reported values ($M_w 4.4$, NRC; $M_L 4.8$, AGS; $M_L 4.9$, NMX). The decomposed moment tensors at various locations suggest a strong DC component (up to 80%), while only minor non-DC (a horizontal CLVD and <5% isotropic) may be needed to match the waveform data.

I adopt a bootstrap resampling test (Efron & Tibshirani 1991) to quantify the uncertainties in the source solution. To accomplish this, I first divide the original data into subsets based on source-station distances or azimuths, and then automatically determine the strike, slip and rake angles (Figure 4.5) from a randomly selected subset containing 70% of the data. This procedure is repeated 200 times to produce a statistically significant distribution of each parameter (Wang *et al.* 2016). The outcomes of the bootstrap resampling tests show consistent fault orientations and the standard deviation of the Gaussian-like distributions is no greater than 4° from a subset of the regional network (i.e., 11 stations <250 km).

A further validation of the focal mechanism is provided by the observed P-wave first motion (Figure 4.4a, Udías *et al.* 2014). In this analysis, I carefully determine the first motions from the vertical-component waveforms of 24 regional stations (Figure 4.1) and 4 near-source stations (see Figure 4.8) within the frequency range of 0.5–5 Hz. The take-off angles are calculated from the same velocity model presented in chapter 2. Nearly all the identified first motions are consistent with focal mechanism from moment tensor inversion (Figure 4.4a).

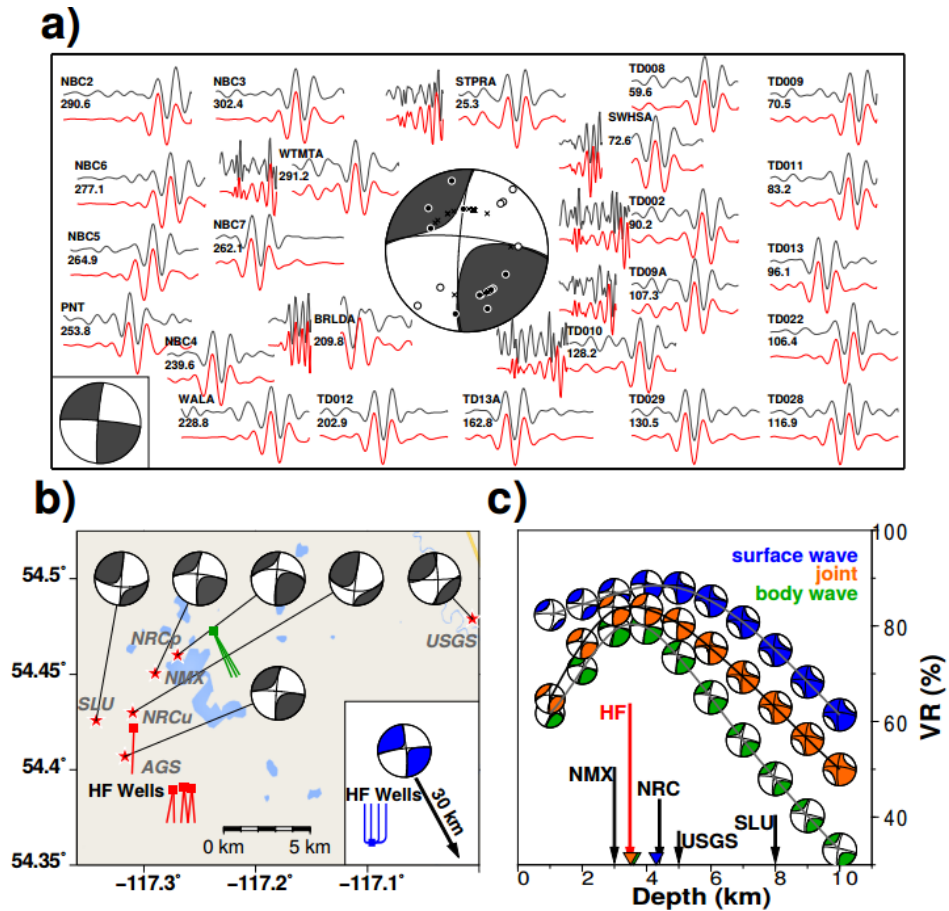


Figure 4.4: a) Moment tensor solution, observed (grey) and best-fit synthetic (red) vertical-component waveforms. Station names and the corresponding azimuths are labeled near the observed waveforms. High-frequency body waves are also used and displayed for stations within 250 km (to the left of the low-frequency waveforms). The circles on the focal mechanism indicate compressional (filled black) and dilatational (filled white) P-wave first motions picked from vertical-component waveforms (including industry contributed stations). The crosses indicate unknown first motions due to low signal-to-noise ratios in P arrivals. The focal mechanism from pure-DC modeling is shown in the lower left corner. b) Inversion results for different epicenters and the possible responsible HF wells with drilling completed in early (green) and late (red) 2015. The focal mechanism for the June 13, 2015 earthquake is presented in the lower right corner with the corresponding HF wells (blue). c) Depth search using different input data. The black arrows indicate the available focal depths reported by different agencies and the red arrow indicates the injection depth of HF operations in the source area.

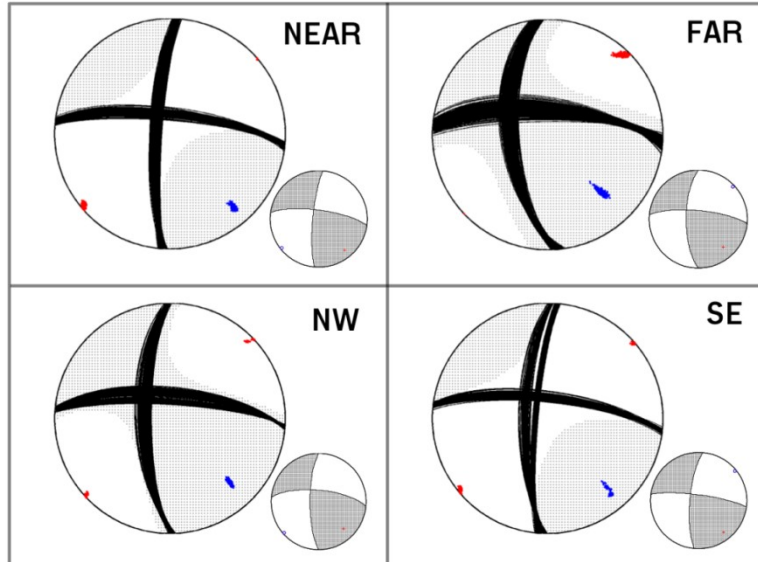


Figure 4.5: Bootstrap resampling tests of the inversion stability using the following four subsets of the recordings: near source stations (30×250 km); far source stations (250×700 km); azimuth between -125° to 45° (NW); azimuth between 45° to 235° (SE). Seventy percent of the stations from each group are used during bootstrapping, and the black lines show the corresponding fault planes from 200 trials. Corresponding result from the forward simulation are also shown. The red and blue dots mark the corresponding P- and T- axes from each solution.

This source solution is stable within minor perturbations in sediment and bedrock velocities (Wang *et al.* 2016). One further consideration is the effect of seismic anisotropy, which is known to exist in the sedimentary layers and may introduce errors in the forward modeling and inversions when stations from wide-azimuths and far offsets are used (Vavryčuk *et al.* 2008). It has been suggested that the crustal anisotropy is mostly aligned along a SW-NE orientation in the WCSB (Fouch & Rondenay 2006; Saruwatari *et al.* 2001). The amount of anisotropy for the Duvernay shale ranges between 25% to 35% for both P and S waves at a confining pressure of 90 MPa, as was determined from core samples (Ong *et al.* 2016). Therefore, the overall effect of anisotropy within the thin shale layer (25-60 m) is minor (~5%, Saruwatari *et al.* 2001) in view of the scale length of the source-receiver paths (30-700 km). This is corroborated by the consistent resulting source mechanisms with (Figure 4.4) and without the secondary time shifts detailed in section 4.3 (see Figure 4.2 and 4.3). The VR increased by 5%, but the fault angles changed by less than 12° after the secondary shifts are applied to minimize the effect of seismic anisotropy.

4.4.2 Hypocenter location of the J12EQ

The VR values from the moment tensor inversion also provide an effective means to refine the location of this earthquake. Six hypocentral locations from five different agencies have been reported for the J12EQ near Fox Creek (Figure 4.1). Most of the locations vary within 5 km except the epicenter reported by USGS, which is roughly 15 km east from the averaged center of the other reported locations. The considerable scatter of the reported locations may be attributable to the use of different regional crustal models and stations/networks. To improve the accuracy of the source location, I perform full moment tensor inversions using the same local stations (<250 km) for all possible epicenters with a fixed depth of 4 km (Figure 4.4b). Minor variations in fault plane angles (i.e., strike, slip and dip) are obtained from the output parameters based on different input locations. I further observe large variations in the percentage of non-DC component: for example, the USGS source location renders high CLVD components (66%), which contrasts with the DC-dominated focal mechanisms inverted from other starting locations. My preferred epicenter is selected based on a comparison of VR values (Table 4.1). As a result, the hypocentral location reported by NRCu achieved the highest initial VR of 82.11%, though the optimal solution converges on the location reported by NMX (VR = 85.03%, Figure 4.4a) after additional

adjustments (e.g., time shifts, see chapter 2 and Figure 4.3); this location is 3-6 km from seven potentially associated HF wells (see Figure 4.4b). The final focal depth is determined through a grid search from 1 to 10 km (Figure 4.4c) at the NMX reported epicentral location. Through independent depth-search analyses on the body waves, surface waves and the combination of the two, I determine the optimal hypocentral depth range to be 3.5-4.3 km (see Figure 4.4c). The hypocentral location and depth are further refined using four operator-contributed stations within 10 km of the HF wells during the detection of multiples (see section 4.4.3).

Location	VR (No Corrected)	(No Decomposition DC/CLVD/ISO	VR (Corrected)	Decomposition DC/CLVD/ISO
USGS	10.22	34/66/0	-	-
NMX	78.86	75/20/5	85.03	78/21/1
NRCp	73.95	87/10/3	84.53	67/31/2
NRCu	82.11	58/41/1	84.73	72/27/1
AGS	78.46	80/19/1	83.26	74/25/1
SLU	81.55	68/29/3	83.68	76/22/2

Table 4.1: Comparison of inversion results at various hypocenter locations VR (see Equation 10) values and moment tensor decompositions for different hypocenter locations before and after the correction for individual components. The preferred solution is shown in red. The names and locations of the agencies are indicated in Figure 4.1.

4.4.3 Detection and location of the earthquake swarm

The availability of injection parameters (Figure 4.6) and near-source broadband data contributed by the operator (stations WSK01-04, Figure 4.8) enables a closer examination of the seismicity leading to, and immediately following, the J12EQ. I adopt 15 events with $M_L > 2$ (reported by Earthquakes Canada and AGS, Schultz *et al.* 2017), including the J12EQ, as master events and systematically search for potential repeating earthquakes within 3 km of the suspected well using the M&L (Zhang & Wen 2015a). Unlike the traditional template matching method which assumes that the template event and slave event are collocated or sufficiently close, M&L scans over potential event locations around the template, by making relative travel-time corrections based on the relative locations of the template event and the potential event before their cross-correlogram stacking (Zhang & Wen 2015a, 2015b). In my analysis, the S-wave phases with relatively large amplitudes are used. The search space is divided into uniform grids with respective dimensions of 300 m and 100 m in hypocentral location and depth. It should be noted that due to the short duration of the accessible data, events after January 19, 2016 are not detected.

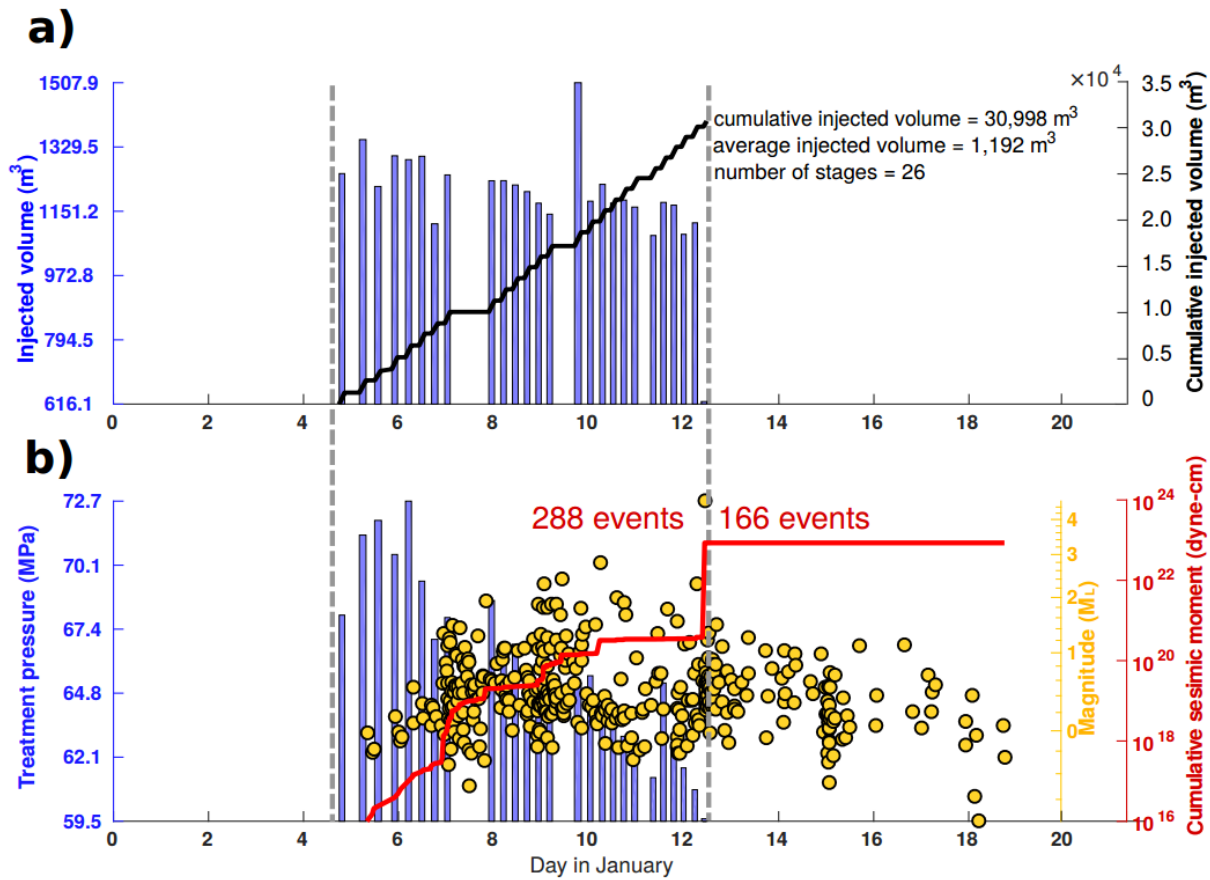


Figure 4.6: (a) Injection at the HF well (well ID: 100/15-25-062-23W5/00). Each bar represents a single HF stage, and the cumulative volume is shown by the solid black line. (b) Similar to (a) but for treatment pressure at each stage. Superimposed on the plot are the detected multiples (yellow circles) with $CC > 0.5$ and the cumulative seismic moment (red line). The grey dash line in both plots marks the period of HF stimulation (January 4 to 12, 2016). The largest event occurred during the last stage of stimulation, followed by a decrease in seismicity rate.

My analysis results in 1108 detected events with waveform cross-correlation coefficients (CC) larger than 0.3 and a b value close to 1 (Figure 4.7), a detection criterion chosen empirically based on the eye-checking of relatively large event detections to avoid possible false detection. Among the robustly detected events (CC>0.5, 454), not a single event was detected before stimulation (Figure 4.6b). The HF injection started on January 4 and ended at 11:34am (Mountain Time Zone) on January 12, 2016. The majority (63.44%) of the detected events were concurrent with the 26 stages of hydraulic fracturing, during which the cumulative seismic moment and cumulative injected volume closely tracked one another. Both the number of events and the daily maximum magnitude decreased during the post-completion period, and the last stage of the injection is marked by the occurrence of the J12EQ (7min before the end of the 26th stage).

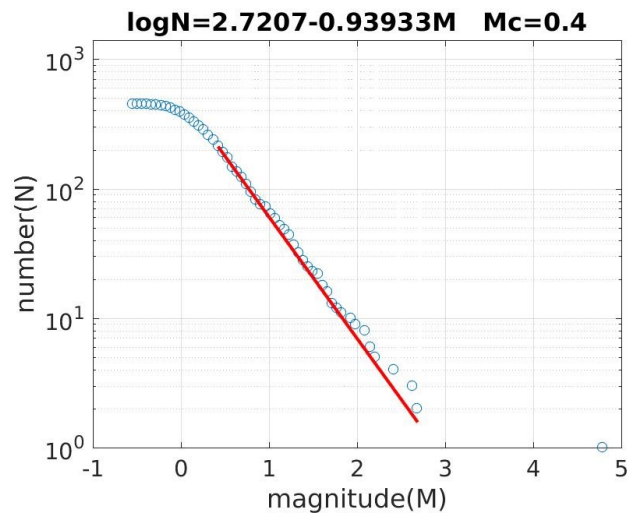


Figure 4.7: Frequency-magnitude distribution of the detected swarm (the Gutenberg-Richter law) containing 1108 events (CC>0.3) with a magnitude of completeness $M_c \sim 0.4$ (in M_L).

To assess the likelihood of a temporal association between the rate of earthquakes and the injected volume, we conduct a cross-correlation reshuffling test (Telesca 2010, Schultz & Telesca 2018). The result of this test suggests a statistical confidence greater than 99.99%¹⁶ that the newly detected events from M&L are correlated to the completion of the southern well in this three-well pad (see Figure 4.8). The temporal (and spatial) correlation between seismicity and injection activities is critical in assessing the cause of the January 2016 earthquake swarm.

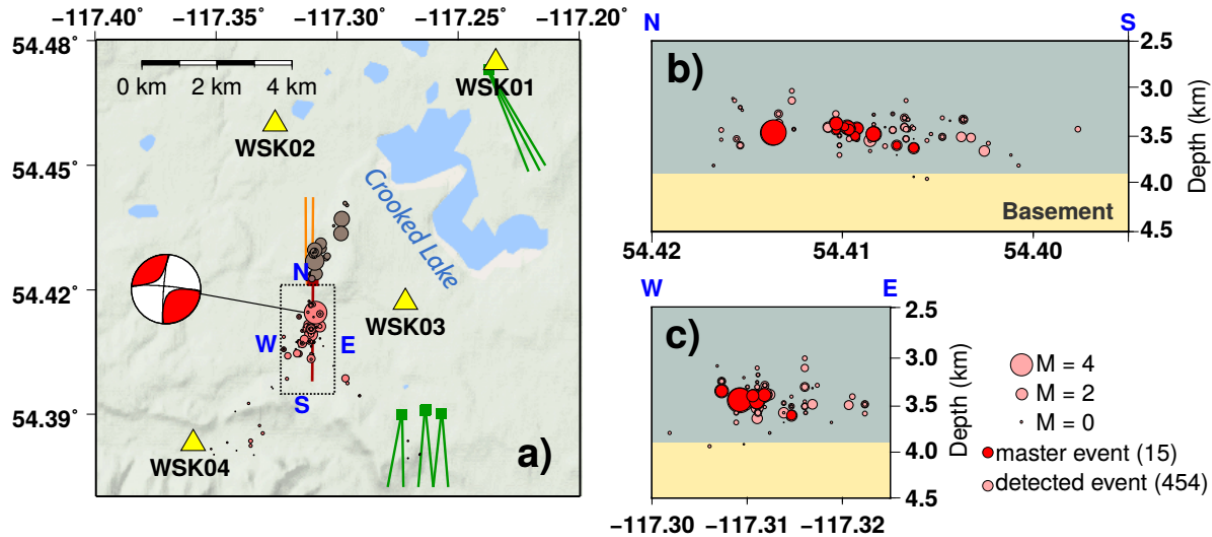


Figure 4.8: (a) Locations of the January swarm (red, $CC > 0.5$) detected using data from 4 industry-contributed stations (yellow triangles). The HF well associated with the January 2016 earthquake swarm is shown by the red line and nearby the wells associated with an earlier swarm (brown, January 2015) are shown in orange (Bao & Eaton 2016, Schultz et al. 2017). Other active wells in 2015 and 2016 are shown in green. (b) and (c) Cross-sectional views of the detected events for the swarm within the dashed box shown in a). Some events are overlapped due to the limited size of the search grid.

¹⁶ *Work by coauthor Ryan Schultz. Included with permission.

4.5 Discussion

Utilizing regional 3-component seismic data, I obtain a moment magnitude $M_w 4.1$ for the J12EQ near Crooked Lake, which is consistent with the reported value from SLU ($M_w = 4.14$) but significantly lower than the reported $M_L 4.8$ (AGS). Using moment tensor inversion, I determine the moment magnitudes of a number of HF-induced (or potentially induced) earthquakes in this region, including $M_w \sim 3.5$ in late 2013 and 2014, $M_w 3.6 \sim 4.1$ in 2015-2017. Despite the differences in magnitude scales reported by various agencies, the self-consistent comparison from the moment tensor inversion confirms that the J12EQ ranks as the second largest in Alberta in the past 30 years, surpassed only by a suspected natural $M_w 5.2$ earthquake near Dawson Creek in 2001 (Earthquakes Canada; Ristau *et al.* 2007). To date, the J12EQ is also known to be the second largest HF induced earthquake in Canada, following the $M_w 4.6$ earthquake in August 2015 in the northeastern British Columbia (Mahani *et al.* 2017). The updated injection volume ($30,998 \text{ m}^3$) falls within the uncertainties provided by Figure 4 of Atkinson *et al.* (2016). It is considerably larger than their estimated value ($\sim 10,000 \text{ m}^3$, Atkinson *et al.* 2016) and leads to a predicted magnitude ($M_w 4.0$, assuming a shear modulus of 40GPa) that follows the linear relationship proposed by McGarr (2014).

Aside from magnitude, the source analysis of the J12EQ provides critical new information on the faulting and the state of crustal stress beneath the Fox Creek/Crooked Lake region. First, the preferred location of this earthquake is SW of Crooked Lake (see Figure 4.4), within one of the most active and highly publicized seismogenic zones in connection with HF operations. The shallowest depth of the January 2016 swarm overlaps with the HF injection depth at $\sim 3.5 \text{ km}$, which is further supported by the resolved depth from double-difference relocation analysis (Schultz *et al.* 2017). The deepest estimated depth of the hypocenter could be as deep as 4.3 km, potentially extending into the basement (3.8 km, Majorowicz *et al.* 2014; Pilkington *et al.* 2000).

My focal mechanism analysis of the J12EQ suggests candidate fault planes in the N-S and E-W orientations (see Figure 4.4b), similar to the January 2015 events (Bao & Eaton 2016) and the first red-light event in June 2015 (Schultz *et al.* 2017; Wang *et al.* 2016; also see chapter 3). The P-axes from all $M_w > 3$ events near Fox Creek (Figure 4.9) are roughly parallel to the maximum

compressive horizontal stress orientations (Figure 4.1). Based on the possible rupture depth and orientations from the dominant strike-slip mechanism, I propose a model of the fault system for the January 2016 swarm as well as other earthquakes near Crooked Lake in recent years (see Figure 4.9). The suggested fault orientations are consistent with earlier findings from aeromagnetic data near Fox Creek, which provide compelling evidence for the Pine Creek fault zone with right-lateral strike-slip motion (Berger & Davies 1999). According to Berger & Davies (1999) and Berger & Zaitlin (2011), these fault systems originated as N–S strike-slips in the basement and extend vertically into the sedimentary strata, showing a flower structure. Furthermore, the presence of basement faults in this region has been argued to have influenced the contour of some reef margins, which coincide with the spatial distribution of induced seismicity (Schultz *et al.* 2016).

Moment tensor analysis offers more constraints on the characteristics of the subsurface fault system (e.g., Skoumal *et al.* 2015b). For a $M_w \sim 4$ earthquake that is ascribed to a simple linear fault plane model, the size of the vertical fault area could be as small as 1 km^2 (Schultz *et al.* 2017). In contrast, the horizontal offsets of the deep-seated vertical faults could be as large as 2–3 km (Berger & Davies 1999), resulting in much larger fault areas capable of producing moderate-sized earthquakes ($M_w 3.8\text{--}5.8$, Wells & Coppersmith 1994; Hanks & Kanamori, 1979). For example, a ~ 15 km long, N–S-trending fault has been reported near the Simonette region (~ 10 km east of Crooked Lake) based on seismic reflection data (Cortis *et al.* 1997), as well as a graben at the depth of 3.1–3.8 km within the sedimentary layers (Wang *et al.* 2016; Green & Mountjoy 2005). In view of the proximity of these faults to the location of the J12EQ, it is plausible that the wrench faults within the Pine Creek fault zone share similar origins and geometries. These faults served as effective conduits for fluid flow that facilitated the formation of dolomite-hosted gas reservoirs (Davies & Smith 2006; Duggan *et al.* 2001; Mountjoy *et al.* 1999). Considering the uncertainties (cumulatively up to hundreds of meters) of the hypocentral depth and the size of the fault plane, it is difficult to determine whether the $M_w \sim 4$ earthquakes occurred on faults within the basement or the overlying sedimentary strata. Whereas the distribution of the seismic swarm prefers a focal depth above the basement, shallower than the water-water disposal induced events (e.g., in Oklahoma). The triggering process could be linked to fluid migration along the shallower fractures and the reactivation of faults in/above the crystalline basement. This mechanism was earlier

suggested for earthquakes induced by wastewater disposal in North America (Rubinstein *et al.* 2014; Ellsworth 2013).

The 2016 Crooked Lake earthquake swarm detected from the 4 near-source industry stations offers further insight into the fault location and orientation of the J12EQ. This swarm resides within 1 km south of the reported induced seismic cluster from 2015 (Bao & Eaton 2016, see Figure 4.8). Most of the detected events (1065 out of 1108) are distributed parallel to a single HF well (dash box in Figure 4.8) with an N-S trend and are spatially separated from other wells in this region (see Figure 4.4). There is no apparent time-dependent spatial pattern during or after injection; for instance, the center of the earthquakes during the post-completion phase (after January 12) is only ~100 m away from the events during the HF stimulation, which is smaller than the size of my search grid. The best-fit strike orientation for the seismic swarm (see Figure 4.5) is 202.64°, comparable to one of my fault plane orientations (184°) resolved from focal mechanism analysis. This trend is consistent with the double-difference relocation outcomes from Schultz *et al.* 2017, in which 92 small magnitude events were detected and relocated. Furthermore, both analyses located the earthquake swarm above the basement (depth = 3.8 km), leaving only a limited number of events within the top 1 km of the basement. Based on all the evidence above, I conclude that the January 2016 earthquake sequence is induced by the nearby horizontal well completion and the true fault orientation is N-S.

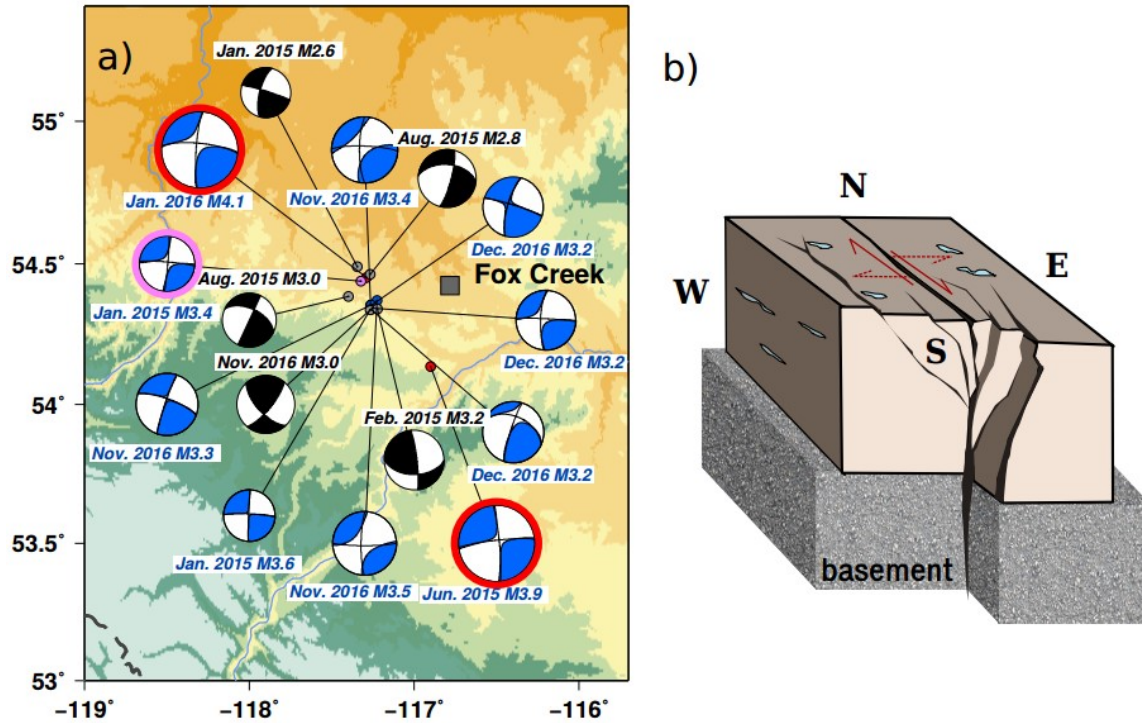


Figure 4.9: (a) A summary of the resolved focal mechanism and moment magnitude of the moderate earthquakes around Fox Creek. The event triggered the “traffic-light” protocol is highlighted by pink, and the two red-light cases are highlighted by red. When the data quality is insufficient for full moment tensor inversion (blue), focal mechanisms are resolved from DC forward modeling (black). The latter one may have larger uncertainty in fault plane orientations. Note there are eight $M_L > 3$ events took place during November and December 2016, out of which seven were resolved with focal mechanism solutions, as presented. (b) A model showing vertical fault(s) and the flower structure along the north-south orientation as suggested by Berger & Davies (1999). The directions of motion on the suggested fault (red solid arrows) and auxiliary (red dash arrows) planes from event investigated in this chapter are as indicated.

The best moment tensor solution is dominated by DC component (~75%), irrespective of the choice of the starting epicenter during the inversion (see Figure 4.4b). My moment tensor solution shows limited dependence on the crustal velocity and attenuation model (Wang *et al.* 2016), as well as on station distribution (Figure 4.3). The resolved moment tensor and the corresponding fault orientations are consistent with the solution of pure-DC moment tensor inversion from SLU and my DC forward models, comparable to those of some other HF induced earthquake in the U.S. (e.g., Skoumal *et al.* 2015; McNamara *et al.* 2015). The focal mechanism, as well as its decomposition, is also highly consistent with that of the June 13, 2015 earthquake (see Figure 4.4b and Figure 3.2). Furthermore, the strike-slip dominated mechanism with the limited non-DC component is also resolved from several $M_w > 3$ earthquakes between 2015 and 2017 within the Fox Creek/Crooked Lake region (see Figure 4.9a). The similarity in focal depths, moment tensors, and their decomposition results suggest comparable triggering mechanisms for events associated with HF operations in this general area (see Figure 4.4b). Based on the moment tensor solutions of several events in western Canada, Zhang *et al.* (2016) suggests that (1) shallower depths and (2) larger non-DC components are expected from induced earthquakes than natural earthquakes. My analysis of the January 2016 earthquake swarm suggests relatively shallow source depths, consistent with their first metric. However, the modest non-DC component based on improved crustal model and revised source location do not systematically differ from those of natural earthquakes (Zhang *et al.* 2016; Cesca & Dahm 2013). A similar limited amount of non-DC component is also observed from HF induced events in the northern British Columbia (Mahani *et al.* 2017). Likely, resolving non-DC components with fidelity will require more data and precise structure model (i.e., 3D), as my experiments do suggest that hypocentral biases, anisotropy and/or insufficient station coverage preferentially contribute to errors in the non-DC components (e.g., Wang *et al.* 2016; Šílený *et al.* 2009; Vavryčuk *et al.* 2008; Frohlich 1994).

4.6 Summary

The main purpose of this chapter is to present the source analysis of a HF induced seismic swarm during January 2016, especially the $M_w 4.1$ earthquake, which is one of the largest earthquakes induced by HF operations worldwide. I verify this event to be the largest earthquake in the past

decade in Alberta through moment tensor inversion. I find this earthquake to be dominated by the DC component, while source solutions are relatively independent of the initial hypocentral location. Furthermore, recent (2015-2017) moderate earthquakes are resolved with the similar strike-slip mechanism in the Crooked Lake region. With more than a thousand events detected around this earthquake, its significance is highlighted by the close spatial-temporal relationship to a HF well targeting the Duvernay Formation. The majority of the swarm took place during HF stimulation, and the largest event occurred during the last stage of injection. The depth of the detected and located earthquake swarm is near the top of the crystalline basement and suggests the reactivation of an N-S-trending fault which may be analogous to the Pine Creek fault zone.

5 Faults and Non-double-couple Components

5.1 Introduction

In recent years, increases of seismicity rates induced (or ‘triggered’) by industrial activities (e.g., McGarr *et al.* 2015) have invited both critical scientific inquiries and public scrutiny due to their potential impact on seismic hazard assessment (Schultz *et al.* 2018; Mignan *et al.* 2017; Peterson *et al.* 2017). Induced earthquakes large enough to be felt have been widely reported in the United States (Ellsworth, 2013), Canada (Bao & Eaton, 2016), Germany (Evans *et al.* 2012), South Korea (Kim *et al.* 2018; Grigoli *et al.* 2018) and other countries (see Grigoli *et al.* 2017 and Foulger *et al.* 2017 for detailed reviews). Their relationships with fluid-injection have been explained both conceptually (Doglioni 2017; Schmitt 2014; Ellsworth 2013) and physically through geomechanical modeling (e.g., Zhang *et al.* 2013), laboratory experiments (e.g., Guglielmi *et al.* 2015) and multi-scale observations (e.g., McGarr & Barbour 2017; Dahm *et al.* 2013).

Source/faulting properties are commonly resolved to identify, evaluate, and manage induced earthquakes. In many cases, focal mechanism solutions are used to infer the orientation and stress condition surrounding (often unmapped) reactivated faults. The double-couple (DC) component therein directly reflects the size and orientation of the reactivated fault and is generally well-constrained in induced seismogenic zones (e.g., western Canada, Wang *et al.* 2017a, 2017b; Oklahoma, U.S., Schoenball *et al.* 2018; Chen *et al.* 2017). The non-DC components reflect fault or fracture growth volume changes that may be associated with fluid injection/extraction. Whereas a few recent studies (e.g., Zhang *et al.* 2016; Zhao *et al.* 2014; Cesca *et al.* 2013) quantified the amount of non-DC components of induced events, characterizing and virtualizing non-DC components, especially those pertaining to fluid-injection induced earthquakes at the regional scale, remains a work in progress.

Among the various challenges, insufficient station density near focal zones and low accuracy in averaged (often 1-dimensional) regional structural models are the most glaring in assessing the non-DC contributions to fluid-induced events (e.g., Wang *et al.* 2016; Zhang *et al.* 2016). In this paper, I simultaneously decipher the DC and non-DC components in the source analyses of regional seismic events. The targets of this chapter are shallow (depth < 10 km) intraplate earthquakes in western Canada – a region where most induced seismicity is caused by hydraulic fracturing (Atkinson *et al.* 2016). This study presents the detailed characteristics of DC and non-DC components from well-resolved full moment tensors of induced events (2013-2017) and shallow intraplate tectonic earthquakes (1985-2007). I extend this analysis to the global scale based on four representative induced seismicity clusters (103 events) where full moment tensor solutions are available.

5.2 Background and datasets

5.2.1 Recent intraplate events in western Canada

The WCSB has been a seismically quiescent region historically. Only one known $M_w > 5$ earthquake ($M_w 5.1$ in 2001) was cataloged (Earthquakes Canada 2018) as a natural event occurred under presumed influences of regional tectonic forces. However, the regional seismic rate has increased exponentially since 2010, during which several felt earthquakes were reported (van der Baan & Calixto 2017) and linked to wastewater disposal (Schultz *et al.* 2014) or hydraulic fracturing (Atkinson *et al.* 2016). The largest induced earthquake occurred in 2015 in northern British Columbia, reaching a moment magnitude of 4.6 (Babaie Mahani *et al.* 2017) while others clustered near central (e.g., Fox Creek; Wang *et al.* 2016, 2017; Schultz *et al.* 2017) and southern (Schultz *et al.* 2015c) Alberta. Events in central Alberta are induced by different wells with separation distances as large as 40 km over a period of 4 years. Based on the regional seismic monitoring, no $M_L > 4$ events were reported in 2017, but the total number of $M_L > 3$ events surpassed that of previous years (Earthquake Canada, 2018).

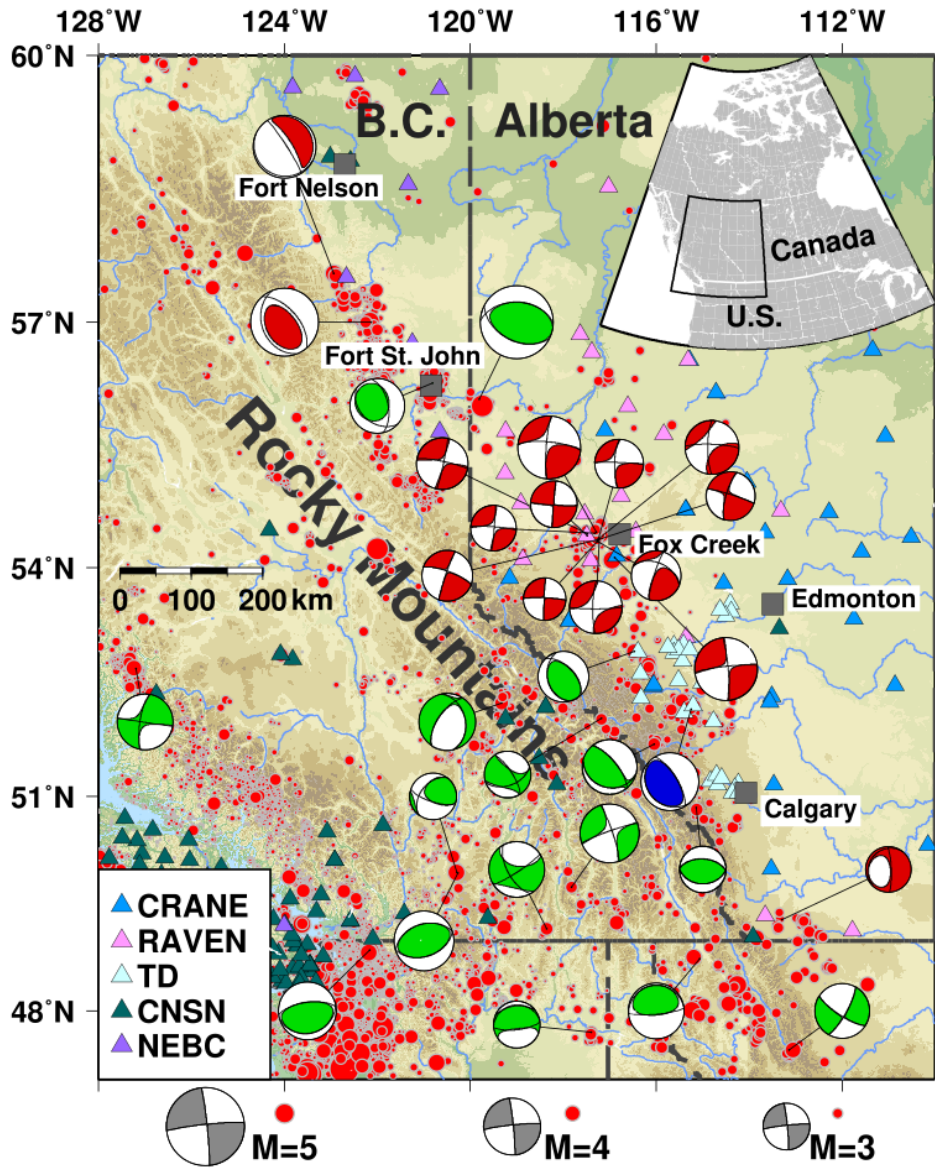


Figure 5.1: Distribution of stations (triangles) and earthquakes (small red circles) in western Canada (1985-2017). The magnitude-scaled “beachballs” show the focal mechanisms of tectonic (green), hydraulic-fracturing induced (red), and secondary recovery induced (blue) events. See list of abbreviations for the network names.

Distinct from the scattered natural events near the Canadian Rockies, the locations of recent earthquakes are inundated by industrial operations (Figure 5.1). Induced events form tight clusters within kilometers of suspected injection sites, which largely target two shale-gas formations: the Montney in northern British Columbia and the Duvernay in central-southern Alberta. The potential faults associated with recent clusters are smaller than, and away from, major thrust fault systems within the Canadian Rockies. Most of the events fall below the magnitude threshold of automatic moment tensor inversion and require a case-by-case analysis to delineate the reactivated fault geometry. By exploiting the expanding regional seismic networks, I systematically resolved the full moment tensors for Mw3-4 events and provided more reliable assessments of the non-DC components.

5.2.2 Representative world-wide cases

Globally, there have been more than 700 industrial sites with reported or suggested induced earthquakes, 88% of which are attributable to mining, waste-water disposal, oil/gas exploration, and geothermal exploitation (Foulger *et al.* 2017; Wilson *et al.* 2017). The largest magnitudes of most induced earthquakes are smaller than Mw2 - below the threshold of reliable full moment tensor retrievals based on regional networks largely designed for natural earthquake hazard monitoring. On the other end of the spectrum, the causes of some devastating earthquakes (Mw>7, e.g., the Wenchuan earthquake) are under debate as either natural or partially induced (Tao *et al.* 2015; Ge *et al.* 2009) and may not represent induced earthquakes with dominating anthropogenic contributions (if any). These debatable cases of seismicity are excluded from the moment-tensor decomposition in section 5.3.

To compare the WCSB events against induced earthquakes worldwide, I collected full moment tensors for events caused by 1) waste-water disposal in the central United States (see Supplementary materials; also see Huang *et al.* 2017 for the main catalogue), 2) mining activity in and around Germany (Cesca *et al.* 2013), 3) multistage hydraulic-fracturing stimulation in the Sichuan Basin, China (Lei *et al.* 2017, 2013), and 4) geothermal exploitation in California, United States (Martínez-Garzón *et al.* 2017; Guilhem *et al.* 2014). In addition, tectonic earthquakes in the central United States are included as a reference group to explore the potential differences between induced and natural earthquakes. All presented datasets share the common magnitude

range of Mw3-6 (see Appendix, Figure A4) to avoid potential mechanism differences between microseismic and regional scale earthquakes.

5.3 Results

5.3.1 Moment tensors solutions and decomposition

The expanding seismic network in the WCSB (Schultz & Stern, 2015) enable possible determinations of moment tensors for events as small as Mw3. To do so, I adopt a refined regional crustal model (see Figure A1) with location-based adjustments in the sedimentary layers (e.g., thinner for events further away from the mountain belt). During the time domain full moment tensor inversion, the displacement waveforms are filtered by 0.05-0.1 Hz, 0.08-0.4 Hz, and 0.4-0.9 Hz. The lowest frequency range is processed with a weight of five (compare to one for the high-frequency ranges) to ensure a similar contribution (i.e., peak amplitude) during the inversion procedure. For near source stations, all frequency ranges contain all phases (body and surface waves) whereas only first arrivals (mainly body waves) visible only at highest frequencies at far field stations (> 100 km) are fitted. For shallow earthquakes, a multi-frequency joint inversion approach (as adopted by this thesis) helps to reduce the potential trade-off between the non-DC components and focal depth. To assess the stability of fault plane orientations, I perform a bootstrap resampling test (Efron & Tibshirani, 1991) 200 times on randomly formed subsets containing $\sim 70\%$ of the original seismograms (Figure 5.4a) for events recorded by more than eight stations. Although other smaller events are recorded by fewer stations, synthetic tests conducted under a four-station scenario (see Appendix) indicate that the challenges to obtaining reliable moment tensor solutions are not insurmountable (Pakzad *et al.* 2018; Johnson *et al.* 2016). On the one hand, my preferred source location and velocity model show strong tolerance to noise level (Figure 5.4b) during synthetic tests with limited station coverage (see Appendix): consistent focal solutions containing positive CLVDs are resolved at all noise levels despite their relatively large amounts (compare with an input of 20%) when five or more times of the recorded noise are introduced. On the other hand, my joint inversions recover the input non-DC mechanisms (with $VR > 80\%$) when $\sim 10\%$ perturbations are applied to in the velocity model. Questionable results (i.e., incorrect non-DC mechanism or $VR < 50\%$) only occur when all velocities are

increased/decreased by 20%, which are extreme cases that are beyond my analysis. Based on the test results, I subjectively choose a $VR > 70\%$ as an indicator of reliable inversion outcomes for events in western Canada. I refer the readers to chapter 2 and the appendix for more details of the method, model, and discussions of their potential effects on the focal solutions based on simulations.

The final dataset contains 103 full moment tensors with 79 induced events. The decomposition of these events follows the convention of DC, CLVD, and the isotropic components as uniquely isolatable (see chapter 2 for details on decomposition). I also provide an alternative major/minor DC decomposition (Jost & Herrmann 1989) for events with consistent non-DC components in the WCSB. These two decomposition approaches favor different physical causes for induced events, and the outcomes will be discussed in section 5.5.2.

5.3.2 Moment magnitudes of recent events in the WCSB

For most studied $M_w \sim 4$ events in the WCSB, the M_w determined from the moment tensor inversions are consistently smaller than the reported M_L , which is measured from the peak amplitude of surface waves. Though the differences between various magnitude scales are widely observed worldwide, I find the discrepancy is larger than expected (i.e., as large as 0.8). Such inconsistency is particularly important for the regulation purpose since the traffic light system in both British Columbia and Alberta requires a suspension of corresponding HF well when an $M_L > 4$ earthquake occurred.

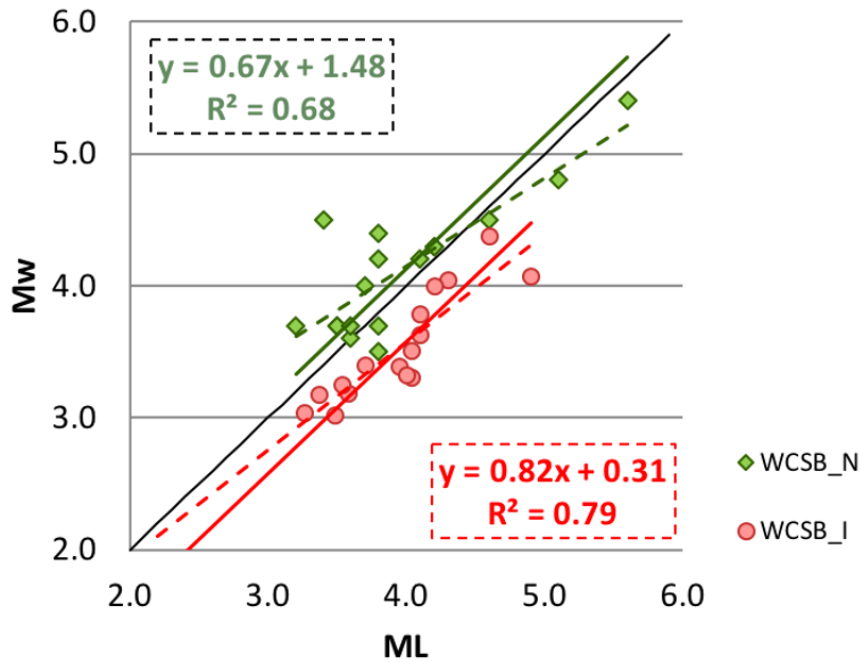


Figure 5.2: The difference between different magnitude scales. Green diamonds are natural ones, and red dots are recently induced ones. The equations in corresponding colors are best linear fits represented by the dashed lines. The solid lines show fits with a fixed slope (1), parallel to the black line representing $M_w = M_L$.

The recent recorded induced events form a valuable dataset to evaluate the relationship of $M_w - M_L$ in the WCSB (Figure 5.2). On average, M_L is 0.4 larger than M_w , in comparison with the reported range by Yenier (2017). However, the definition of M_w contains a scaling parameter (2/3), which should be taken into consideration when converting M_w into M_L . In Figure 5.2 I show that the slope from linear fits are much smaller than 1 for both natural and induced earthquakes. Thus, following Hanks and Kanamori (1979), I refine the relationship with a fixed slope of 2/3 and find the following relationship between the reported M_L and the determined M_w for the induced earthquake in the WCSB:

$$M = 2/3M_L + 0.91. \quad (21)$$

The constant (0.91) is comparable to that from Munafò *et al.* (2016) (1.15), who also generated an empirical M_w - M_L equation for small earthquakes ($0 < M_w < 3.8$) in central Italy, while much smaller than the empirical equation for $M_w > 4$ events in central Tibet (Tang *et al.* 2016; $M_w = 2/3M_L + 1.64$). In addition, my observed relationship roughly agrees with that from southern California ($M_w = 0.754M_L + 0.88$, Ross *et al.* 2016).

From equation 21, $M_w = M_L$ when the reported M_L is 2.73 and M_w will be significantly smaller than reported M_L for larger events, as observed in the WCSB (Yenier 2017). On the other hand, I can also derive that events with smaller M_L would expect larger M_w (e.g., when $M_L = 0$, $M_w = 0.91$). This negative relationship for smaller events is often neglected, possibly due to the fact that moment magnitude cannot be obtained from moment tensor inversion and individual smaller events are often ignored. However, the magnitude conversion for all ranges will lead to a smaller b-value when using M_L to fit the Gutenberg-Richter relationship (Ross *et al.* 2016).

The proposed conversion (Equation 21) should also be taken into consideration when examining the relationships between maximum magnitude of potentially induced earthquake and the total injection volume (Figure 5.3, also see McGarr 2014).

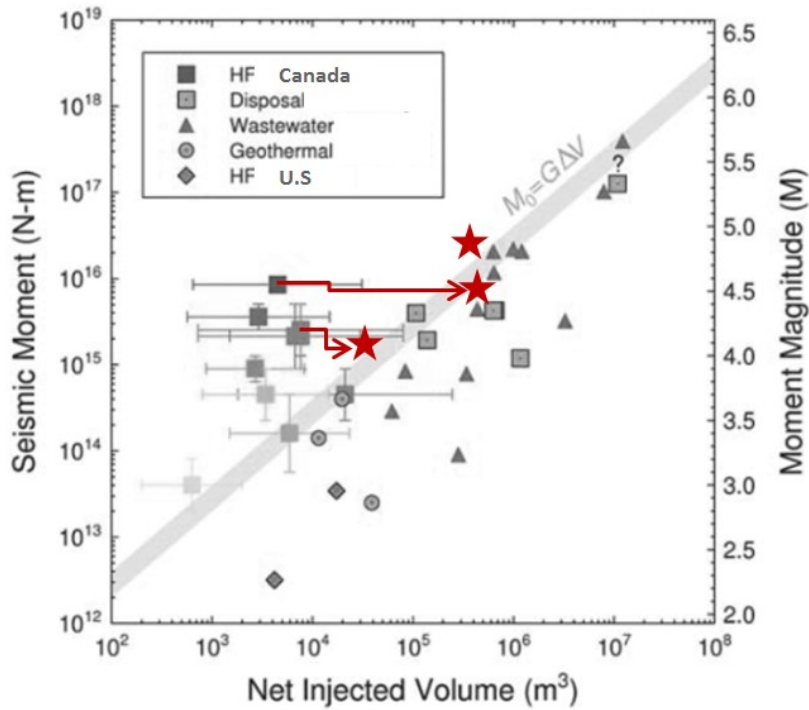


Figure 5.3: The relationship between seismic moment and total injected volume has been examined in a recent study by Atkinson et al. 2016, showing world's largest HF induced earthquakes (red stars). From top to bottom: $M_w=4.9$ ($252,000\text{m}^3$, Lei et al. 2017); $M_w=4.6$ ($320,000\text{m}^3$, Mahani et al. 2017); $M_w=4.1$ ($298,000\text{m}^3$, Wang et al. 2017a). The red arrows indicate how the coordinate for a specific event moves after obtaining the moment magnitude through moment tensor inversion and revised injection volumes. Figure modified after Atkinson et al. 2017 (with permission).

5.4 Moment tensor decompositions and implications

5.4.1 Double-couple faulting in western Canada

Prior to 2007, seventeen intraplate focal mechanisms were reported in western Canada, and all the related earthquakes occurred within the mountain belt (see Figure 5.1; Ristau *et al.* 2007). These mechanisms exhibit substantial variations in faulting regimes and strike orientations, partially due to the limited seismic station coverage before 2010 (Gu *et al.* 2010). In comparison, fault plane solutions for seven recent $M_w \sim 4$ events in this study are more stable and vary by less than 2.2° (Figure 5.4a). The P-axes are uniformly aligned along the NE-SW, consistent with the dominant crustal stress orientations in western Canada (Heidbach *et al.* 2016). Despite the differences in location, causes, and stabilities, focal mechanisms of events in western Canada mainly fall into two faulting categories: 1) thrust near the Canadian Rockies, and 2) strike-slip elsewhere (see Figure 5.1).

Both natural and induced events exhibit strike-slip dominated faulting mechanisms basinward from the Canadian Rockies. Many of these induced events are associated with operations that hydraulically fractured the Duvernay Formation (2.8-3.6 km depth, Dunn *et al.* 2012), which is within 1 km of the crystalline basement. Among the two candidate fault orientations (N-S or E-W), the existence of vertical N-S faulting system (within or above the basement) is supported by both geological and geophysical observations (Wang *et al.* 2017a; Schultz *et al.* 2016; Davies & Smith 2006; Duggan *et al.* 2001). At other locations, strike-slip dominated tectonic events show similar fault plane orientations to those of induced events, with a lone outlier in western British Columbia (52.7°N, 127.2°W, see Figure 5.1) where complex crustal structures around Vancouver Island might be largely responsible (Ellis *et al.* 1983).

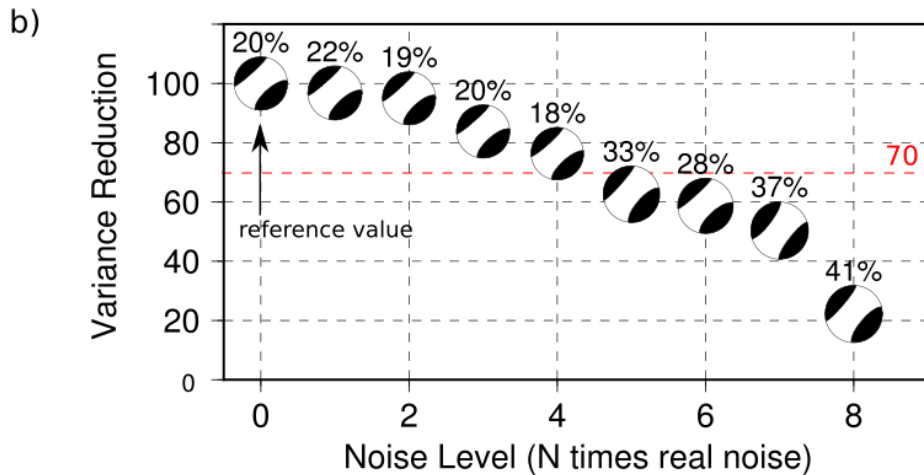
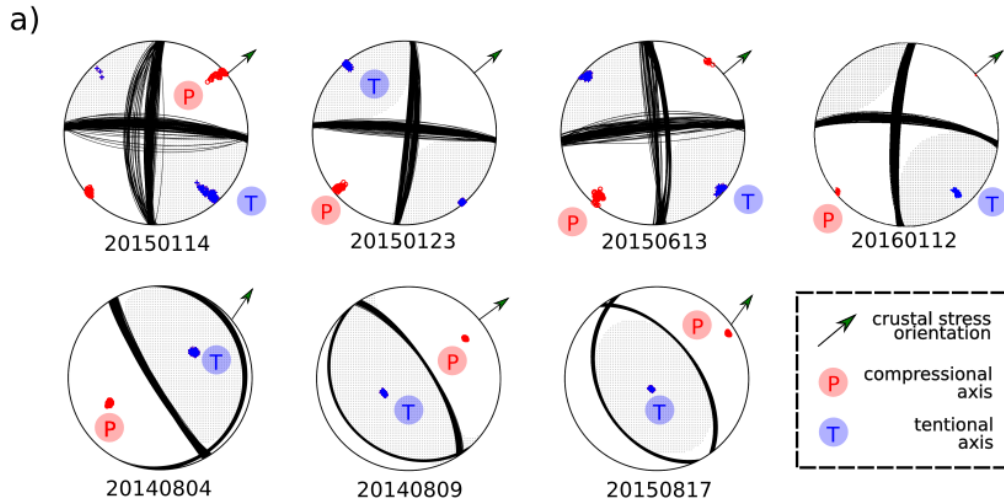


Figure 5.4: a) Examples of fault plane solutions (uniform sizes) determined from bootstrap resampling test for events in the WCSB. The P-axes are consistently aligned along NE-SW for both strike-slip (top) and reverse (bottom) faulting mechanisms, comparable to nearby S_H orientation (Heidbach et al. 2016). b) Variance reduction (fit) vs. noise level during synthetic tests (see Appendix for detailed results and test on velocity model variation). Real noise is multiplied by N times and added to synthetic waveforms generated with 20% of CLVD and 0% of isotropic components. Only the non-DC components after decomposition are plotted, and the corresponding percentages are labeled on top.

Along the Canadian Rockies, almost all events exhibit thrust-dominated faulting mechanisms. Natural events with thrust faulting slippages show variable strike orientations along E-W or NE-SW, including the Mw5.1 earthquake in 2001 (near Alberta and British Columbia border). An induced event in 2014 is located within northern British Columbia and shows either a near-vertical fault plane (84°), or a low-angle thrust fault (7°). The two remaining events with distinctive thrust components, i.e., a secondary recovery induced event in central Alberta and a hydraulic-fracturing induced case in northern British Columbia (see Figures 5.1 and 5.4), exhibit comparable (and moderate) dipping angles of 58° and 64° , respectively. The mechanisms of these two events are very similar to those of nearby (<100 km) tectonic earthquakes.

For both strike-slip and thrust faulting regimes, the maximum horizontal stress (S_H) and vertical stress are the respective maximum stress magnitudes (Schmitt 2014). My P-axis orientations from the focal mechanisms of recent earthquakes within the WCSB (see Figure 5.4) are predominantly along an NE-SW trend, which is consistent with the reported S_H direction in western Canada (Bell & Grasby 2012; Reiter *et al.* 2014). The similarity between natural and induced non-DC components suggests that the strain release during an earthquake is dominated by the crustal stress condition and pre-existing unmapped faults. This could manifest in induced earthquakes that are initiated by industrial activities, whereas the focal mechanisms are predominantly “pre-set” by the ambient stress condition and geology within the crust.

5.4.2 Interpretations of non-double-couple components

Despite known challenges in constraining non-DC components, I observe consistent CLVD motions from the strike-slip dominated events in central Alberta (Figure 5.5a). I decompose the deviatoric part of a moment tensor in two ways: 1) DC and CLVD, and 2) major and minor DCs (Jost & Herrmann 1989). Since the dominant DC components are mainly controlled by crustal stress condition and fault architecture (see section 5.4.1), the secondary components of the moment tensors likely reflect contributions from fault initiation by fluid involvement or complex/jogged fault structure. I consider the potential contributions from these two interpretations further.

First, it has been suggested that tensile cracks likely propagate along the S_H direction during hydraulic fracturing (Bell & Grasby 2012). At the microseismic scale (i.e., $M_w < 0$), large non-DC

components have been frequently documented and regarded as evidence for tensile-crack opening (Baig & Urbancic 2010; Šílený *et al.* 2009; Šílený & Milev 2008). A similar mechanism has been proposed for more sizeable events (-up to $M_w=2$) in geothermal regions (e.g., Foulger & Long 1984). My moment tensor decomposition analysis suggests that similar physical processes may contribute to hydraulic-fracturing induced events in the WCSB (Figure 5.5b). Both the resolved CLVD components and regional S_H orientations (Reiter *et al.* 2014) are aligned subparallel to the NE-SW direction, consistent with hydraulic fracture propagation during stage stimulations. For earthquakes in the WCSB, the CLVD components ($M_w 2.1-3.8$) are usually smaller than the DC components ($M_w 3.1-4.4$) but above the microseismic range ($M_w < 0$). In fact, the estimated fracture opening for a crack with 300 m length would be a few centimeters (seismic potency $P_0 \sim 0.1 \text{ km}^2\text{cm}$, Ben-Zion, 2008), which is capable of producing a $M_w \sim 3$ non-DC event. Specific to the Duvernay, a 200 m length was used as an acceptable estimate for geomechanical modeling of fracture propagation (Lele *et al.* 2017), and ~ 1 cm fracture apertures are observed when higher viscosity fluids are used (Maxwell *et al.* 2016). The chosen length dimension is at the high end of hydraulic fracturing cases, where fractures grow up to hundreds of meters in length (Wilson *et al.* 2018; Davies *et al.* 2012). In addition, the limited amounts of isotropic components are disproportional to the CLVD for purely tensile cracks. Therefore, the above explanation may only partially explain the consistent CLVD, specific to the anticipated shearing motion of ~ 3 cm on a $\sim 1 \text{ km}^2$ fault in connection with a $M_w \sim 4$ strike-slip event.

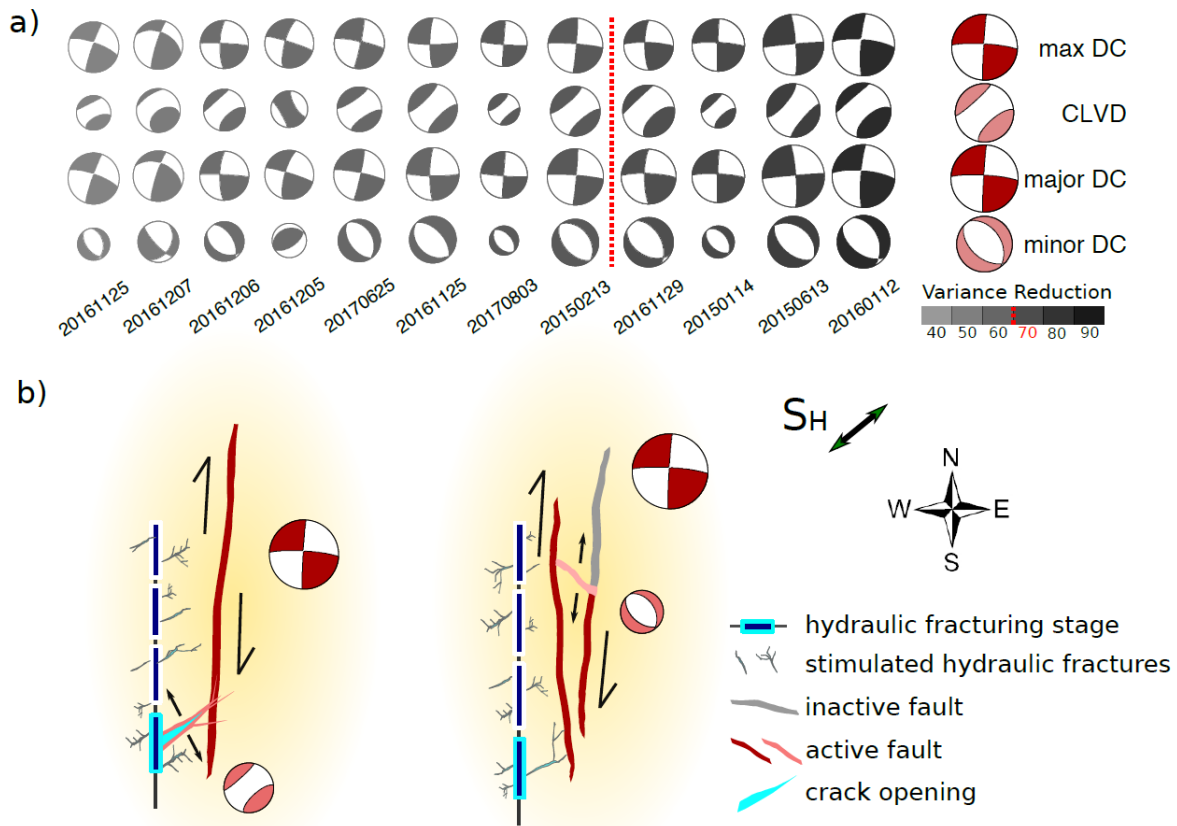


Figure 5.5: Decomposition of the deviatoric parts for the hydraulic fracturing induced events in central Alberta. The event dates are indicated at the bottom and sizes of the different components are scaled to the magnitudes. Events are aligned by variance reduction values (see legend for the shade) and the red dashed line indicated 70% value. Two methods are presented: max DC and CLVD (rows 1-2) or major DC and minor DC (rows 3-4). Normalized summations of each row are on the right. All decompositions are consistent regardless of the magnitude and date of these events, except for the event on 5 December 2016. b) Map view of the interpretations of the two decomposition styles related to hydraulic fracturing: CLVD components (left) and minor DC components (right). Black arrows indicate relative motions. The minor fault (right) is extensional possibly due to the external pressure load on the highly fractured zone along the HF well.

Alternatively, the minor DCs show consistent NW-SE aligned normal faults. In other words, minor faults could have slipped as a part of an extensional duplex connecting the dextral N-S (and subvertical) shear slips (Figure 5.5b). The averaged magnitude difference between major and minor DCs is 0.8: assuming both the major and connecting (minor) faults share similar rupture distances, this corresponds to a tenfold fault length difference (Hanks & Kanamori, 1979). A strike-slip fault system with transtensional flower structure has been supported by geological evidence (Wang *et al.* 2016; Berger & Davies 1999), as well as by recent seismic imaging at the basement depth in the Fox Creek area (Corlett *et al.* 2018; Chopra *et al.* 2017). It is highly possible for transtensional faults to develop within the limited zone between *en echelon* fault strands (Sylvester 1988). For matured complex fault zones, the connecting segments usually contain both thrust and normal faults (depends on their orientations and develop history), which deviate from simplified textbook examples. Interestingly, these fault structures are often related to vertical fluid flow (Cox 2016; Davies & Smith 2006) – a condition required for induced seismicity.

In summary, the orientation of CLVD components for hydraulic-fracturing induced earthquakes offers tangible evidence for either crack opening or co-slipping on a transtensional fault system (see Figure 5.5b). The former explanation is typically favored by microseismicity/geothermal induced events, while the latter mechanism is common for natural events under tectonic environments (Frohlich 1994). Because induced earthquakes may be treated as a mix of these two classes of seismicity, I cannot rule out the possibility that both interpretations may be valid for the earthquakes in central Alberta.

5.4.3 The non-DC component: prevalence and implications

The non-DC components provide details on how fluid injection/extraction reactivates (more realistic) faults, with multiple physical explanations. However, improperly constrained non-DC components could lead to confounding reasoning or misinterpretation (Vavryčuk *et al.* 2008). Many factors, including hypocentral location, station coverage, and velocity model, may affect the resolution and amount of non-DC contributions. For example, a large non-DC may be introduced due to insufficient coverage during bore-hole monitoring (Eyre & van der Baan 2017). Insufficient station coverage is particularly concerning for focal mechanism solutions of natural earthquakes in the WCSB, especially those before 2010. To mitigate undesired hypocentral and structural

effects, I carefully compare and select input hypocenter locations from multiple sources and use industry-verified depths (see supplementary material of Wang *et al.* 2018). I also examine the potential relationship between my observed amounts of non-DC in western Canada with earthquake depth and magnitude and found no clear relationships (Figure 5.6). This may be attributable to the variations in the amounts of non-DC components.

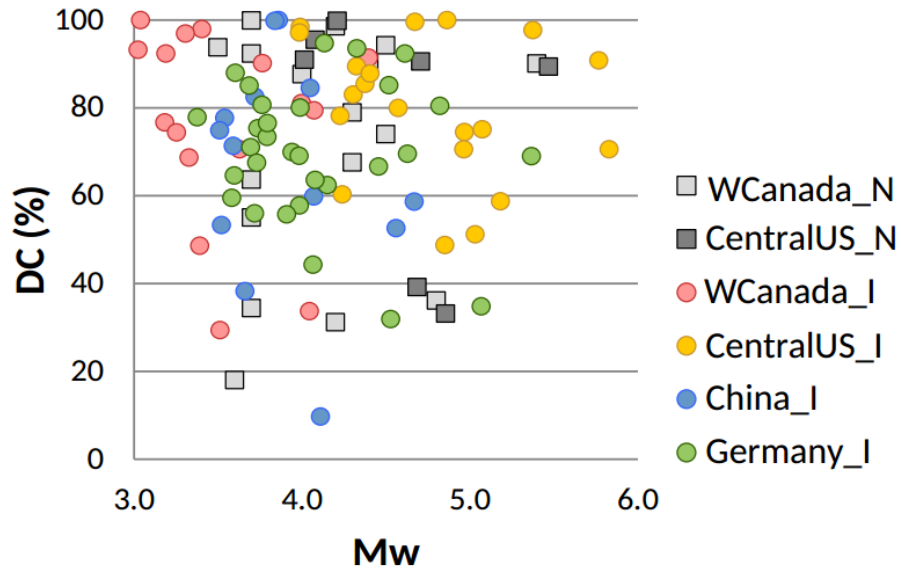


Figure 5.6: Percentage of DC components v.s. moment magnitude for the studied earthquake catalogs.

The statistics of the decompositions of the collected datasets show comparable amounts of non-DC among six independent categories (Figure 5.7a). This result raises questions about the effectiveness of using non-DC as a reliable metric in identifying an induced event (e.g., Zhang *et al.* 2016; Dahm *et al.* 2013). On the one hand, I observe very limited (~3%) isotropic components from induced events in the WCSB, which differ greatly from fluid induced earthquakes during geothermal (i.e., Martínez-Garzón *et al.* 2017) and mining-related (Cesca *et al.* 2013) activities. Figure 5.7b shows a 2-D Hudson’s plot, which partitions a full moment tensor of an earthquake into DC, CLVD and isotropic components (Hudson *et al.* 1989). Most of the induced events in the WCSB are located within the 4th quadrant of Hudson’s plot, which corresponds to tensile crack

opening with a limited volume increase. In contrast, events located in Germany (mostly mining induced) are more randomly distributed in all four quadrants, showing greater isotropic components. The results suggest that the volume changes during hydraulic fracturing are only responsible for an isotropic component less than 10% of the total moment during an Mw3 earthquake (i.e., Mw2.4), a value considerably smaller than those previously proposed for events in the WCSB (Zhang *et al.* 2016). Natural and induced intraplate events in western Canada exhibit comparable amounts (29% vs. 20% on average, respectively) of CLVD as well as substantial variations (see Figure 5.7a). Large variations in the CLVD components are also observed for both types of earthquakes in central United States; unfortunately, their isotropic components have been preset to zero during moment tensor solutions (Global Centroid Moment Tensor solutions). Overall, due to the marginal differences among the various earthquake types, I suggest that the proper determination of the nature of an event (induced or natural) should rely more on the background seismicity and the spatiotemporal correlation to industry activities rather than its focal mechanism.

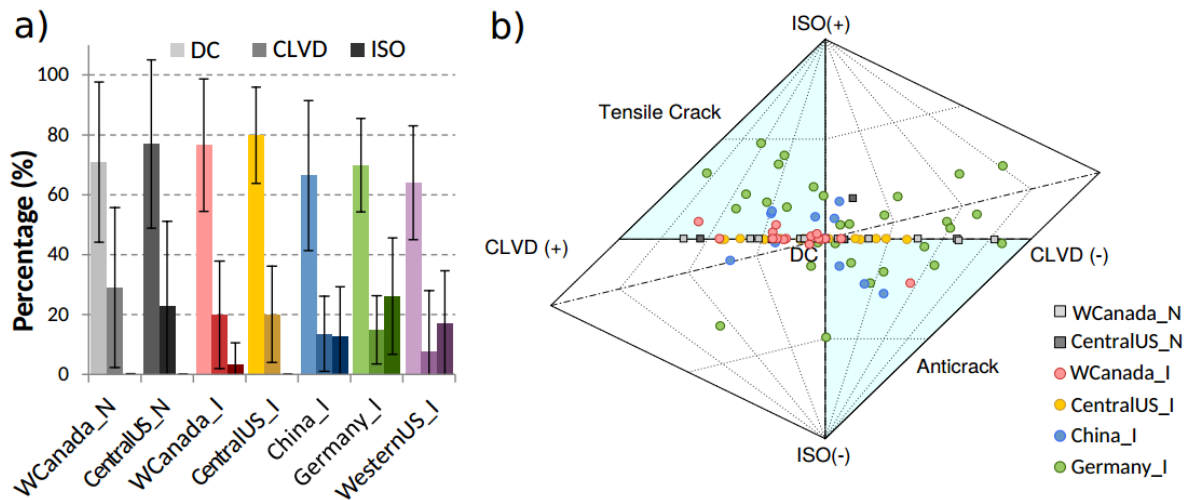


Figure 5.7: Decompositions of the collected dataset. a) Averaged percentages (shaded bars) and standard deviations (black error bars) of the DC, CLVD, and isotropic components (ISO). b) Hudson's plot summarizing the decomposed moment tensors for the listed regions. Geothermal induced events (purple bars) in the western U.S. are only presented in Figure a (moment tensor values are unavailable). For both plots, tectonic events (labeled with 'N') are shown in grey scale, and induced events (labeled with 'I') are shown in color.

Given the apparent lack of distinction between non-DC components for natural and induced events, I further speculate on the implications for natural events. In western Canada, the intraplate events vary substantially in location and possibly also involve slippages on *en echelon* faults other than the major mapped faults. For example, nonplanar faulting systems are common for large-scale natural events with significant non-DC components, as evidenced by vertical CLVDs (“eyeballs”) observed in volcanic regions (e.g., Shuler *et al.* 2013; Minson *et al.* 2007) and horizontal CLVDs (“baseballs”) near mid-ocean ridges (e.g., Miller *et al.* 1998; Frohlich 1994). Regardless of the nature of an earthquake, complex regional fault systems can produce CLVD components via similar mechanisms. Assisted by dynamic triggering stresses (Wang *et al.* 2015), the fluid-fault interaction (Cox 2016) rationale can also be responsible for the slippages of critically stressed faults that produced natural earthquakes. For the isotropic component, mass perturbation due to injection/extraction does not ensure a larger volume change in each of related

earthquake and therefore may be case specific (e.g., hydraulic fracturing and volcanic earthquakes may contain lower isotropic components than previously suspected). Taken together, both the uncertainties and complex source physics can lead to the indistinguishable amounts of non-DC between natural and induced events at regional scales.

5.5 Summary

This chapter presents our first and preliminary collection of focal mechanisms from several key regions with human-induced earthquakes (and their interpretations). My integrated evaluation of recent intraplate earthquakes in western Canada, as well as several worldwide clusters, leads to the following conclusions:

- The focal mechanisms of the induced earthquakes in the WCSB can be separated into strike-slip events within central Alberta and thrust faulting events along the Canadian Rockies, similar to tectonic earthquakes.
- Events in Fox Creek contain minimal isotropic components while sharing highly consistent CLVD components with P-axis orientated along NE-SW. I interpreted this as a consequence of tensile crack opening and/or *en echelon* faults co-slipping.
- Induced events in western Canada have comparable non-DC components to those of natural and induced earthquakes elsewhere, leaving their focal mechanisms indistinguishable. I speculate that this may mean fluid-fault interactions or complex fault architectures play an important role in natural intraplate events too.

6 Conclusions and Future Work

6.1 Conclusions

The increasing seismic rate in the WCSB raises many critical questions pertaining to the seismic hazard assessment of shale gas development. Whereas examination of the nature of surrounding earthquakes relies on the accurate determination of the source locations as well as their temporal relationship to nearby industrial activities. To understand the relationships between earthquakes, industrial activities, and the local geological framework, other evidence from source parameters are also critical. In this thesis, I examined seismicity in and around the WCSB recorded in the past decade, with special interest in their source parameters. Chapter 1 presents the seismicity and industrial background and chapter 2 introduces the key methods adopted in this thesis. My findings are presented in chapters 3-5 in detail.

The first $M_L > 4$ induced earthquake in Alberta occurred on June 13, 2015. Chapter 3 focus on this first red-light event and point out the potential fault orientations (N-S or E-W) with various tests on velocity model and source location to prove the robustness of the resolved focal mechanism. My moment tensor inversions lead to a moment magnitude of 3.9, smaller than the reported M_L of most agencies. The potentially related HF wells are also listed based on improved location through our grid search. This chapter was published as one of the earliest papers on the HF-induced events in western Canada, a study region that attracted significant scientific interest (to date, with three publications in *Science*).

The seismic rate continued to grow with the HF activities on the Duvernay formation, and the largest HF induced earthquake in Alberta occurred on January 12, 2016. Chapter 4 inherited the analysis of source parameters for the first $M_L > 4$ HF induced event and adopted the local array to detect, locate and analyze the associated cluster of this second “red-light” event. Whereas similar fault solutions are found, my detected cluster prefers the N-S fault orientation. I proposed the positive flower type of fault system to explain the strike-slip events in 2016-2017 around Crooked Lake/Fox Creek, Alberta. With the growing seismic monitoring network, future work could

expand such comparison by including more case studies and filling the magnitude gaps (i.e., between Mw0-3), which would enhance our understanding and regulation of induced seismicity.

In chapter 5, I switch the scope from case-studies of HF-induced seismicity to all types of events worldwide, with a specific focus on the non-double-couple components within the shallow intraplate earthquakes. I first show that recent Mw~4 induced earthquakes in western Canada can be categorized into strike-slip and reverse-faulting regimes, similar to tectonic ones. Using over 100 full moment tensors collected all over the world, I show that induced earthquakes exhibited indistinguishable amounts of non-DC components from tectonic earthquakes. Furthermore, consistent CLVD components observed from the HF-induced earthquakes in central Alberta may reflect fault/fracture growth or *en echelon* faults slipping. This fluid-fault interaction is consistent with the physics behind natural volcanic earthquakes, which encourage future studies focusing on the similarity between natural and induced earthquakes.

By utilizing techniques normally employed for the analysis of active source data and global seismology, my research aims to provide insights into both the regional structures and complex source properties. Understanding the occurrence of regional (especially induced) seismicity is the knowledge foundation for decision-makers. For instance, one may prevent/minimize induced earthquakes by optimal the injection strategies. Overall, the outcomes of the proposed integrated analysis will assist researchers and regulators to assess the seismic hazard in western Canada, central U.S. as well as other regions with increasing seismicity.

6.2 Future work

This thesis provides fundamental analysis on the ones in the WCSB. For the hydraulic-fracturing induced events in central Alberta, future work could base on the on-hand packages as well as geological knowledge: on the one hand, both the threshold of event detection (i.e., M&L, hypoDD) and moment tensor inversion (i.e., TDMT_INV, gCAP) could be reduced even further with the growing seismic network. My cluster analysis is conducted only for a few local regions due to the data-driven nature of this research. Future work may consider applying similar methods to different clusters (e.g., natural earthquakes in and around Peace River region and mining blasts within the Rocky Mountains). On the other hand, anisotropy, heterogeneity could be considered

in a 3D velocity model to improve the resolution as well as counter-balance the raising standard requirement for high-frequency ranges or lower event magnitude threshold.

Another issue left unsolved is related to the mining-blasts: waveform-based analysis in both time and frequency domain failed to tell earthquakes and mining blasts apart, mainly attributable to low SNR and complex structure within the mountains. It is worth noting that the studied mining-related activities were recorded between 2006 and 2010 - a period with much lower station coverage than the present day. Despite the challenges, it is highly likely that a few earthquakes were categorized as mining blasts) within this period and potentially more mis-determined cases exist after 2010. Even though open-pit mines are less likely to induce earthquakes, the outliers within the mining dataset worth careful examination. A robust determination may rely on access to industrial blasts records and/or waveform-based discrimination methods. Furthermore, those repeating mining-blasts can be utilized as regional sources to investigate the Moho structure below the mountains, as stations within a few hundreds of kilometers toward the east of the Rocky Mountains show clear Pp arrivals.

In short, this thesis only provides basic answers to the occurrences of induced earthquakes in western Canada from the source property aspects. To fully understand their origins and provide effective risk assessment, one needs to gain access to the industry owned catalog or event records from the dense monitoring network, incorporate the geologic factors in the seismic hazard prediction and aim for a site-based probability seismic hazard analysis. Recent fashion of applying machine learning techniques to seismology have made significant progress on event detection as well as identifying key industrial factors (e.g., injection volume, depth, pressure) for induced earthquakes (e.g., Pawley *et al.* 2018; Holtzman *et al.* 2018). The data sharing, close monitoring, and collaboration between industry, regulators and academic institution are the foundations for future analysis of induced seismicity (Eaton, 2018; Karimi *et al.* 2018). In addition, one should not be limited to the current target of finding and understanding the induced seismicity only. Both natural earthquakes and mining blasts data are valuable datasets for the overall understanding of both regional tectonics and seismic hazard.

Bibliography

Ake, J., Mahrer, K., O'Connell D., & Block, L. (2005). Deep-injection and closely monitored induced seismicity at Paradox Valley, Colorado, *Bull. Seismol. Soc. Am.*, 95(2), 664–683, doi:10.1785/0120040072.

Aki, K., & Richards, P. G. (1980). Quantative seismology: Theory and methods. New York, 801.

Alberta Energy Regulator, (2015). Subsurface order 2. (Available at <https://aer.ca/documents/orders/subsurface-orders/SO2.pdf>.)

Atkinson, G.M., Greig, D.W., & Yenier, E. (2014). Estimation of moment magnitude (M) for small events ($M < 4$) on local networks, *Seismol. Res. Lett* 85(5), 1116–1124, doi:10.1785/0220130180.

Atkinson, G.M., Eaton, D.W., Ghofrani, H., Walker, D., Cheadle, B., Schultz, R., ... & Liu, Y. (2016). Hydraulic fracturing and seismicity in the Western Canada Sedimentary Basin. *Seismol. Res. Lett*, 87(3), 631-647, DOI: 10.1785/0220150263.

Arrowsmith, S. J., Arrowsmith, M. D., Hedlin, M. A., & Stump, B. (2006). Discrimination of delay-fired mine blasts in Wyoming using an automatic time-frequency discriminant. *Bulletin of the Seismological Society of America*, 96(6), 2368-2382.

Babaie Mahani, A., Schultz, R., Kao, H., Walker, D., Johnson, J., & C. Salas (2017). Fluid injection and seismic activity in the northern Montney play, British Columbia, Canada, with special reference to the 17 August 2015 Mw 4.6 induced earthquake.

Bachu, S. (1993). Basement heat flow in the Western Canada sedimentary basin, *Tectonophysics*, 222(1), 119–133, doi:10.1016/0040-1951(93)90194-O.

Baig, A., & Urbancic, T. (2010). Microseismic moment tensors: A path to understanding frac growth. *The Leading Edge*, 29(3), 320-324.

Bao, X., & Eaton, D. W. (2016). Fault activation by hydraulic fracturing in western Canada. *Science*, aag2583.

BC Oil and Gas Commission (2012). Investigation of observed seismicity in the Horn River Basin. (Available at <http://www.bcogc.ca/sites/default/files/documentation/technical-reports/investigation-observed-seismicity-montney-trend.pdf>.)

BC Oil and Gas Commission (2014). Investigation of observed seismicity in the Montney Trend. (Available at <http://www.bcogc.ca/document.aspx?documentID=1270>), (December), 32.

Bell, J. S., & Grasby, S. E. (2012). The stress regime of the Western Canadian sedimentary basin. *Geofluids*, 12(2), 150-165.

Ben - Zion, Y. (2008). Collective behavior of earthquakes and faults: Continuum - discrete transitions, progressive evolutionary changes, and different dynamic regimes. *Reviews of Geophysics*, 46(4).

Bent, A. L. (2011). Moment magnitude (M_w) conversion relations for use in hazard assessment in eastern Canada, *Seismol. Res. Lett.*, 82(6), 984–990.

Berger, Z. & Davies, G.R. (1999.) The development of linear hydrothermal dolomite (HTD) reservoir facies along wrench or strike slip fault systems in the Western Canada Sedimentary Basin. *Canadian Society of Petroleum Geologists Reservoir*, 26(1), 34-38.

Berger, Z. & Zaitlin, B.A. (2011). Detection and analysis of structurally controlled enhanced reservoir potential in mature and emerging oil resource plays in the WCSB: tight oil examples from the Nordegg and Alberta Bakken. *CSPG CSEG CWLS Convention*.

Beirlant, J., Kijko, A., Reynkens, T., & Einmahl, J. H. (2017). Estimating the maximum possible earthquake magnitude using extreme value methodology: the Groningen case. *Natural Hazards*, 1-23.

- Berman, R., Davis, W., & Pehrsson, S. (2007). Collisional Snowbird tectonic zone resurrected: Growth of Laurentia during the 1.9 accretionary phase of the Hudsonian orogeny, *Geology*, 35(10), 911–914, doi:10.1130/G23771A.1
- Bowers, D., & Hudson, J. A. (1999). Defining the scalar moment of a seismic source with a general moment tensor. *Bulletin of the Seismological Society of America*, 89(5), 1390-1394.
- Brune, J. N. (1970). Tectonic stress and the spectra of seismic shear waves from earthquakes, *J. Geophys. Res.*, 75(26), 4997–5009.
- CBC news (2016). Fox Creek fracking operation closed indefinitely after earthquake (Available at <http://www.cbc.ca/news/canada/edmonton/fox-creek-fracking-operation-closed-indefinitely-after-earthquake-1.3400605>.)
- Cesca, S., Rohr, A., & Dahm, T. (2013). Discrimination of induced seismicity by full moment tensor inversion and decomposition. *J. Seismol.*, 17(1), 147-163. doi:10.1007/s10950-012-9305-8.
- Chen, W., Ni, S., Kanamori, H., Wei, S., Jia, Z., & Zhu, L. (2015a). CAPjoint, a computer software package for joint inversion of moderate earthquake source parameters with local and teleseismic waveforms, *Seismol. Res. Lett.*, 86(2A), 432–441, doi:10.1785/0220140167
- Chen, Y., Gu, Y.J., Dokht, R.M. & Sacchi, M.D. (2015b). Crustal imprints of Precambrian orogenesis in western Laurentia, *J. Geophys. Res. Solid Earth*, 120, 5051–5069, doi:10.1002/2014JB011802.
- Chen, X., Nakata, N., Pennington, C., Haffener, J., Chang, J. C., He, X., ... & Walter, J. I. (2017). The Pawnee earthquake as a result of the interplay among injection, faults and foreshocks. *Scientific Reports*, 7(1), 4945.
- Chopra, S., Sharma, R. K., Ray, A. K., Nemat, H., Morin, R., Schulte, B., & D'Amico, D. (2017). Seismic reservoir characterization of Duvernay shale with quantitative interpretation and induced seismicity considerations—A case study. *Interpretation*.

Clerc, F., Harrington, R.M., Liu, Y., & Gu, Y.J. (2016). Stress drop estimates and hypocenter relocations of induced seismicity near Crooked Lake, Alberta. *Geophys. Res. Lett.*, 43(13), 6942-6951.

Clowes, R. M., Burianyk, M. J., Gorman, A. R., & Kanasewich, E. R. (2002). Crustal velocity structure from SAREX, the Southern Alberta Refraction Experiment, *Can. J. Earth Sci.*, 39(3), 351–373, doi:10.1139/e01-070.

Corlett, H., Schultz, R., Branscombe, P., Hauck, T., Haug, K., MacCormack, K., & Shipman, T. (2018). Subsurface faults inferred from reflection seismic, earthquakes, and sedimentological relationships: Implications for induced seismicity in Alberta, Canada, *Marine and Petroleum Geology*, ISSN 0264-8172, <https://doi.org/10.1016/j.marpetgeo.2018.03.008>.

Cortis, A., Ollenberger, L., & Fawcett, M. (1997). Simonette Beaverhill Lake oil field: a multi-cyclic approach to understanding reef growth and reservoir heterogeneity. *CSPG-SEPM Joint Convention*, 73-88.

Cox, S. F. (2016). Injection-driven swarm seismicity and permeability enhancement: Implications for the dynamics of hydrothermal ore systems in high fluid-flux, overpressured faulting regimes— An invited paper. *Economic Geology*, 111(3), 559-587, doi: [10.2113/econgeo.111.3.559](https://doi.org/10.2113/econgeo.111.3.559).

Crotwell, H. P., Owens, T. J., & Ritsema, J. (1999). The TauP Toolkit: Flexible seismic travel-time and ray-path utilities. *Seismological Research Letters*, 70, 154-160.

Dahm, T., Becker, D., Bischoff, M., Cesca, S., Dost, B., Fritschen, R., ... & Meier, T. (2013). Recommendation for the discrimination of human-related and natural seismicity. *Journal of Seismology*, 17(1), 197-202.

Davies, G.R. & Smith, Jr, L.B. (2006). Structurally controlled hydrothermal dolomite reservoir facies: An overview. *AAPG bulletin*, 90(11), 1641-1690.

Davis, M. & Karlen, G. (2014). A regional assessment of the Duvernay Formation; a world-class liquids-rich shale play. *GeoConvention: Integration, Calgary*, 6-10. 2013

DeMets, C., Gordon, R. G., Argus, D. F., & Stein, S. (1990). Current plate motions. *Geophysical journal international*, 101(2), 425-478.

Deng, K., Liu, Y., & Harrington, R. M. (2016). Poroelastic stress triggering of the December 2013 Crooked Lake, Alberta, induced seismicity sequence. *Geophys. Res. Lett.*, 43(16), 8482-8491.

Dixon, J. (2000). Regional lithostratigraphic units in the Triassic Montney Formation of western Canada. *Bulletin of Canadian Petroleum Geology*, 48(1), 80-83.

Dreger, D.S. (2003). TDMT_INV: Time domain seismic moment tensor inversion, *Int. Handb. Earthquake Eng. Seismolog.*, 81b, 1627.

Dogliani, C. (2017). A classification of induced seismicity. *Geoscience Frontiers*. ISSN 1674-9871.

Duggan, J.P., Mountjoy, E.W., & Stasiuk, L.D. (2001). Fault-controlled dolomitization at Swan Hills Simonette oil field (Devonian), deep basin west-central Alberta, Canada. *Sedimentology*, 48(2), 301-323. doi: 10.1046/j.1365-3091.2001.00364.x

Dunn, L., Schmidt, G., Hammermaster, K., Brown, M., Bernard, R., Wen, E., ... & Gardiner, S. (2012). The Duvernay Formation (Devonian): sedimentology and reservoir characterization of a shale gas/liquids play in Alberta, Canada. *In Canadian Society of Petroleum Geologists, Annual Convention, Calgary*

Earthquakes Canada, <http://earthquakescanada.nrcan.gc.ca/stndon/NEDB-BNDS/bull-en.php>, last access: Jan 2018.

Eaton, D. W. & A. B. Mahani (2015). Focal mechanisms of some inferred induced earthquakes in Alberta, Canada, *Seismol. Res. Lett.*, 86(4), 1–8, doi:10.1785/0220150066.

Eaton, D. W., & Schultz, R. (2018). Increased likelihood of induced seismicity in highly overpressured shale formations. *Geophysical Journal International*, 214(1), 751-757.

Eaton, D., Igonin, N., Poulin, A., Weir, R., Zhang, H., Pellegrino, S. and Rodriguez, G., 2018. Induced seismicity characterization during hydraulic fracture monitoring with a shallow-wellbore geophone array and broadband sensors. *Seismol. Res. Lett.*, in press.

Eaton, D. W. (2018). Passive Seismic Monitoring of Induced Seismicity: Fundamental Principles and Application to Energy Technologies. *Cambridge University Press*.

Efron, B. & Tibshirani, R. (1991). Statistical data analysis in the computer age, *Science*, 253(5018), 390–395

Ellsworth, W.L. (2013). Injection-induced earthquakes, *Science*, 341, 6142, doi:10.1126/science.1225942.

Elsworth, D., Spiers, C. J., & Niemeijer, A. R. (2016). Understanding induced seismicity. *Science*, 354(6318), 1380-1381.

Ellis, R. M., Spence, G. D., Clowes, R. M., Waldron, D. A., Jones, I. F., Green, A. G., ... & Kanasewich, E. R. (1983). The Vancouver Island Seismic Project: a co-CRUST onshore–offshore study of a convergent margin. *Canadian Journal of Earth Sciences*, 20(5), 719-741.

Evans, K. F., Zappone, A., Kraft, T., Deichmann, N., & Moia, F. (2012). A survey of the induced seismic responses to fluid injection in geothermal and CO₂ reservoirs in Europe. *Geothermics*, 41, 30-54.

Eyre, T. S. & van der Baan, M. (2017). The Reliability of Microseismic Moment Tensor Solutions: Surface versus Borehole Monitoring. *Geophysics*, 82(6), 1-46.

Fan, W. & Shearer, P. M. (2016). Local near instantaneously dynamically triggered aftershocks of large earthquakes. *Science*, 353(6304), 1133-1136, doi: 10.1126/science.aag0013

Farahbod, A. M., Kao, H., Walker, D. M., & Cassidy, J. F. (2015). Investigation of regional seismicity before and after hydraulic fracturing in the Horn River Basin, northeast British Columbia, *Can. J. Earth Sci.*, 52(2), 112–122, doi:10.1139/cjes-2014-0162.

- Farrugia, D., Paolucci, E., D'Amico, S., & Galea, P. (2015). Inversion of surface wave data for shear wave velocity profiles: Case studies of thick buried low-velocity layers in Malta, *Geophysical Research Abstracts* Vol. 17, EGU2015-448 presented at 2015 EGU General Assembly, Vienna, Austria, 12–17 Apr
- Fouch, M. J. & Rondenay, S. (2006). Seismic anisotropy beneath stable continental interiors. *Physics of the Earth and Planetary Interiors*, 158(2), 292-320.
- Foulger, G. & Long, R. E. (1984). Anomalous focal mechanisms: Tensile crack formation on an accreting plate boundary. *Nature*, 310(5972), 43-45.
- Foulger, G. R., Wilson, M., Gluyas, J., Julian, B. R., & Davies, R. (2017). Global review of human-induced earthquakes. *Earth-Science Reviews*.
- Frohlich, C. (1994). Earthquakes with non-double-couple mechanisms. *Science*, 264(5160), 804-809.
- Fox, D.A. & Soltanzadeh, M. (2015). A regional geomechanical study of the Duvernay Formation in Alberta, Canada, *GeoConvention 2015: New horizons*.
- Friberg, P. A., Besana-Ostman, G. M., & Dricker, I. (2014). Characterization of an earthquake sequence triggered by hydraulic fracturing in Harrison County, Ohio, *Seismol. Res. Lett.*, 85(6), 1295–1307, doi:10.1785/0220140127
- Frohlich, C. (1994). Earthquakes with non-double-couple mechanisms. *Science*, 264(5160), 804-809.
- Ge, S., Liu, M., Lu, N., Godt, J. W., & Luo, G. (2009). Did the Zipingpu Reservoir trigger the 2008 Wenchuan earthquake?. *Geophysical Research Letters*, 36(20).
- Ghofrani, H. & Atkinson G. N. (2016). A Preliminary Statistical Model for Hydraulic Fracture-Induced Seismicity in the Western Canada Sedimentary Basin (WCSB), *Geophys. Res. Lett.*, 43, doi:10.1002/2016GL070042.

Globalnews (2016). Fox Creek mayor concerned by oilpatch impacts after earthquake: <http://globalnews.ca/news/2452038/fox-creek-mayor-concerned-by-oilpatch-impacts-after-earthquake/>

Goldstein, P. A. U. L., & Snoke, A. (2005). SAC availability for the IRIS community. *Incorporated Research Institutions for Seismology Newsletter*, 7(UCRL-JRNL-211140).

Green, D.G. & Mountjoy, E.W. (2005). Fault and conduit controlled burial dolomitization of the Devonian west-central Alberta Deep Basin. *Bulletin of Canadian Petroleum Geology*, 53(2), 101-129.

Grigoli, F., Cesca, S., Priolo, E., Rinaldi, A. P., Clinton, J. F., Stabile, T. A., ... & Dahm, T. (2017). Current challenges in monitoring, discrimination, and management of induced seismicity related to underground industrial activities: A European perspective. *Reviews of Geophysics*.

Grigoli, F., Cesca, S., Rinaldi, A. P., Manconi, A., López-Comino, J. A., Clinton, J. F., ... & Wiemer, S. (2018). The November 2017 Mw 5.5 Pohang earthquake: A possible case of induced seismicity in South Korea. *Science*, eaat2010.

Gu, Y. J., Okeler, A., Shen, L., & Contenti, S. (2011). The Canadian Rockies and Alberta Network (CRANE): New constraints on the Rockies and western Canada sedimentary basin. *Seismological Research Letters*, 82(4), 575-588.

Gu, Y. J. & L. Shen (2015). Noise correlation tomography of Southwest Western Canada Sedimentary Basin, *Geophys. J. Int.*, 202(1), 142–162, doi:10.1093/gji/ggv100

Guilhem, A., Hutchings, L., Dreger, D. S., & Johnson, L. R. (2014). Moment tensor inversions of $M \sim 3$ earthquakes in the Geysers geothermal fields, California. *J. Geophys. Res. Solid Earth*, 119(3), 2121-2137.

Guglielmi, Y., Cappa, F., Avouac, J. P., Henry, P., & Elsworth, D. (2015). Seismicity triggered by fluid injection–induced aseismic slip. *Science*, 348(6240), 1224-1226.

- Hanks, T. C. & H. Kanamori (1979). A moment magnitude scale, *J. Geophys. Res.*, 84(B5), 2348–2350, doi:10.1029/JB084iB05p02348.
- Hanmer, S., Williams, M., & Kopf, C. (1995). Striding-Athabasca mylonite zone: Implications for the Archean and Early Proterozoic tectonics of the western Canadian Shield, *Can. J. Earth Sci.*, 32(2), 178–196.
- Häring, M. O., Schanz, U., Ladner, F., & Dyer, B. C. (2008). Characterisation of the Basel 1 enhanced geothermal system, *Geothermics*, 37(5), 469–495, doi:10.1016/j.geothermics.2008.06.002.
- Haug, K. M., Dongas, J. M., & Warren, J. (2013). A review of the potential correlation between low-magnitude earthquakes and oil and gas industry activity in Alberta, *Alberta Energy Regulator, AER/AGS Open File Report*, 2013-16, 43 p.
- Heidbach, O., Rajabi, M., Reiter, K., Ziegler, M., & Team, W. S. M. *World Stress Map Database Release 2016*. Henry, C., Woodhouse, J., & Das, S. (2002). Stability of earthquake moment tensor inversions: Effect of the double-couple constraint, *Tectonophysics*, 356(1), 115–124, doi:10.1016/S0040-1951(02)00379-7.
- Herrmann, R. B. & Nuttli, O. W. (1982). Magnitude: The relation of ML to mbLg, *Bull. Seismol. Soc. Am.*, 72(2), 389–397.
- Hincks, T., Aspinall, W., Cooke, R., & Gernon, T. (2018). Oklahoma's induced seismicity strongly linked to wastewater injection depth. *Science*, 359(6381), 1251-1255.
- Hoffman, P. F. (1988). United plates of America, the birth of a craton-Early Proterozoic assembly and growth of Laurentia, *Annu. Rev. Earth Planet. Sci.*, 16, 543–603.
- Holtzman, B. K., Paté, A., Paisley, J., Waldhauser, F., & Repetto, D. (2018). Machine learning reveals cyclic changes in seismic source spectra in Geysers geothermal field. *Science advances*, 4(5), eaao2929.

- Honda, H. (1962). Earthquake mechanism and seismic waves. *Journal of Physics of the Earth*, 10(2), 1-97.
- Hope, J., Eaton, D. W., & Ross, G. M. (1999). Lithoprobe seismic transect of the Alberta Basin: compilation and overview. *Bulletin of Canadian Petroleum Geology*, 47(4), 331-345.
- Huang, Y., Ellsworth, W. L., & Beroza, G. C. (2017). Stress drops of induced and tectonic earthquakes in the central United States are indistinguishable. *Science advances*, 3(8), e1700772.
- Hudson, J. A., Pearce, R. G., & Rogers, R. M. (1989). Source type plot for inversion of the moment tensor. *J. Geophys. Res. Solid Earth*, 94(B1), 765-774.
- Ichinose, G. A., Smith, K. D., & Anderson, J. G. (1998). Moment tensor solutions of the 1994 to 1996 double spring flat, Nevada, earthquake sequence and implications for local tectonic models, *Bull. Seismol. Soc. Am.*, 88(6), 1363–1378
- Jones, A. G. (2002), Magnetotelluric and teleseismic study across the Snowbird Tectonic Zone, Canadian Shield: A Neoproterozoic mantle suture?, *Geophys. Res. Lett.*, 29(17), 1829, doi:10.1029/2002GL015359.
- Jost, M. U. & Herrmann, R. B. (1989). A student's guide to and review of moment tensors. *Seismological Research Letters*, 60(2), 37-57.
- Johnson, K. L., Hayes, G. P., Herrmann, R. B., Benz, H. M., McNamara, D. E., & Bergman, E. (2016). RMT focal plane sensitivity to seismic network geometry and faulting style. *Geophysical Journal International*, 206(1), 525-556.
- Julian, B. R., Miller, A. D., & Foulger, G. (1998). Non-double-couple earthquakes 1. *Theory, Rev. Geophys.*, 36(4), 525–549.
- Kao, H., Shan, S. J., Bent, A., Woodgold, C., Rogers, G., Cassidy, J. F., & Ristau, J. (2012). Regional centroid-moment-tensor analysis for earthquakes in Canada and adjacent regions: An update. *Seismological Research Letters*, 83(3), 505-515.

- Kawakatsu, H. (1991). Enigma of earthquakes at ridge-transform-fault plate boundaries distribution of non-double couple parameter of Harvard CMT solutions, *Geophys. Res. Lett.*, 18(6), 1103–1106.
- Karimi, S., Baturan, D., & Yenier, E. (2018). Five key lessons gained from induced seismicity monitoring in western Canada. *The Leading Edge*, 37(2), 107a1-107a8.
- Kennett, B., & Engdahl, E. (1991). Travel times for global earthquake location and phase identification, *Geophys. J. Int.*, 105(2), 429–465.
- Kim, W.-Y. (2013). Induced seismicity associated with fluid injection into a deep well in Youngstown, Ohio, *J. Geophys. Res. Solid Earth*, 118, 3506–3518, doi:10.1002/jgrb.50247
- Kim, Y., Liu, Q., & Tromp, J. (2011). Adjoint centroid-moment tensor inversions. *Geophys. J. Int.*, 186(1), pp.264-278.
- Kim, K. H., Ree, J. H., Kim, Y., Kim, S., Kang, S. Y., & Seo, W. (2018). Assessing whether the 2017 Mw 5.4 Pohang earthquake in South Korea was an induced event. *Science*, eaat6081.
- Kuge, K. & Kawakatsu, H. (1990). Analysis of a deep “non-double-couple” earthquake using very broadband data, *Geophys. Res. Lett.*, 17(3), 227–230
- Langenbruch, C., & Zoback, M. D. (2016). How will induced seismicity in Oklahoma respond to decreased saltwater injection rates?. *Science advances*, 2(11), e1601542.
- Lei, X., Ma, S., Chen, W., Pang, C., Zeng, J., & Jiang, B. (2013). A detailed view of the injection-induced seismicity in a natural gas reservoir in Zigong, southwestern Sichuan Basin, China. *J. Geophys. Res. Solid Earth*, 118(8), 4296-4311.
- Lei, X., Huang, D., Su, J., Jiang, G., Wang, X., Wang, H., ... & Fu, H. (2017). Fault reactivation and earthquakes with magnitudes of up to Mw4.7 induced by shale-gas hydraulic fracturing in Sichuan Basin, China. *Scientific Reports*, 7.

Lewry, J., Hajnal, Z., Green, A., Lucas, S., White, D., Stauffer, M., Ashton, K., Weber, W., & Clowes, R. (1994). Structure of a Paleoproterozoic continent-continent collision zone: A LITHOPROBE seismic reflection profile across the Trans-Hudson Orogen, Canada, *Tectonophysics*, 232(1), 143–160.

Lele, S. P., Tyrrell, T., & Dasari, G. R. (2017, August). Geomechanical Analysis of Fault Reactivation Due to Hydraulic Fracturing. In *51st US Rock Mechanics/Geomechanics Symposium*. American Rock Mechanics Association.

Majorowicz, J., Chan, J., Crowell, J., Gosnold, W., Heaman, L. M., Kück, J., Nieuwenhuis, G., Schmitt, D.R., Unsworth, M., Walsh, N., & Weides, S. (2014). The first deep heat flow determination in crystalline basement rocks beneath the Western Canadian Sedimentary Basin. *Geophys. J. Int.*, 197(2), 731-747. doi: 10.1093/gji/ggu065.

Martínez-Garzón, P., Kwiatek, G., Bohnhoff, M., & Dresen, G. (2017). Volumetric components in the earthquake source related to fluid injection and stress state. *Geophysical Research Letters*, 44(2), 800-809.

Maxwell, S., Chorney, D., Smith, M., & Mack, M. (2016, January). Microseismic geomechanical interpretation of asymmetric hydraulic fractures. In *2016 SEG International Exposition and Annual Meeting*. Society of Exploration Geophysicists.

McGarr, A. (2014). Maximum magnitude earthquakes induced by fluid injection. *Journal of Geophysical Research: Solid Earth*, 119(2), 1008-1019.

McGarr, A. & Barbour, A. J. (2017). Wastewater disposal and the earthquake sequences during 2016 near Fairview, Pawnee, and Cushing, Oklahoma. *Geophysical Research Letters*, 44(18), 9330-9336.

McGarr, A., Bekins, B., Burkardt, N., Dewey, J., Earle, P., Ellsworth, W., ... & Rubinstein, J. (2015). Coping with earthquakes induced by fluid injection. *Science*, 347(6224), 830-831.

- McNamara, D.E., Benz, H.M., Herrmann, R.B., Bergman, E.A., Earle, P., Holland, A., Baldwin, R., & Gassner, A. (2015). Earthquake hypocenters and focal mechanisms in central Oklahoma reveal a complex system of reactivated subsurface strike-slip faulting *Geophys. Res. Lett.*, 42(8), pp.2742-2749.
- Mignan, A., Broccardo, M., Wiemer, S., & Giardini, D. (2017). Induced seismicity closed-form traffic light system for actuarial decision-making during deep fluid injections. *Scientific Reports*, 7(1), 13607.
- Miller, A. D., Foulger, G. R., & Julian, B. R. (1998). Non-double-couple earthquakes 2. Observations. *Reviews of Geophysics*, 36(4), 551-568.
- Minson, S. E., Dreger, D. S., Bürgmann, R., Kanamori, H., & Larson, K. M. (2007). Seismically and geodetically determined nondouble-couple source mechanisms from the 2000 Miyakejima volcanic earthquake swarm. *J. Geophys. Res. Solid Earth*, 112(B10).
- Minson, S. E., & Dreger, D. S. (2008). Stable inversions for complete moment tensors, *Geophys. J. Int.*, 174(2), 585–592, doi:10.1111/j.1365-246X.2008.03797.x.
- Monger, J., & Price, R. (2002). The Canadian Cordillera: geology and tectonic evolution. *CSEG Recorder*, 27(2), 17-36.
- Mountjoy, E.W., Machel, H.G., Green, D., Duggan, J., & Williams-Jones, A.E. (1999). Devonian matrix dolomites and deep burial carbonate cements: a comparison between the Rimbey-Meadowbrook reef trend and the deep basin of west-central Alberta. *Bulletin of Canadian Petroleum Geology*, 47(4), 487-509.
- Munafò, I., Malagnini, L., & Chiaraluce, L. (2016). On the relationship between M_w and M_L for small earthquakes. *Bulletin of the Seismological Society of America*, 106(5), 2402-2408.
- Nuttli, O. W. (1973). Seismic wave attenuation and magnitude relations for eastern North America, *J. Geophys. Res.*, 78(5), 876–885.

Oilweek Magazine (2013). Delving into the Duvernay. [Available at <http://oilweek1.rssing.com/browser.php?indx=10975088&item=82.>]

Ong, O. N., Schmitt, D. R., Kofman, R. S., & Haug, K. (2016). Static and dynamic pressure sensitivity anisotropy of a calcareous shale. *Geophysical Prospecting*, 64(4), 875-897.

Pakzad, M., Moradi, A., Afra, M., & Hosseini, H. (2018). Resolvability of moment tensors in Iran. *Geophysical Journal International*, 214(1), 133-147.

Pasyanos, M. E., Dreger, D. S., & Romanowicz, B. (1996). Toward real-time estimation of regional moment tensors, *Bull. Seismol. Soc. Am.*, 86(5), 1255–1269.

Petersen, M. D., Mueller, C. S., Moschetti, M. P., Hoover, S. M., Shumway, A. M., McNamara, D. E., ... & Rubinstein, J. L. (2017). 2017 one-year seismic-hazard forecast for the Central and Eastern United States from induced and natural earthquakes. *Seismological Research Letters*, 88(3), 772-783.

Pilkington, M., Miles, W.F., Ross, G.M., & Roest, W.R. (2000). Potential-field signatures of buried Precambrian basement in the Western Canada Sedimentary Basin. *Can. J. Earth Sci.*, 37(11), 1453-1471. doi: 10.1139/e00-020.

Rebollar, C., Kanasevich, E., & Nyland, E. (1982). Source parameters from shallow events in the Rocky Mountain House earthquake swarm, *Can. J. Earth Sci.*, 19(5), 907–918

Reiter, K., Heidbach, O., Schmitt, D., Haug, K., Ziegler, M., & Moeck, I. (2014). A revised crustal stress orientation database for Canada. *Tectonophysics*, 636, 111-124.

Richter, C. F. (1935). An instrumental earthquake magnitude scale. *Bulletin of the Seismological Society of America*, 25(1), 1-32.

Ristau, J., Rogers, G.C., & Cassidy, J.F. (2007). Stress in western Canada from regional moment tensor analysis. *Can. J. Earth Sci.*, 44(2), 127-148. doi: 10.1139/e06-057.

Rivard, C., Lavoie, D., Lefebvre, R., Séjourné, S., Lamontagne, C., & Duchesne, M. (2014). An overview of Canadian shale gas production and environmental concerns. *International Journal of Coal Geology*, 126, 64-76.

Rokosh, C. D., Anderson, S. D., Beaton, A. P., Berhane, M., & Pawlowicz, J. (2010). Geochemical and geological characterization of the Duvernay and Muskwa Formation in Alberta, paper presented at Canadian Unconventional Resources and International Petroleum Conference, Calgary, Alberta, Canada, 19–21 Oct., Soc. of Petrol. Eng., doi:10.2118/137799-MS

Rokosh, C. D., Lyster, S., Anderson, S. D. A., Beaton, A. P., Berhane, H., Brazzoni, T., Chen, D., Cheng, Y., Mack, T., Paná, C., & Pawlowicz, J. G. (2012). Summary of Alberta's Shale-and Siltstone-Hosted Hydrocarbons. *ERCB/AGS Open File Report*, 6.

Ross, A., Foulger, G. R., & Julian, B. R. (1996). Non-double-couple earthquake mechanisms at The Geysers geothermal area, California. *Geophysical Research Letters*, 23(8), 877-880.

Ross, G. M. & Eaton, D. W. (1999). Basement reactivation in the Alberta Basin: Observational constraints and mechanical rationale. *Bulletin of Canadian Petroleum Geology*, 47(4), 391-411.

Ross, G. M., Eaton, D. W., Boerner, D. E., & Miles, W. (2000). Tectonic entrapment and its role in the evolution of continental lithosphere: An example from the Precambrian of western Canada, *Tectonics*, 19(1), 116–134.

Ross, Z. E., Ben-Zion, Y., White, M. C., & Vernon, F. L. (2016). Analysis of earthquake body wave spectra for potency and magnitude values: implications for magnitude scaling relations. *Geophysical Journal International*, 207, 1158-1164.

Rubinstein, J. L. & Mahani, A. B. (2015). Myths and facts on wastewater injection, hydraulic fracturing, enhanced oil recovery, and induced seismicity. *Seismol. Res. Lett.*

Rubinstein, J. L., Ellsworth W. L., McGarr, A., & Benz H. M. (2014). The 2001-present induced earthquake sequence in the Raton Basin of northern New Mexico and southern Colorado, *Bull. Seismol. Soc. Am.* 104, no. 5, 2162–2181, doi: 10.1785/0120140009.

- Saikia, C.K. (1994). Modified frequency-wavenumber algorithm for regional seismograms using Filon's quadrature: Modelling of Lg waves in eastern North America, *Geophys. J. Int.*, 118(1), 142–158.
- Saruwatari, K., Ji, S., Long, C., & Salisbury, M. H. (2001). Seismic anisotropy of mantle xenoliths and constraints on upper mantle structure beneath the southern Canadian Cordillera. *Tectonophysics*, 339(3), 403-426.
- Shearer, P. M. (2009). Introduction to seismology. *Cambridge University Press*.
- Schmitt, D. R. (2014). Basic geomechanics for induced seismicity: A tutorial. *CSEG RECORDER (Nov 2014)*, 39(9).
- Schoenball, M., Walsh, F. R., Weingarten, M., & Ellsworth, W. L. (2018). How faults wake up: The Guthrie-Langston, Oklahoma earthquakes. *The Leading Edge*, 37(2), 100-106.
- Shuler, A., Ekström, G., & Nettles, M. (2013). Physical mechanisms for vertical-CLVD earthquakes at active volcanoes. *J. Geophys. Res. Solid Earth*, 118(4), 1569-1586.
- Schultz, R., Stern, V., & Gu Y.J. (2014). An investigation of seismicity clustered near the Cordell Field, west-central Alberta, and its relation to a nearby disposal well, *J. Geophys. Res. Solid Earth*, 119, 3410–3423, doi:10.1002/2013JB010836.
- Schultz, R. & Stern, V. (2015). The Regional Alberta Observatory for Earthquake Studies Network (RAVEN). *CSEG Recorder*, 40(8), 34-37.
- Schultz, R., Stern, V., Gu, Y. J., & Eaton, D. (2015a). Detection threshold and location resolution of the Alberta Geological Survey earthquake catalogue. *Seismological Research Letters*, 86(2A), 385-397.
- Schultz, R., Stern, V., Novakovic, M., Atkinson, G., & Gu, Y. J. (2015b). Hydraulic fracturing and the Crooked Lake Sequences: Insights gleaned from regional seismic networks. *Geophysical Research Letters*, 42(8), 2750-2758.

Schultz, R., Mei, S., Pană, D., Stern, V., Gu, Y.J., Kim, A., and Eaton, D. (2015c). The Cardston earthquake swarm and hydraulic fracturing of the Exshaw Formation (Alberta Bakken play), *Bull. Seismol. Soc. Am.*, 105(6), 2871–2884, doi:10.1785/0120150131.

Schultz, R., Corlett, H., Haug, K., Kocon, K., MacCormack, K., Stern, V., & Shipman, T. (2016). Linking fossil reefs with earthquakes: Geologic insight to where induced seismicity occurs in Alberta. *Geophys. Res. Lett.*, 43, 2534–2542, doi:10.1002/2015GL067514.

Schultz, R., Wang, R., Gu, Y. J., Haug, K., & Atkinson, G. (2017). A seismological overview of the induced earthquakes in the Duvernay play near Fox Creek, Alberta. *J. Geophys. Res. Solid Earth*, 122(1), 492-505.

Schultz, R., Atkinson, G., Eaton, D. W., Gu, Y. J., & Kao, H. (2018). Hydraulic fracturing volume is associated with induced earthquake productivity in the Duvernay play. *Science*, 359(6373), 304-308.

Schultz, R., & Telesca, L. (2018). The Cross-Correlation and Reshuffling Tests in Discerning Induced Seismicity. *Pure and Applied Geophysics*, 1-7.

Šílený, J. & Milev, A. (2008). Source mechanism of mining induced seismic events—resolution of double couple and non double couple models. *Tectonophysics*, 456(1), 3-15.

Šílený, J., Hill, D.P., Eisner, L., & Cornet, F.H. (2009). Non–double-couple mechanisms of microearthquakes induced by hydraulic fracturing, *J. Geophys. Res. Solid Earth*, 114, B08307, doi:10.1029/2008JB005987.

Skoumal, R. J., Brudzinski, M. R., & Currie, B. S. (2015a). Distinguishing induced seismicity from natural seismicity in Ohio: Demonstrating the utility of waveform template matching. *J. Geophys. Res. Solid Earth*, 120(9), 6284-6296.

Skoumal, R.J., Brudzinski, M.R., & Currie, B.S. (2015b). Earthquakes induced by hydraulic fracturing in Poland Township, Ohio. *Bull. Seismol. Soc. Am.*, 105(1), pp.189-197.

Smith, W. & Wessel, P. (1990). Gridding with continuous curvature splines in tension, *Geophysics*, 55(3), 293–305.

Stern, V., Schultz, R., Shen, L., Gu, Y., & Eaton, D. (2013). Alberta earthquake catalogue, version 1.0: September 2006 through December 2010, *AER/AGS Open File Rep.* 2013-15, vol. 15, 36 pp., Alberta Geol. Surv., Alberta, Canada. [Available at http://www.ags.gov.ab.ca/publications/ofr/PDF/ofr_2013_15.pdf.]

Switzer, S.B., Holland, W.G., Christie, D.S., Graf, G.C., Hedinger, A.S., McAuley, R.J., Wierzbicki, R.A., & Packard, J.J. (1994). Devonian Woodbend-Winterburn strata of the Western Canada Sedimentary Basin. *Geological Atlas of the Western Canada Sedimentary Basin: Canadian Society of Petroleum Geologists and Alberta Research Council*, pp.165-202.

Sylvester, A. G. (1988). Strike-slip faults. *Geological Society of America Bulletin*, 100(11), 1666-1703.

Tang, C. C., Zhu, L., & Huang, R. (2016). Empirical M_w -ML, mb, and M_s Conversions in Western China. *Bulletin of the Seismological Society of America*, 106(6), 2614-2623.

Tao, W., Masterlark, T., Shen, Z. K., & Ronchin, E. (2015). Impoundment of the Zipingpu reservoir and triggering of the 2008 Mw 7.9 Wenchuan earthquake, China. *J. Geophys. Res. Solid Earth*, 120(10), 7033-7047.

Tape, W., & Tape, C. (2012). A geometric comparison of source-type plots for moment tensors. *Geophysical Journal International*, 190(1), 499-510.

Telesca, L. (2010). Analysis of the cross-correlation between seismicity and water level in the Koyna area of India. *Bull. Seismol. Soc. Am.*, 100(5A), 2317-2321.

Udias, A., Madariaga, R., & Buforn, E. (2014). *Chapter 6: Determination of point source mechanisms, Source Mechanisms of Earthquakes: Theory and Practice*. Cambridge University Press.

van der Baan, M. & Calixto, F. J. (2017). Human-induced seismicity and large-scale hydrocarbon production in the USA and Canada. *Geochemistry, Geophysics, Geosystems*.

Vavryčuk, V., Bohnhoff, M., Jechumtálová, Z., Kolář, P., & Šílený, J. (2008). Non-double-couple mechanisms of microearthquakes induced during the 2000 injection experiment at the KTB site, Germany: A result of tensile faulting or anisotropy of a rock?, *Tectonophysics*, 456(1), 74-93.

Vavryčuk, V. (2015). Moment tensor decompositions revisited. *Journal of Seismology*, 19(1), 231-252.

Waldhauser, F., & Ellsworth, W. L. (2000). A double-difference earthquake location algorithm: Method and application to the northern Hayward fault, California. *Bulletin of the Seismological Society of America*, 90(6), 1353-1368.

Wang, B., Harrington, R. M., Liu, Y., Yu, H., Carey, A., & Elst, N. J. (2015). Isolated cases of remote dynamic triggering in Canada detected using cataloged earthquakes combined with a matched-filter approach. *Geophysical Research Letters*, 42(13), 5187-5196.

Wang, R., Gu, Y.J., Schultz, R., Kim, A., & Atkinson, G. (2016). Source analysis of a potential hydraulic-fracturing-induced earthquake near Fox Creek, Alberta, *Geophys. Res. Lett.*, 43, doi:10.1002/2015GL066917.

Wang, R., Gu, Y. J., Schultz, R., Zhang, M., & Kim, A. (2017a). Source characteristics and geological implications of the January 2016 induced earthquake swarm near Crooked Lake, Alberta. *Geophysical Journal International*, 210(2), 979-988.

Wang, R., Gu, Y. J., & Zhang, M. (2017b), Hydraulic fracturing induced seismicity in western Canada: insights from focal mechanism and swarm analysis, 2017 Workshop: Microseismic Technologies and Applications, Hefei, China, 4-6 June 2017: pp. 42-45.

Wang, R., Gu, Y. J., Schultz, R., & Chen, Y. (2018). Faults and the non-double-couple components of induced earthquake, submitted to *Geophys. Res. Lett.*

- Welford, J. K. & Clowes R. M. (2006). Three-dimensional seismic reflection investigation of the upper crustal Winagami sill complex of northwestern Alberta, Canada, *Geophys. J. Int.*, 166(1), 155–169, doi:10.1111/j.1365-246X.2006.02805.x.
- Wells, D. L. & Coppersmith, K. J. (1994). New empirical relationships among magnitude, rupture length, rupture width, rupture area, and surface displacement, *Bull. Seismol. Soc. Am.*, 84(4), 974–1002.
- Wendte, J. & Uyeno, T. (2005). Sequence stratigraphy and evolution of Middle to Upper Devonian Beaverhill Lake strata, south-central Alberta. *Bulletin of Canadian Petroleum Geology*, 53(3), 250
- Wessel, P., Smith, W.H.F., Scharroo, R., Luis, J.F., & Wobbe, F. (2013). Generic Mapping Tools: Improved version released, *EOS Trans. AGU*, 94, 409-410, 2013.
- Wetmiller, R. J. (1986). Earthquakes near Rocky Mountain House, Alberta, and their relationship to gas production facilities. *Can. J. Earth Sci.*, 23(2), 172-181.
- Wilson, M.P., Worrall, F., Davies, R.J., & S. Almond. (2018). Fracking: How far from faults? *Geomech. Geophys. Geo-energ. Geo-resour.* <https://doi.org/10.1007/s40948-018-0081-y>
- Wilson, M. P., Foulger, G. R., Gluyas, J. G., Davies, R. J., & Julian, B. R. (2017). HiQuake: The Human-Induced Earthquake Database. *Seismological Research Letters*, 88(6), 1560-1565.
- Yenier, E. & Atkinson, G. M. (2015). Regionally adjustable generic ground-motion prediction equation based on equivalent point-source simulations: Application to central and eastern North America, *Bull. Seismol. Soc. Am.*, 105(4), 1989–2009, doi:10.1785/0120140332.
- Zang, A., Oye, V., Jousset, P., Deichmann, N., Gritto, R., McGarr, A., Majer, E., & Bruhn, D. (2014), Analysis of induced seismicity in geothermal reservoirs—An overview, *Geothermics*, 52, 6–21, doi:10.1016/j.geothermics.2014.06.005
- Zelt, C. & Ellis, R. (1990). Crust and upper mantle Q from seismic refraction data: Peace River region, *Can. J. Earth Sci.*, 27(8), 1040–1047.

Zhao, P., Kühn, D., Oye, V., & Cesca, S. (2014). Evidence for tensile faulting deduced from full waveform moment tensor inversion during the stimulation of the Base enhanced geothermal system. *Geothermics*, 52, 74-83.

Zhang, H., Eaton, D. W., Li, G., Liu, Y., & Harrington, R.M. (2016). Discriminating induced seismicity from natural earthquakes using moment tensors and source spectra. *J. Geophys. Res. Solid Earth*, 121, 972-993, doi: 10.1002/2015JB012603.

Zhang, M. & Wen, L. (2015a). An effective method for small event detection: match and locate (M&L). *Geophys. J. Int.*, 200(3), pp. 1523-1537, doi: 10.1093/gji/ggu466

Zhang, M. & Wen, L. (2015b). Earthquake characteristics before eruptions of Japan's Ontake volcano in 2007 and 2014. *Geophys. Res. Lett.*, 42(17), 6982-6988, doi: 10.1002/2015GL065165.

Zhang, Y., Person, M., Rupp, J., Ellett, K., Celia, M. A., Gable, C. W., ... & Dewers, T. (2013). Hydrogeologic controls on induced seismicity in crystalline basement rocks due to fluid injection into basal reservoirs. *Groundwater*, 51(4), 525-538.

Zhu, L., & Ben-Zion, Y. (2013). Parametrization of general seismic potency and moment tensors for source inversion of seismic waveform data. *Geophysical Journal International*, 194(2), 839-843.

Zhu, L., Helmberger, D. V., Saikia, C. K., & Woods, B. B. (1997). Regional waveform calibration in the Pamir-Hindu Kush region. *Journal of Geophysical Research: Solid Earth*, 102(B10), 22799-22813.

A Appendix

A1. Input parameter and velocity model set up for moment tensor inversion

The locations of the induced earthquakes are selected from multiple reporting agencies: Earthquake Canada, Nanometrics Athena, and the Alberta Geological Survey (Table A1). For induced events, the hypocenters are further refined by relocation, and their focal depths are verified with known injection depths. In addition, I refine the sedimentary velocity model for various events and reduce the effect of heterogeneity and anisotropy by allowing additional shifts for individual components and frequencies (Figure A26-27 and Dataset S1; also see Wang *et al.* 2017a for details).

I find that even though the DC components are highly stable, the non-DC component trade-offs with event depth as well as the structure of sedimentary layers (Figure A24). The velocity model factor may explain the different amounts of non-DC resolved by this and Zhang *et al.* (2016), which found significantly larger non-DC from eight suspected Mw~4 induced events than an Mw5.1 tectonic earthquake. Given model uncertainties and limited resolution, Fischer & Guest (2011) justified the existence of significant non-DC, especially at shallow depths and/or over-pressured reservoirs. In our case, it is encouraging that the highly consistent events are all shallow earthquakes within the over-pressured Duvernay Formation. A series of synthetic tests were conducted to evaluate the effect of noise and station distribution. I conclude that the non-DC components have been constrained reliably using the available data and structural model in this study.

A1.1 Hypocenter locations and synthetic tests setup

My hypocenter locations of the earthquakes are well-determined for two reasons. First, my source locations are selected from values reviewed and provided by multiple agencies and overlap with the location of corresponding hydraulic-fracturing wells (Schultz *et al.* 2017). Second, the source

mislocation has less effect on the moment tensor inversion than mismodelling (Šílený *et al.* 2009). Based on these considerations, I believe that the selected source location is constrained to errors less than 1 km and has a negligible effect on my moment tensor inversion results.

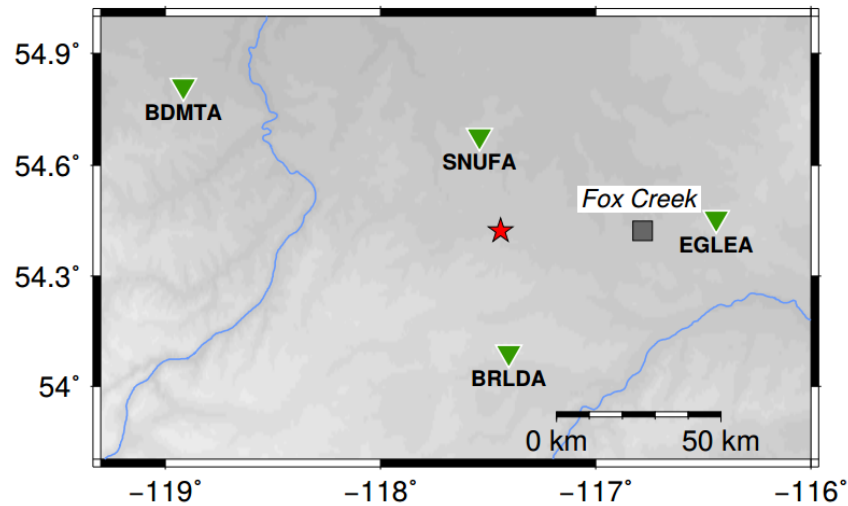


Figure A.1: Station distribution for the synthetic tests. The red star denotes the location of earthquake hypocenter (depth = 4 km).

With the confidence in the source location and depth, I believe four three-component stations (Figure A1) are sufficient to resolve the non-DC components. I have conducted multiple synthetic tests to examine the effects of two key factors: 1) velocity model (section A1.2) and 2) SNR (section A1.3). First, I computed synthetic seismograms using a hypothetical source that combines two double-couples (Table A1). Then I inverted and decomposed the moment tensors in all cases. The inversion metric is also same as my real-data processing: the data, Green's function, and noise are fitted in two frequency ranges: 0.05-0.1 Hz and 0.08-0.4 Hz. The lower frequency range is processed with a weight of 5 to ensure similar contribution during the inversion procedure. For near source stations, both frequency ranges contain all phases (body and surface waves) while only first arrivals (mainly body waves) are fitted for recordings from far source stations (> 100 km). The variance reduction (VR) and decomposed results are summarized in Table A2 and Table A3.

Results of all waveform fitting and associated parameters are presented in Figures A5-22. Finally, the waveform matching of real data and summaries of my findings are presented in section A1.4.

Input	strike	rake	dip	M0	Mw
				(dyne-cm)	
Major DC	183.2	171.7	87.7	4.48e20	3.06
Minor DC	326.5	-78.9	41.2	4.48e19	2.40
Isotropic (ISO)	-			0	0.00

Table A.1: Input moment tensor for the synthetic test

This super-imposed source produces the following full moment tensor:

$$\mathbf{M}_{dc} = \begin{bmatrix} 0.6787 & -4.1770 & -0.2921 \\ -4.1770 & -0.2925 & 0.6216 \\ -0.2921 & 0.6216 & -0.3862 \end{bmatrix} \times 1e^{20}$$

Note that moment magnitude of \mathbf{M}_{dc} is 3.1 and the trace of \mathbf{M}_{dc} is zero, indicating no ISO component. A noise free synthetic test was conducted to ensure the output is equivalent to my input (Figure A2), where the fault angles for the major and minor DCs correspond to the input moment tensor (Table A1).

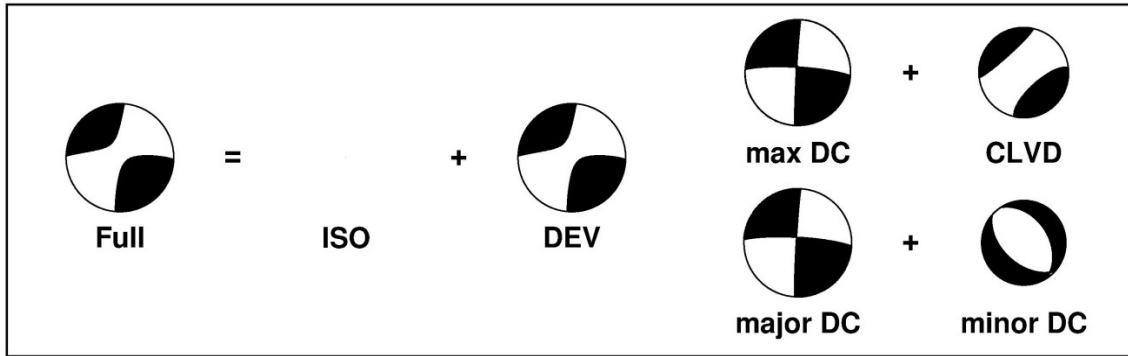


Figure A.2: Decomposition of zero-noise recovered moment tensor. The isotropic (ISO) part is zero (0%), and the deviatoric part can be decomposed into 1) DC (80%) and CLVD (20%) or 2) major ($M=3.1$) and minor ($M=2.4$) DCs.

A1.2 Velocity model test

My velocity model test is conducted for five cases (Table A2) based on reference (input) weights of DC/CLVD/ISO = 80/20/0.

Velocity change	VR	Decomp (DC/CLVD/ISO)	Figures
20% decrease	30.9	79/14/7	S3 & S5
10% decrease	83.4	90/9/1	S3 & S6
10% increase	85.4	78/19/3	S3 & S7
20% increase	48.0	87/9/4	S3 & S8
<10% random	95.1	83/16/2	S4 & S9

Table A.2: Summary of velocity model tests

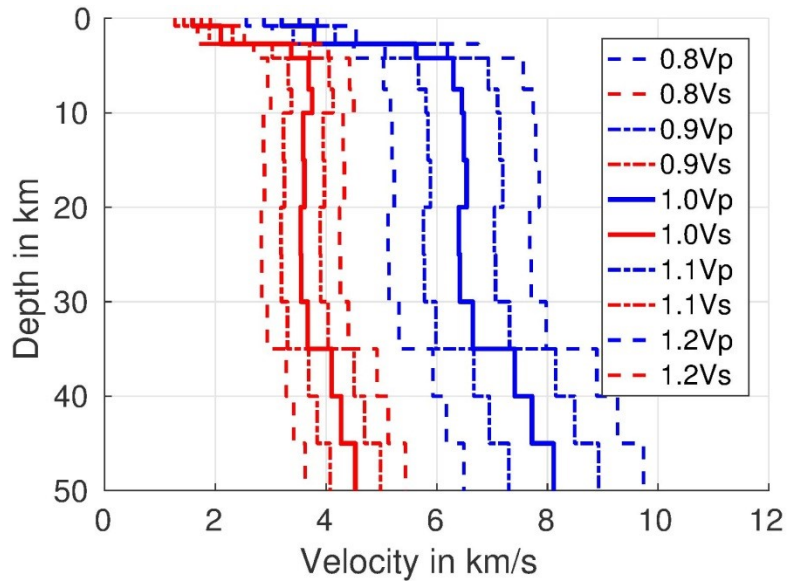


Figure A.3: Outcomes of the change on my preferred 14-layer model (solid lines) for $\pm 10\%$ (dot-dashed lines) and $\pm 20\%$ (dashed lines) perturbations to all layers.

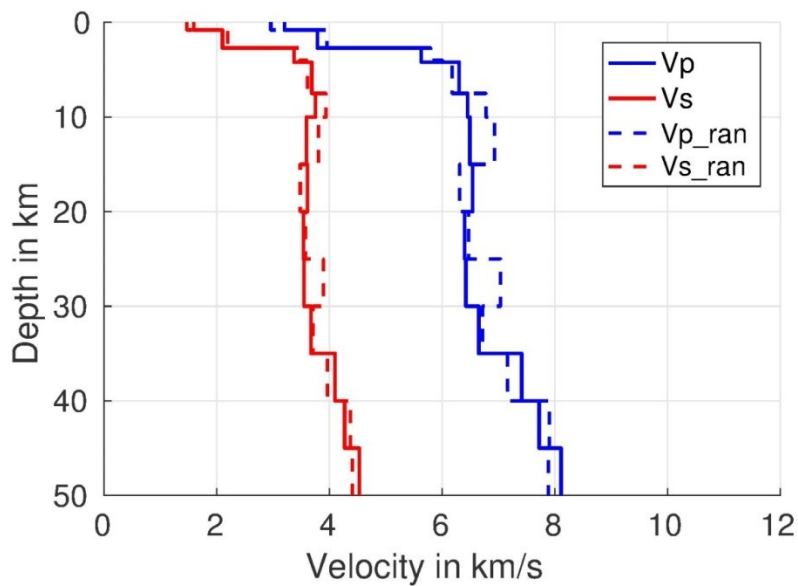


Figure A.4: Random perturbation (up to $\pm 10\%$) on the velocity model (dashed lines) relative to the preferred velocity model is shown in solid lines.

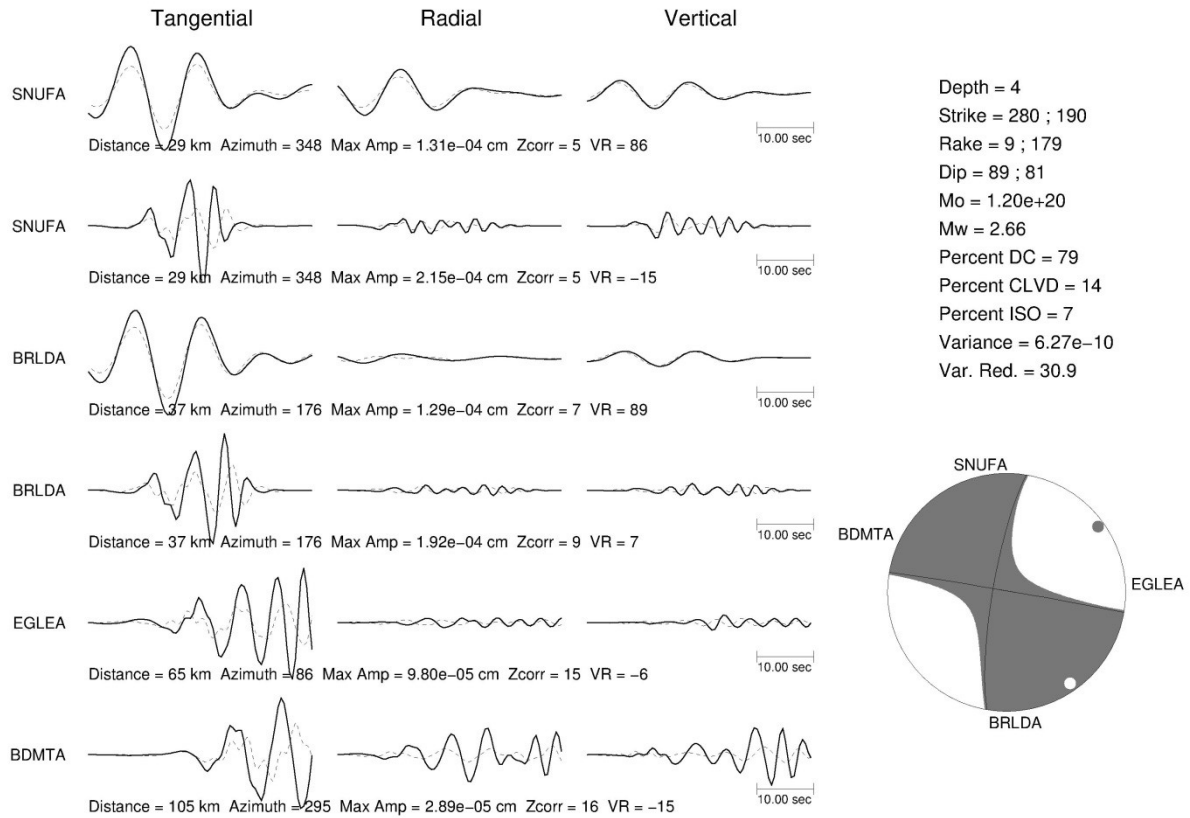


Figure A.5: Waveform fitting using synthetic data and model with decreased velocity by 20%. The Zcorr are relative shifts and are all negative in this case. The solid lines show the input (simulated) waveforms and the grey dashed lines show the outcomes of the moment tensor inversion. The definitions are consistent for subsequent plots of A6-9.

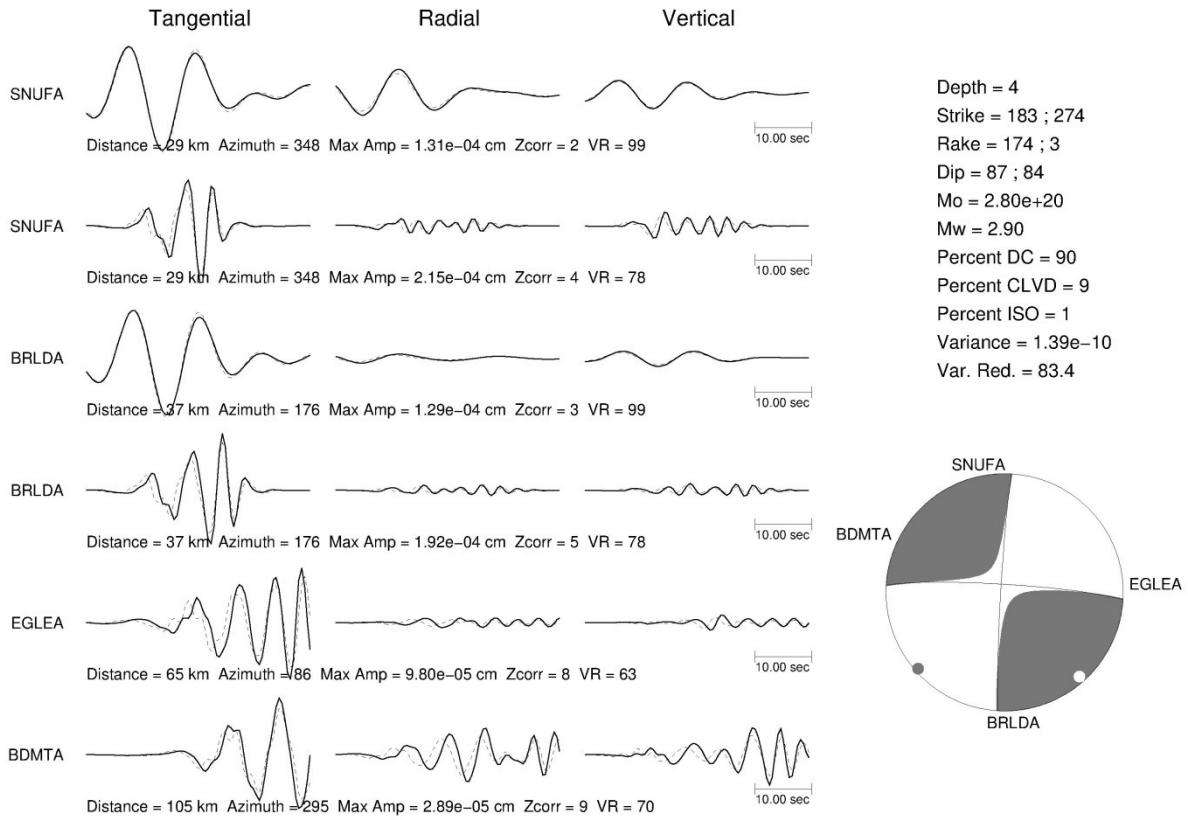


Figure A.6: Waveform fitting using synthetic data and model with decreased velocity by 10%. The Zcorr are relative shifts and are all negative in this case.

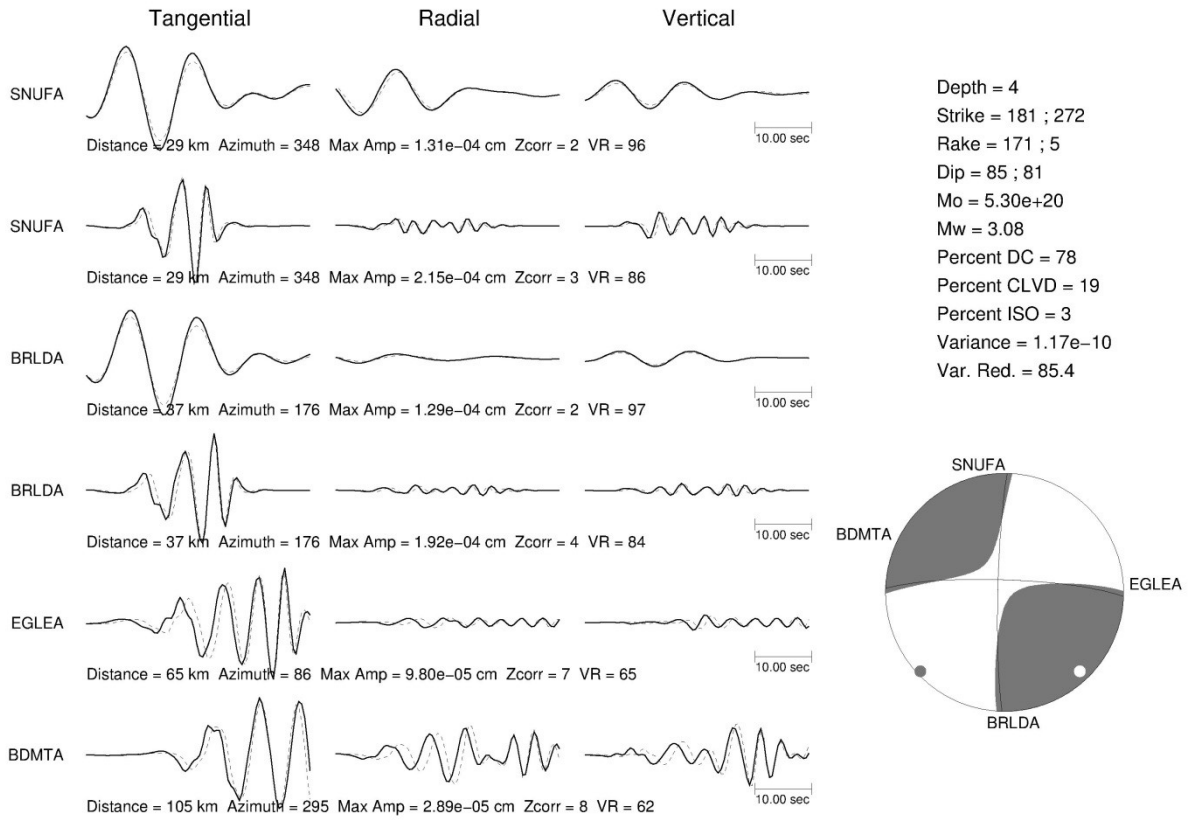


Figure A.7: Waveform fitting using synthetic data and model with increased velocity by 10%. The Zcorr are relative shifts and are all positive in this case.

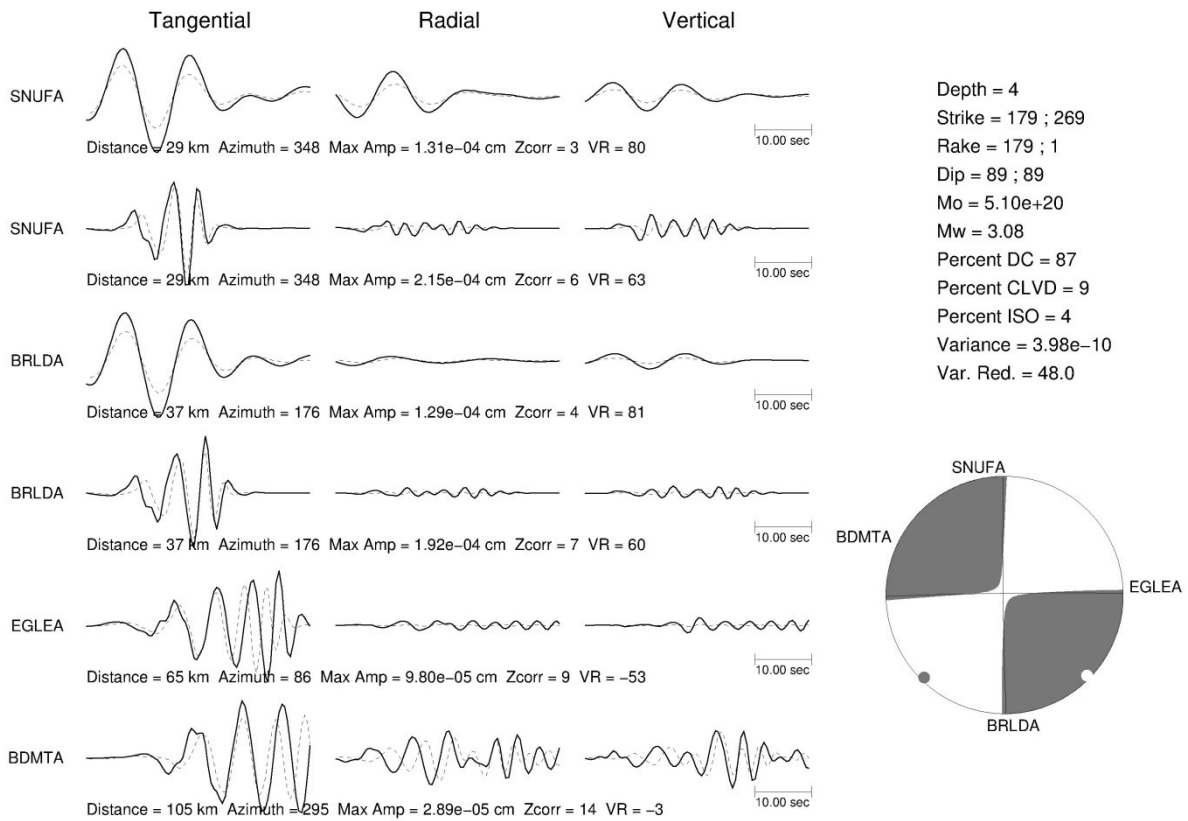


Figure A.8: Waveform fitting using synthetic data and model with increased velocity by 20%. The Zcorr are relative shifts and are all positive in this case.

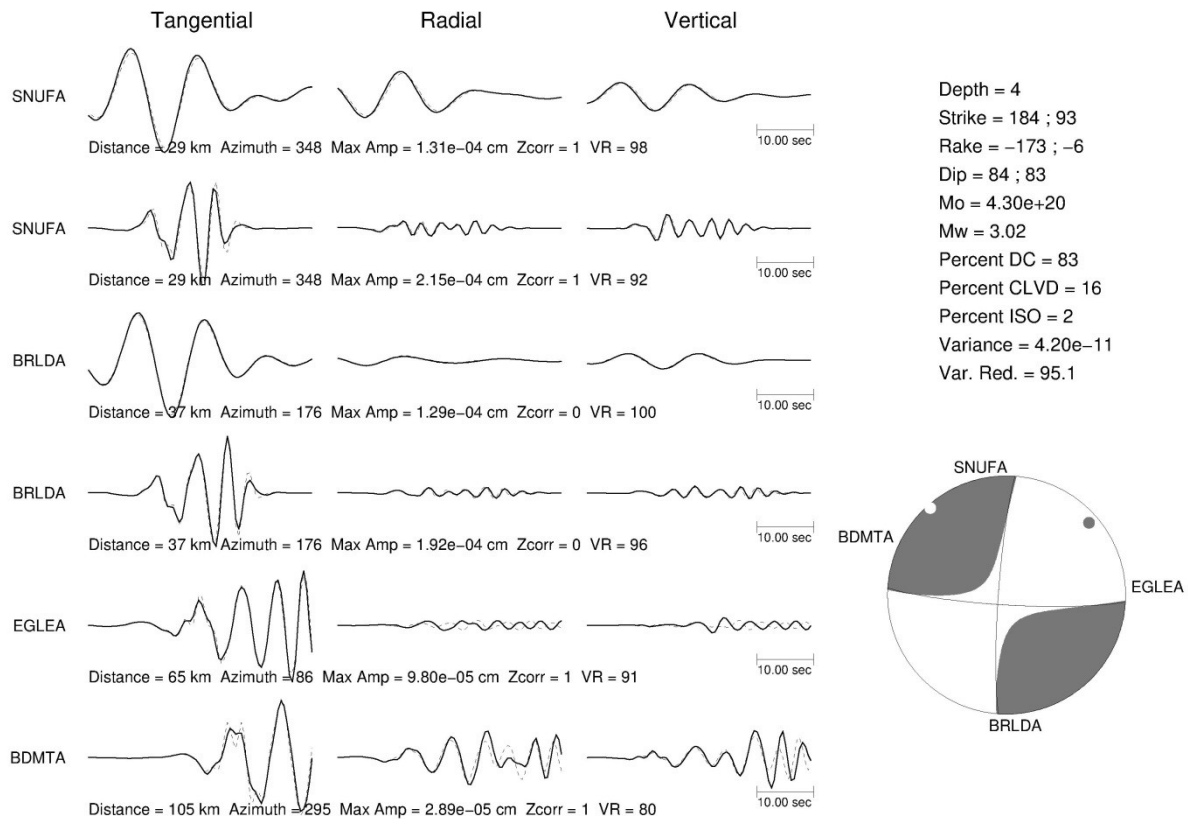


Figure A.9: Waveform fitting using synthetic data and model with randomly permuted (<10%) velocity (relative to the preferred model, also see Figure A2).

A1.3 SNR test

Similar to section A1.2, I added two types of noise into my synthetic data and repeated the inversion for various levels of noise (Table A3). The corresponding waveforms are presented in Figures A10-21. The random noise is generated with FUNGEN in SAC (Seismic Analysis Code). To ensure comparable spectrum, I also repeat my SNR test by adding real noise randomly cut from the one-day data (June 1, 2017) of the four stations (Figure A1). The VR lowers with increasing noise level, and most of the tests successfully recover the input focal mechanisms. My tests indicate that the inversion outcomes may be less stable when the noise level is above 25% (random) or five times (real). However, after removing the noisy stations with relatively low SNR,

I can still retrieve a reasonable full moment tensor with an input noise level as high as eight times the observed values at the seismic stations (Figure A22).

Noise level	Noise type	VR	Decomp (DC/CLVD/ISO)
10% of T* amplitude	Random (Gaussian)	95.8	73/27/0
15% of T amplitude	Random (Gaussian)	90.8	69/30/0
20% of T amplitude	Random (Gaussian)	86.4	66/34/1
25% of T amplitude	Random (Gaussian)	77.6	62/37/1
30% of T amplitude	Random (Gaussian)	70.3	59/40/1
1×	Real	96.8	76/22/2
2×	Real	95.0	80/19/1
3×	Real	83.8	79/20/1
4×	Real	76.3	81/18/1
5×	Real	62.6	53/33/14
6×	Real	58.7	70/28/1
7×	Real	50.4	55/37/8
8×	Real	22.2	34/41/25
8× (but only two stations)		68.8	78/15/7

Table A.3: Summary of SNR tests.

*: T for transform component, which contains the largest amplitude for a strike-slip event received by my designed station coverage.

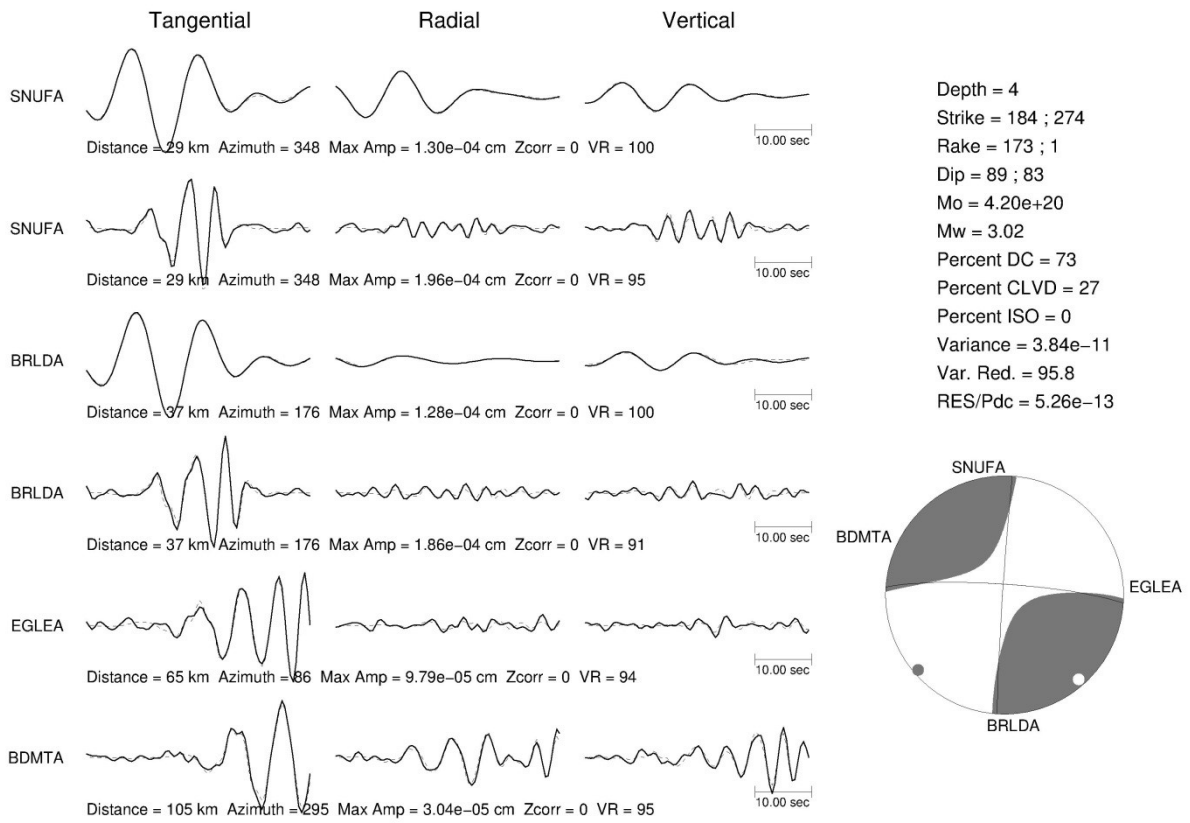


Figure A.10: Synthetic waveforms (solid lines) fitted with 10% random noise added (dashed lines).

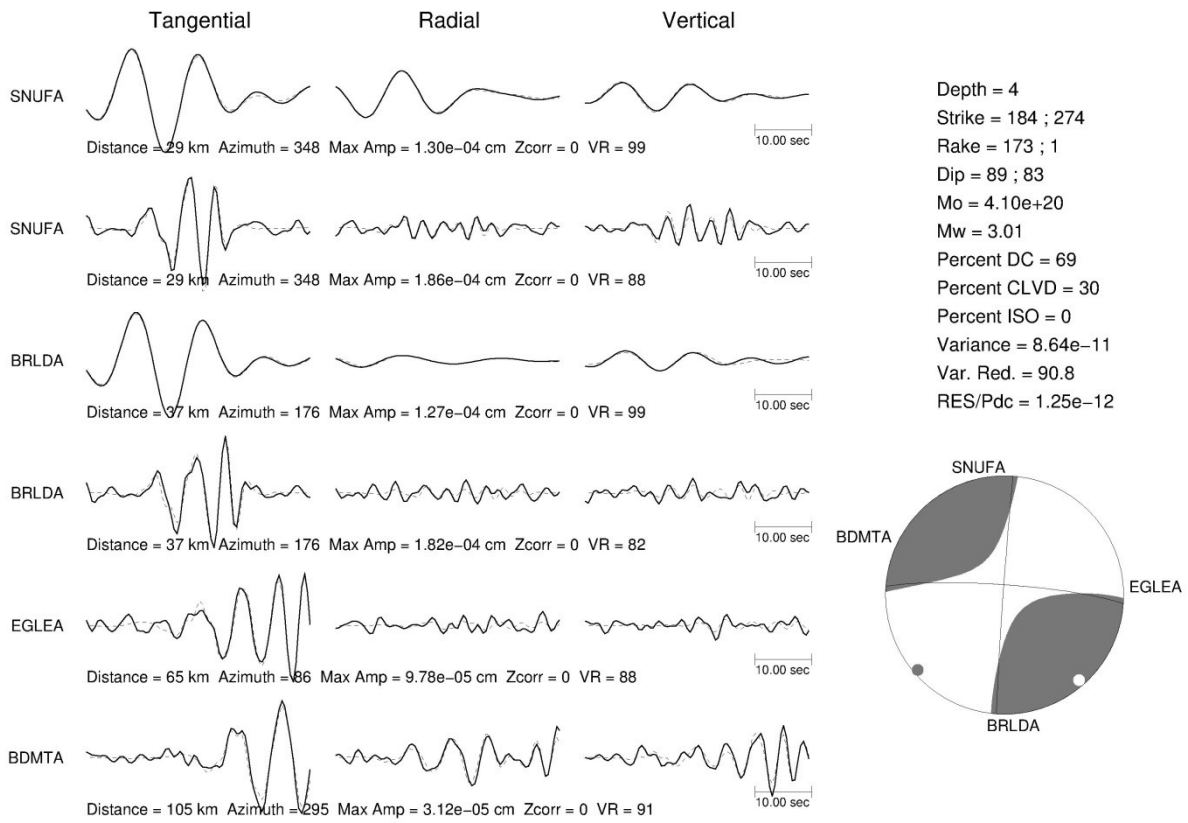


Figure A.11: Synthetic waveforms (solid lines) fitted with 15% random noise added (dashed lines).

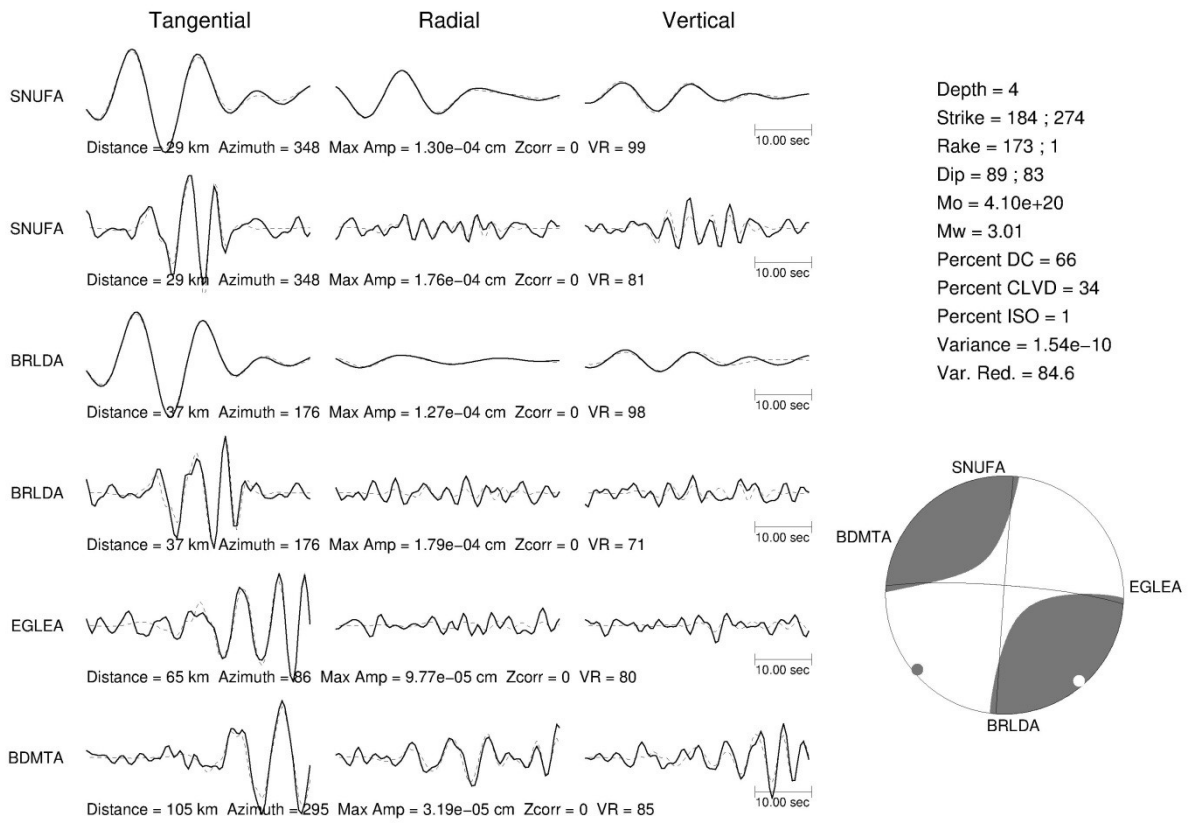


Figure A.12: Synthetic waveforms (solid lines) fitted with 20% random noise added (dashed lines).

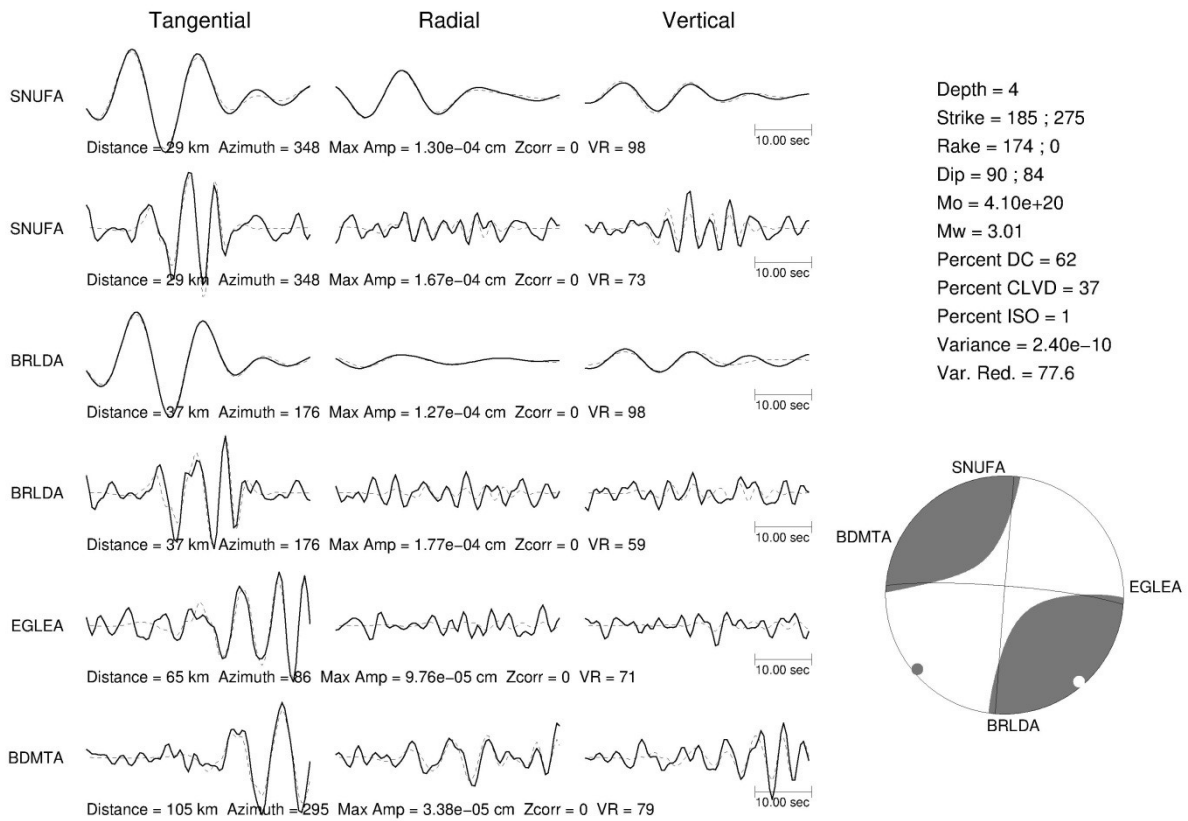


Figure A.13: Synthetic waveforms (solid lines) fitted with 25% random noise added (dashed lines).

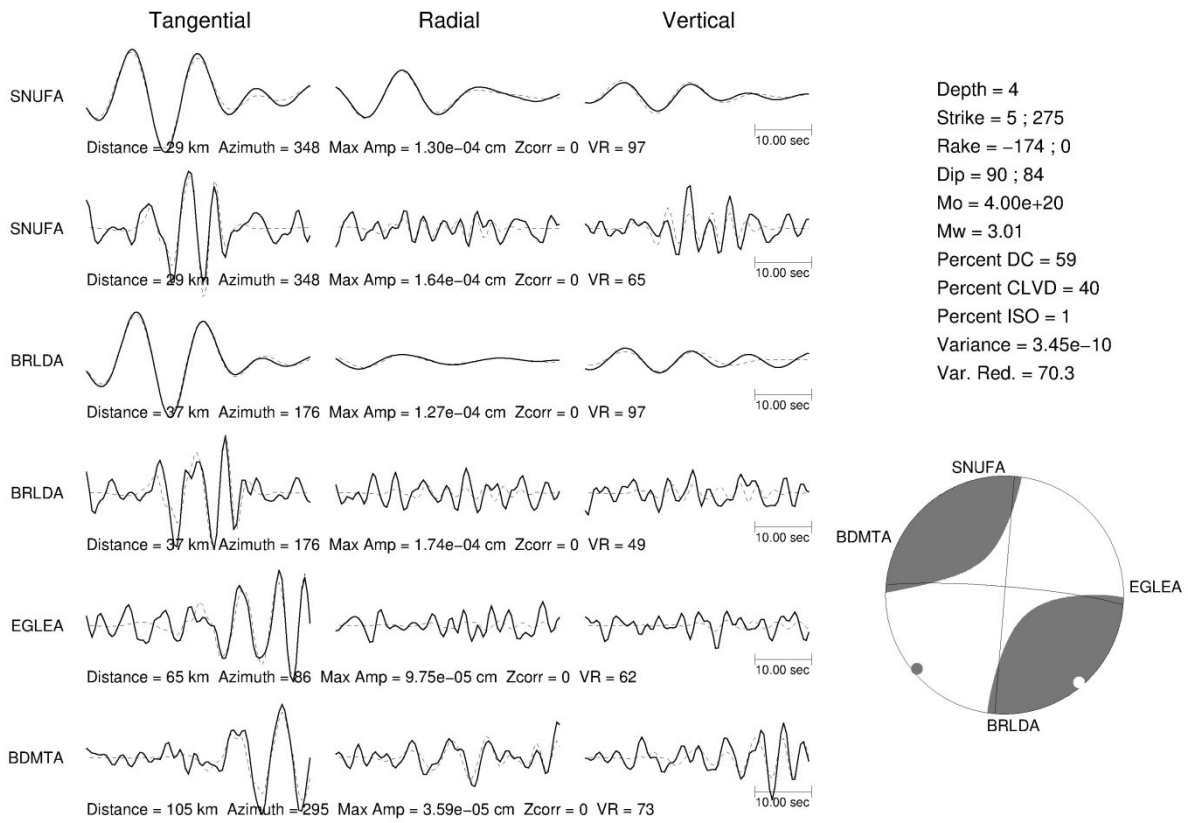


Figure A.14: Synthetic waveforms (solid lines) fitted with 30% random noise added (dashed lines).

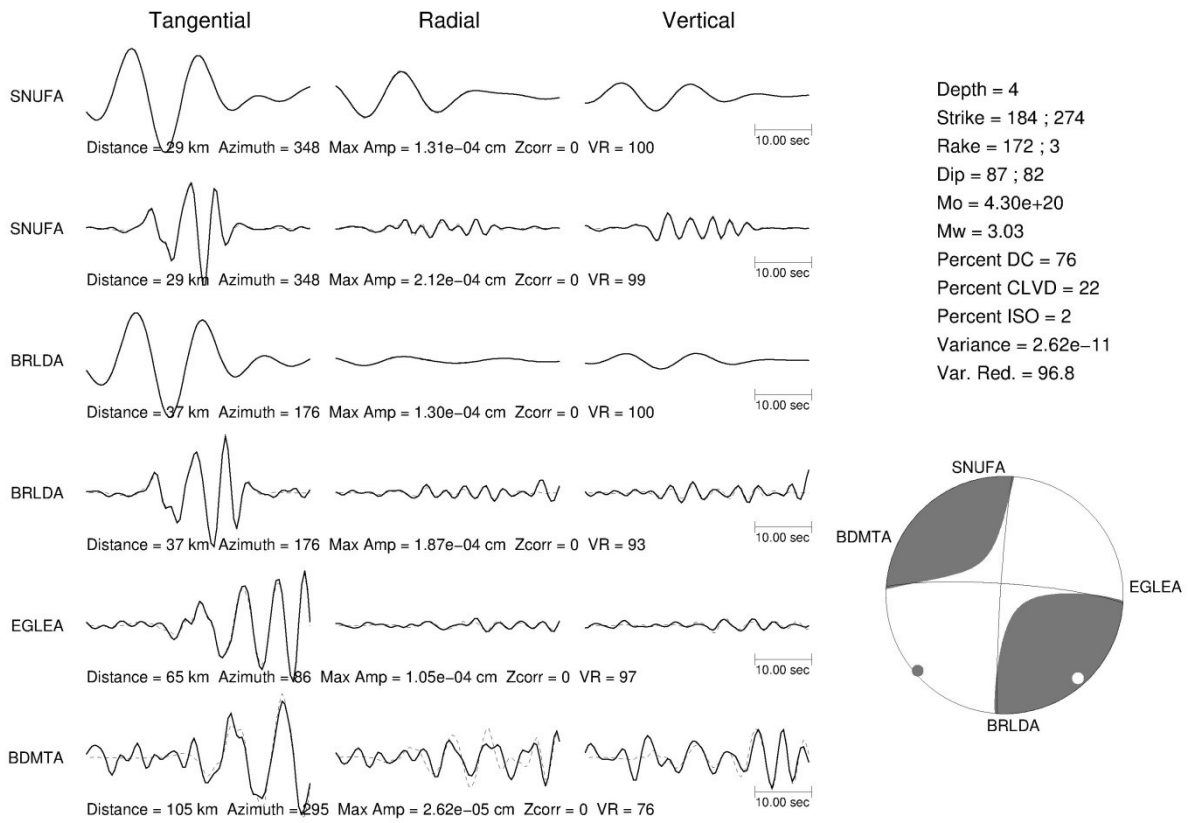


Figure A.15: Synthetic waveforms (solid lines) fitted noise equal to the observed value at each station (dashed lines).

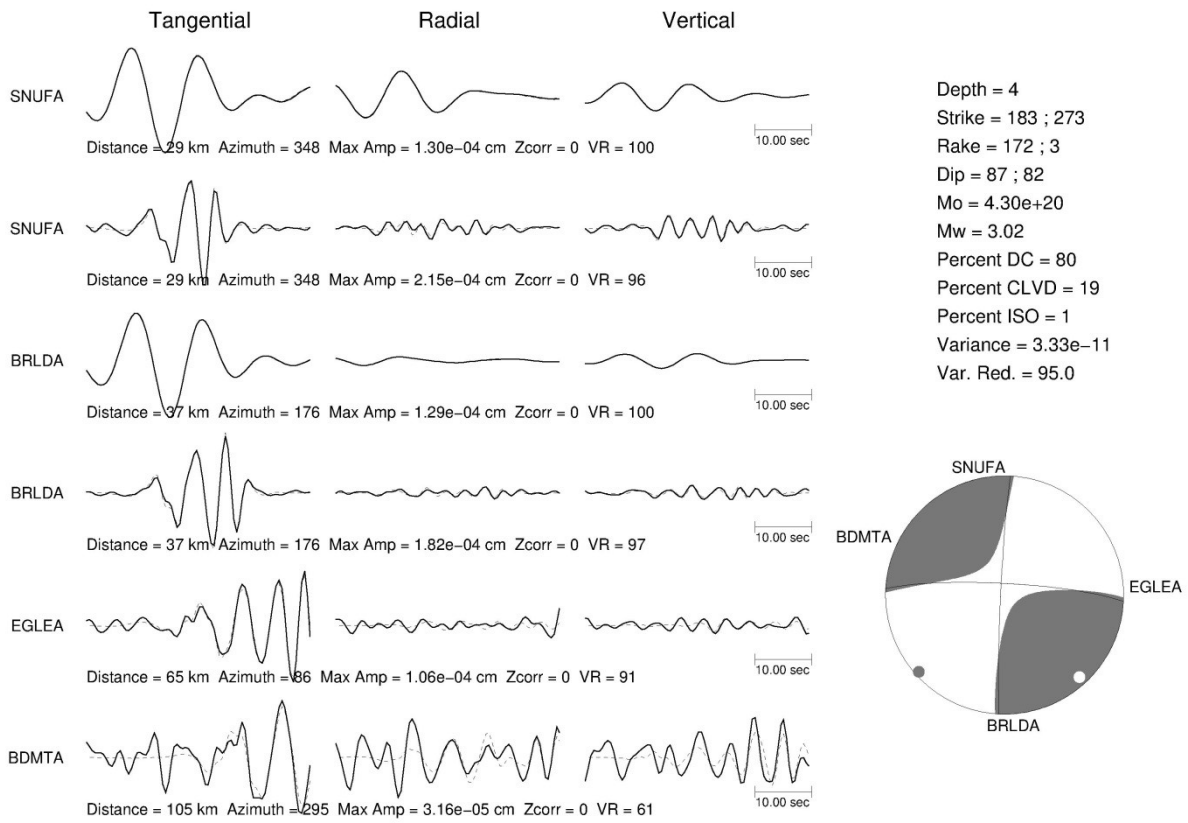


Figure A.16: Synthetic waveforms (solid lines) fitted with 2 times of real noise added (dashed lines).

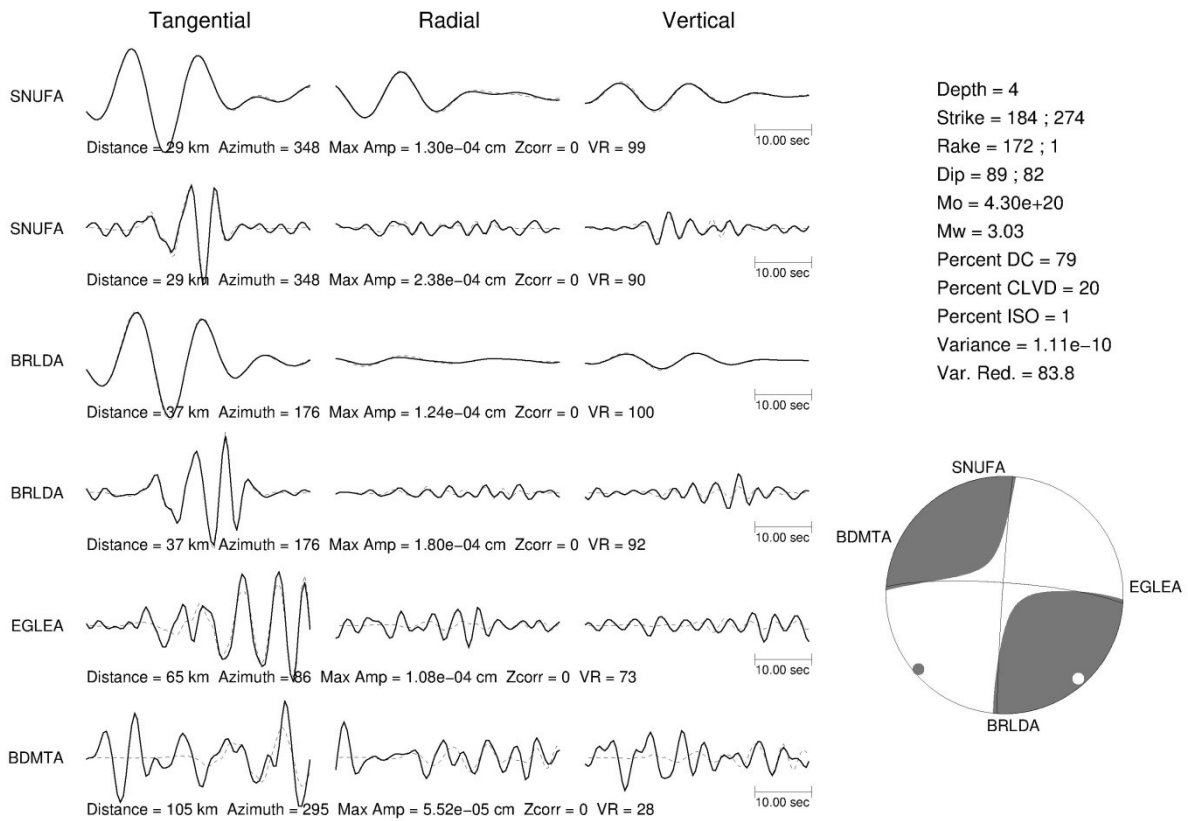


Figure A.17: Synthetic waveforms (solid lines) fitted with 3 times of real noise added (dashed lines).

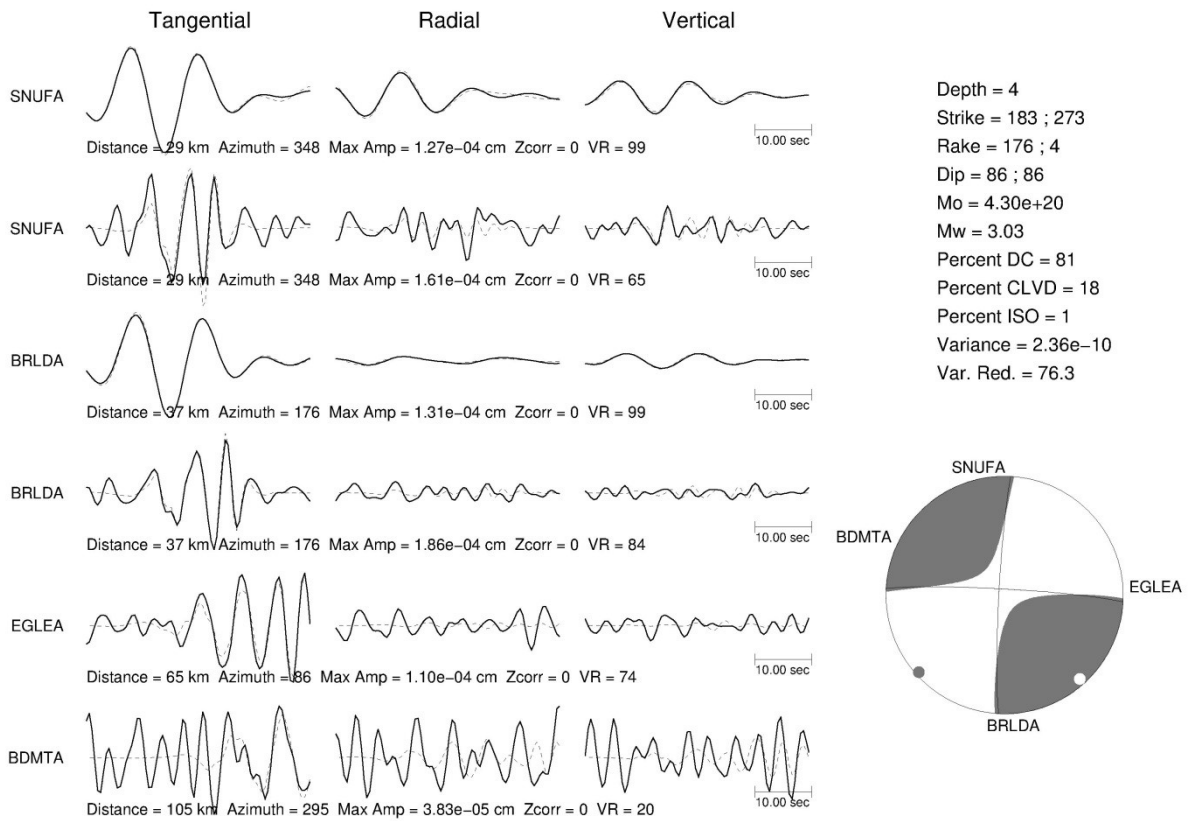


Figure A.18: Synthetic waveforms (solid lines) fitted with 4 times of real noise added (dashed lines).

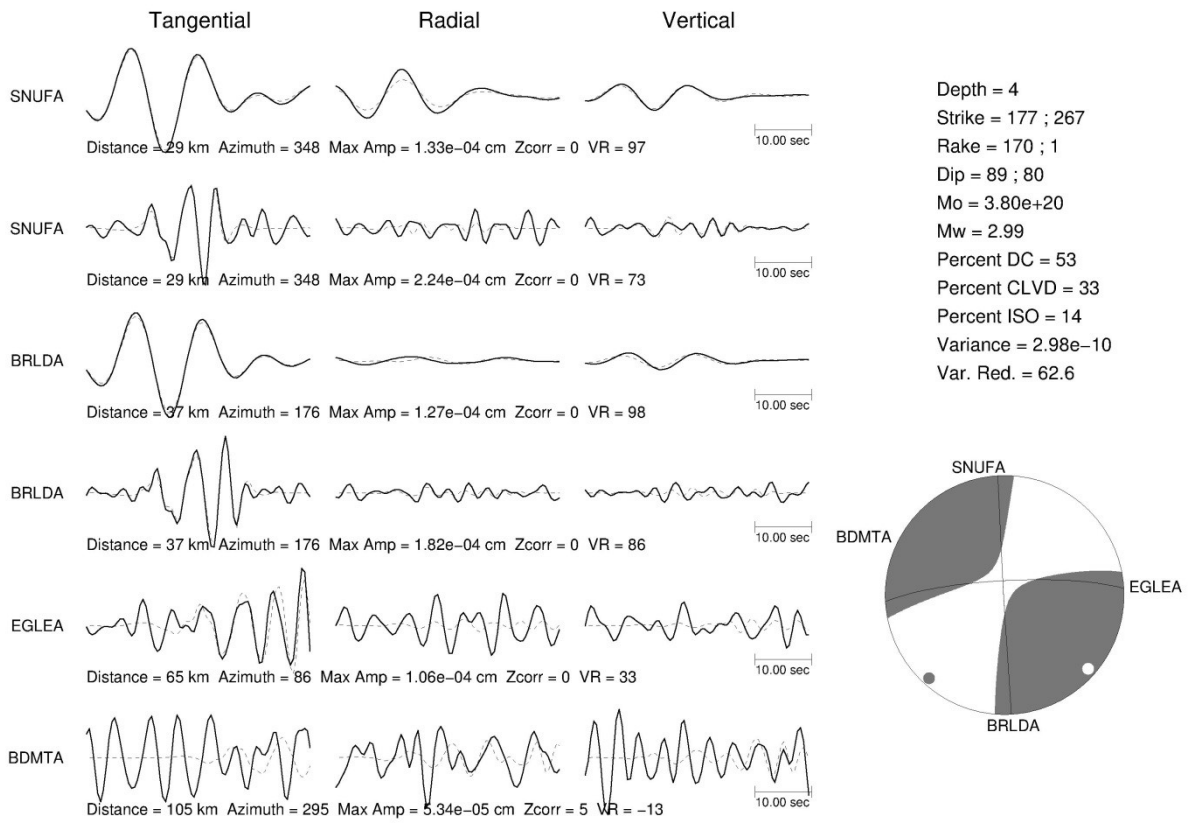


Figure A.19: Synthetic waveforms (solid lines) fitted with 5 times of real noise added (dashed lines).

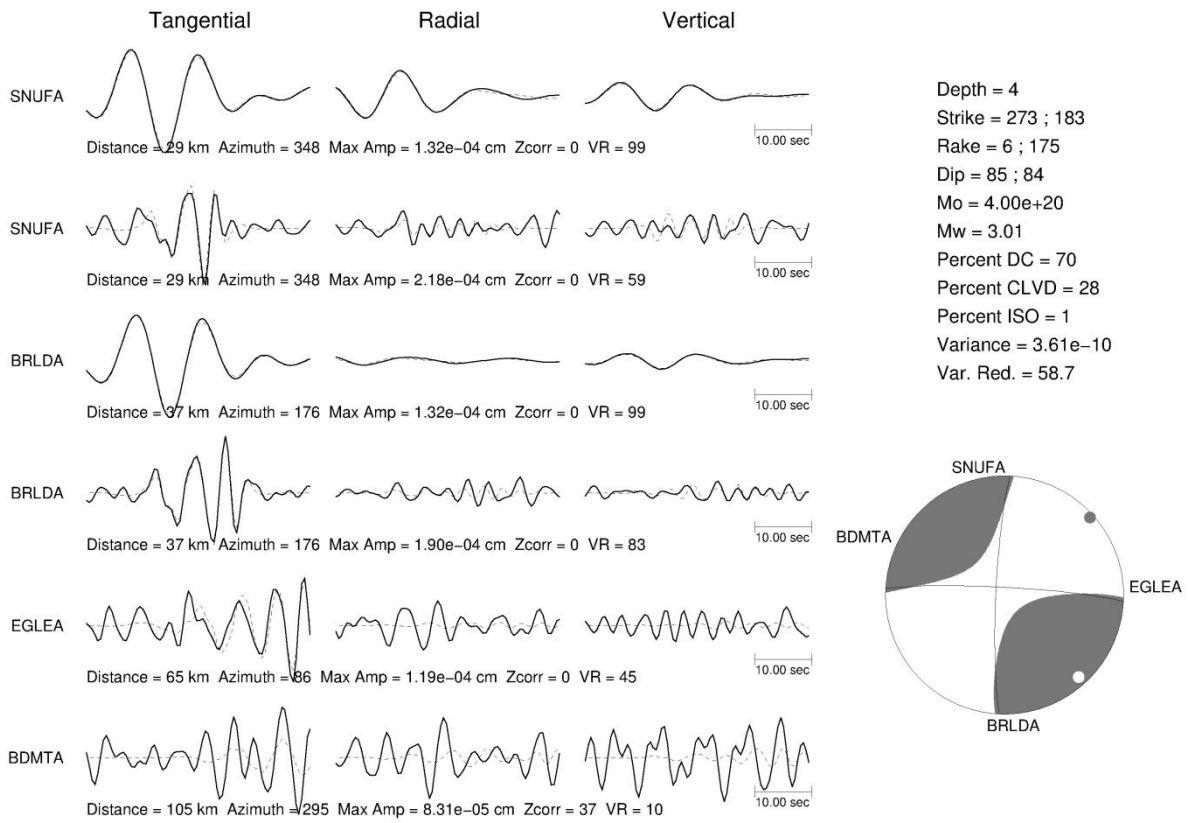


Figure A.20: Synthetic waveforms (solid lines) fitted with 6 times of real noise added (dashed lines).

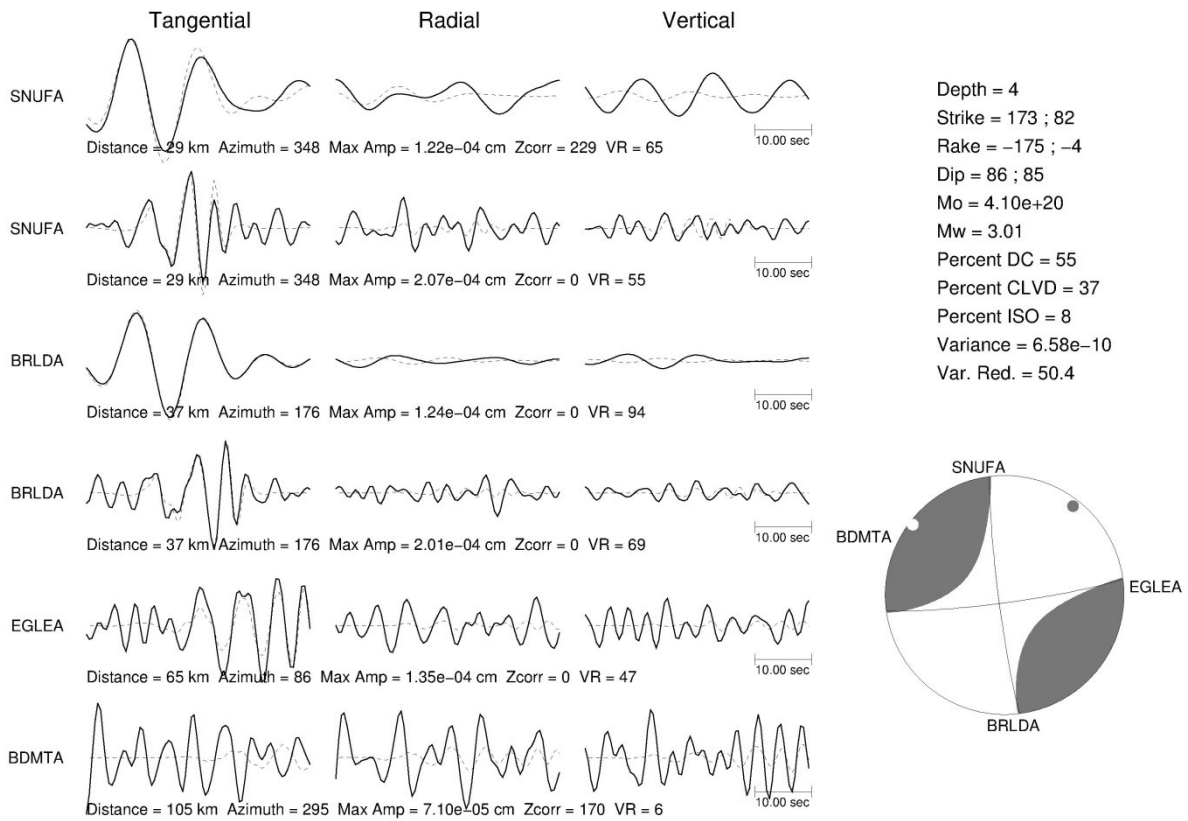


Figure A.21: Synthetic waveforms (solid lines) fitted with 6 times of real noise added (dashed lines).

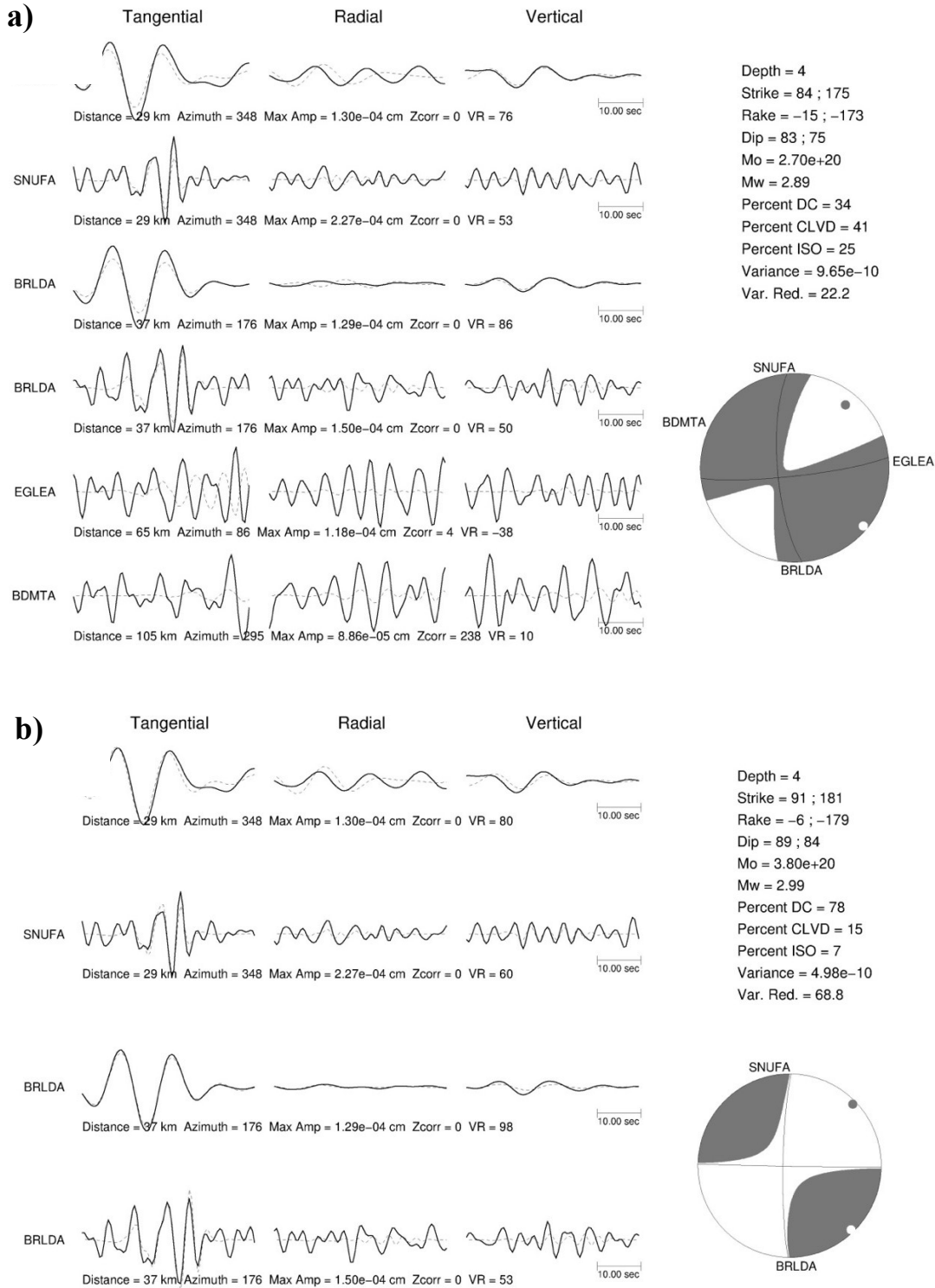


Figure A.22: Synthetic waveforms (solid lines) fitted with 8 times of real noise added (dashed lines): (a) use all four stations and (b) use only two stations with high SNR.

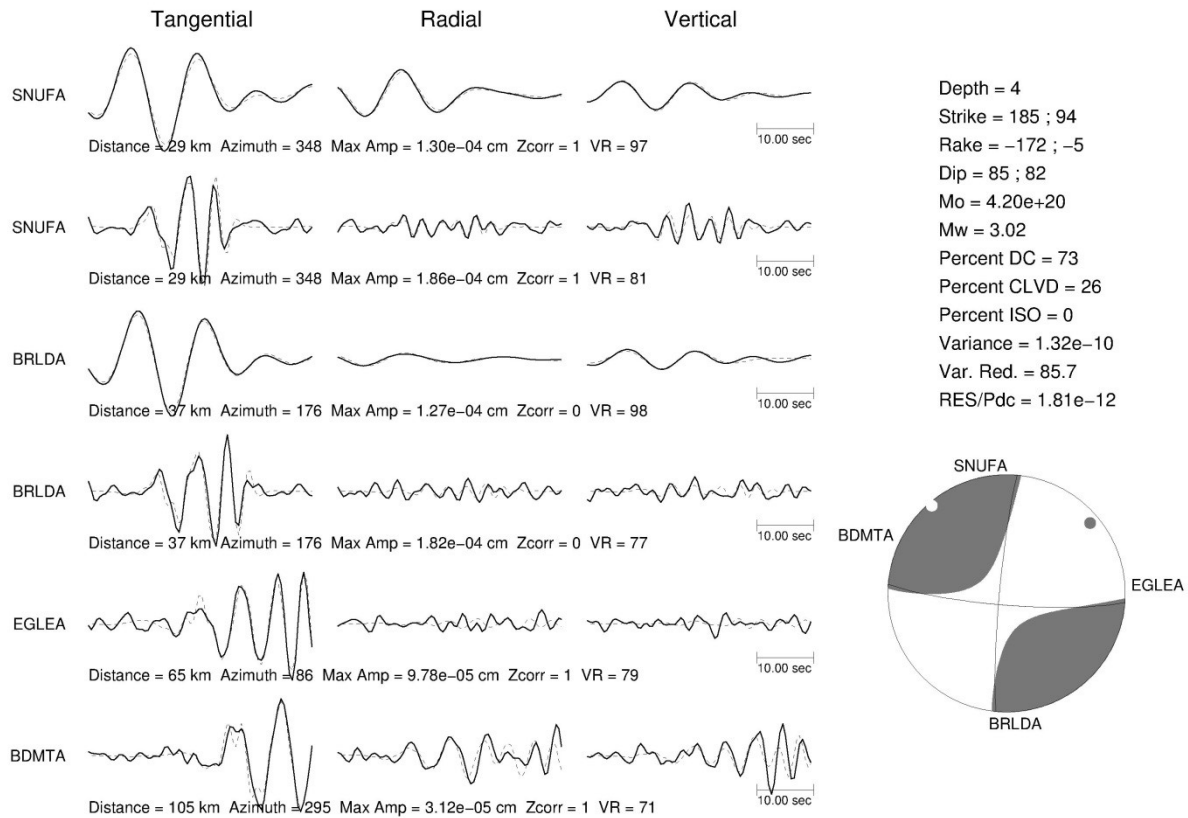


Figure A.23: Synthetic waveforms (with 15% noise) fitted with the randomly perturbed model (relative to the preferred model, see Figure A2). The result resembles my input focal mechanism.

A1.4 Real data fitting and conclusions

From the above synthetic tests, I show that the waveforms can be matched well and the recovered non-DC components are highly stable (Figure A23). My source locations are strongly correlated with those of industrial activities (chapters 3 and 4). My preferred velocity model is adopted by colleagues and researchers in their related studies of the WCSB (Chen *et al.* 2015; Wang *et al.* 2016; Schultz *et al.* 2017; Clerc *et al.* 2016; Farrugia *et al.* 2017).

I show that my choice of hypocenter location, velocity model, and station distribution are sufficient to provide trustworthy full moment tensor inversions. When the noise level is high (e.g., comparable to or even higher the amplitude of signal; station EGELA in Figure A22, a), removing low SNR stations and inversion with only two stations (see Figure A22, b) can provide the identical result to the true solution (Table A2). The surprisingly stable results benefit from:

- 1) the adoption of multi-phases and multi-frequency ranges
- 2) the availability of near-source three-component stations
- 3) detailed 14-layer crustal model (see chapter 2)

A2. Related software

name	use	reference
GMT	Figure making	Wessel <i>et al.</i> 2013
SAC	Seismograph processing	Goldstein & Snoke 2005
Taup	Phase arrival & ray path calculation	Crotwell <i>et al.</i> 1999
M&L	Events detection & location	Zhang & Wen, 2015
hypoDD	Events location	Waldhauser & Ellsworth 2000
TDMT_INV	Time domain moment tensor inversion	Dreger 2003
FKPRROG	Green's function generation	Saikia <i>et al.</i> 1994

Table A.4 List of used software for this thesis